Search for light long-lived neutral particles that decay to collimated pairs of leptons or light hadrons in pp collisions at $\sqrt{s} = 13\ TeV$ with the ATLAS detector

UNIVERSITY OF LIVERPOOL

Thesis submitted in accordance with the requirements of the University of Liverpool for the degree of Doctor in Philosophy by

Alessandro Biondini

Department of Physics
Oliver Lodge Laboratory
University of Liverpool

June 2023

Abstract

The Standard Model (SM) of particle physics provides an incredibly accurate description of a wide range of physics phenomena. However the scientific community is well aware that the SM is not the ultimate, complete theory we are hoping for. A key role in the quest for new physics is covered by searches for new phenomena, such as the one described in this thesis. This search has been performed using events selected in 139 fb^{-1} of $\sqrt{s} = 13$ TeV of proton-proton collision data provided by the Large Hadron Collider (LHC) and collected by the ATLAS experiment. The search aims to identify new physics particles, referred to as dark-photons, that are neutral, have a long lifetime and travel macroscopic distances inside the detector. In particular, the analysis targets the production of dark-photons arising in the decay of a Higgs boson, produced via gluon-gluon fusion or in association with a W boson, and exploits simplified models where the existence of a hidden sector, weakly coupled to the SM, is assumed. The search aims to identify light neutral particles that decay outside the innermost region of the detector, involving the production of collimated bundles of SM fermions in the final state. This experimental signature, referred to as Dark Photon Jets (DPJs), requires the use of dedicated triggers, custom object reconstruction algorithms, and sophisticated background rejection techniques involving deep-learning-based classifiers. The observed event yields are consistent with the expected background and are used to set constraints on benchmark models predicting the existence of long-lived particles. A Higgs boson branching fraction above 1% is excluded at 95% confidence level for a Higgs boson decaying into two dark-photons, for dark-photon mean proper decay lengths between 10 mm and 250 mm, and dark-photons with masses between 0.4 GeV and 2 GeV.

Finally, this thesis describes also a study that has been carried out in the context of the upgrade of the tracking system of the ATLAS experiment. This study involves the validation of a new framework for the reconstruction of testbeam data.

Declaration

I hereby confirm this work is my own, except where other works are referenced. In particular, the author has been the main contributor to the analysis work described in chapters 5 and 6 on what is referred to as the WH part of the analysis, with however non-negligible contribution to the ggF side of the analysis. The author has also been one of the main contributors of the work described in Appendix A. This work has not previously been submitted to any institute, including this one. This thesis does not exceed the relevant word count.

Alessandro Biondini

Contents

List of Figures

List of Tables

Introduction

Humanity has been, in all of its history, in a constant journey towards the exploration and understanding of the Universe. For what concerns the knowledge of elementary particles and their interaction, huge progresses have been made during the last century. The union of quantum mechanics and special relativity led to the introduction of quantum field theory, which provides the mathematical structure for the Standard Model (SM). The SM is the theoretical model that summarises all known elementary particles and their interactions, with the exception of gravitation. Elementary and composite particles were discovered by the handful, sometimes following from theoretical prediction and sometimes being observed before the theory was in place. The weak and strong forces were proposed along with the Higgs field. The most recent important confirmation of the validity of the SM has been the discovery of the Higgs boson in 2012, by the ATLAS and CMS experiments at the Large Hadron Collider.

However, it is well known that the SM cannot be the complete theory that we are looking for. In fact, new physics Beyond the SM (BSM) is well motivated by the presence of several observed experimental phenomena, which the SM is unable to describe, and is also needed to solve problems related to the SM theory itself. Countless new theories have been proposed, and a huge effort has been made by experimentalists over the last few decades. Unfortunately, no compelling evidence has been found yet to support any particular proposed theory.

The work described in this thesis adds to the efforts in the search for new physics in the context of high energy collider experiments, and it is focused on the exploration of the uncovered regions in the lifetime frontier at LHC. The overwhelming majority of searches for new physics BSM at the LHC focus on promptly-decaying particles, even though the SM consists of particles with a variety of masses and lifetimes. Many theories for new physics often predicts the same behaviour, having the long lifetime of a particle being originated from a small coupling constant or limited available phase space. Particles with a non-negligible lifetime are referred to as Long-Lived Particles (LLPs). Due to the limited amount of searches for LLPs at the LHC that have been carried out, there is still a wide region of the phase space left uncovered, and accessible at LHC energies. However, the reason for the presence of those gaps in the coverage of LLPs searches is that those particles often travel long distances in the detector and produce a wide variety of unconventional

signatures in the detector.

Among the many BSM theories available, one option is to search for LLPs using simplified benchmark models. In those models, a bottom-up approach is used meaning that rather than a complete new physics model only a minimal, or quasi-minimal, extension of the SM is introduced. Therefore, simplified benchmark models can be derived as limits of more complete theoretical frameworks. They often predicts the existence of a dark sector, weakly coupled to the SM, where unstable dark states may be produced, resulting in the presence of LLPs.

In this thesis, the option that is explored involves that the SM and dark sectors communicate through the so-called *Higgs portal* for the production of the beyond the SM particles and through a *vector portal* for the decay of the produced particles. In particular, a dark-photon is assumed to be produced via Higgs decay, or via the decay of a heavy scalar Higgs-like boson, and to mix kinetically with the SM photon, subsequently decaying into leptons and light quarks [1]. The kinetic mixing parameter ε determines the lifetime of the dark-photon, and it is theoretically allowed to vary over a wide range of values. The analysis described in this thesis focuses on small values of the kinetic mixing parameter, corresponding to dark-photon decays happening at a macroscopic distance from their production point, and with dark-photon mass in the O(MeV-GeV) range. Due to their small mass compared to the energy scale of the hard-scattering process, the dark-photons are expected to be produced with large Lorentz boosts, resulting in collimated bundles of fermions grouped in a jet-like structure, referred to as Dark-Photon Jets (DPJs).

The search presented here [2] makes use of the dataset collected at the Large Hadron Collider by the ATLAS detector between 2015 and 2018 in proton-proton (pp) collisions at a centre-of-mass energy of $\sqrt{s} = 13$ TeV, corresponding to an integrated luminosity of 139 fb^{-1}. Previous searches for displaced DPJs were performed by ATLAS [3], as well as searches for prompt DPJs [4], which cover complementary regions of the kinetic mixing-dark-photon mass parameters space.

As a result of the work presented in this thesis, the sensitivity to displaced DPJs is significantly improved, not only due to the higher integrated luminosity of the dataset, but also thanks to the newly developed analysis methods. These include an updated signal region selection and the use of dedicated deep-learning-based taggers, that play a crucial role in the background rejection. In addition, the analysis sensitivity also benefits from the exploitation of a new set of event selection criteria, targeting events where the dark-photons arise from the decay of a Higgs boson, or a heavy scalar Higgs-like boson, produced in association with a W boson.

The thesis is organised as follows. Chapter 1 gives an overview of the Standard Model, its current limitations, and also describes the possible SM extensions involving LLPs and the models used as benchmarks. Chapter 2 summarises the main characteristics of the LHC and of the ATLAS detector. Chapter 3 describes the datasets used in the analysis

detailed in this thesis, along with the triggers used and the description of the Monte-Carlo simulated samples. Chapter 4 is devoted to the description of the object reconstruction and identification in ATLAS. In Chapter 5, the methods and tools used to perform the displaced dark-photon jet analysis are described, while in Chapter 6 the analysis results and their interpretation are discussed. Finally, in Appendix A, an overview is given about the technical work that has been carried out in the context of testbeam data reconstruction for the ATLAS Inner Tracker upgrade.

Part I

Theoretical overview and experimental apparatus

Chapter 1

The Standard Model and Beyond

This chapter presents an overview of the Standard Model (SM) of elementary particles, which currently represents our best tool to describe nature from the microscopic point of view. Nonetheless, the SM provides a unified description of only three out of the four known fundamental forces: the electromagnetic, strong and weak interactions, therefore excluding the gravitational interaction. This represents only one of the shortcomings of the SM, some of which are briefly discussed later in this chapter. An overview of the possible extensions of the SM involving dark sectors are also presented. Feebly interacting and therefore Long-Lived Particles (LLPs) arising from the dark sectors are discussed, as they represent the main objective of this thesis.

1.1 The Standard Model

The SM of particle physics is the theoretical framework that describes the fundamental constituents of matter and their interactions under three of the four known fundamental forces: electromagnetic, weak and strong. These interactions are described using the mathematical framework of Quantum Field Theory [5] (QFT), which is currently not able to describe the gravitational interaction[1]. However, the effects of gravity at the collider energy scale can be considered negligible. The SM was first introduced in the late 1960s and fifty years of precision measurements at collider experiments have proven its remarkable capability not only in describing experimental observations, but also in providing predictions for a wide array of physics phenomena with a high level of accuracy. Nevertheless, there are several experimental indications left unexplained by the theory, indicating hints of new physics Beyond the SM (BSM).

[1]Including gravity in the Standard Model theoretical framework has proven to be very challenging and it is currently an area of active research.

1.1.1 Overview

The Standard Model is a renormalisable QFT[2] that unifies quantum mechanics and special relativity. In this formulation, the wave function of a single particle is described by a local field (ψ) depending on the four-dimensional space-time coordinates (x). The Lagrangian formalism introduced in classical mechanics can be extended to quantum field theory. Therefore, the dynamic of a quantum field system can be written in terms of a Lagrangian density[3] $\mathcal{L}$, function of the field ψ and its derivatives $\partial_\mu\psi$, that needs to satisfy the principle of least action:

$$\delta\mathcal{S} = \delta \int d^4x \mathcal{L}(\psi, \partial_\mu\psi) = 0. \tag{1.1.1}$$

This corresponds to the requirement of the action $\mathcal{S}$ to be stationary.

The expression of this Lagrangian in the SM must take into account the symmetries observed in nature. Noether's theorem [7] ensures that any continuous symmetry of the Lagrangian yields a conserved current and charge. Therefore, the corresponding Lagrangian must be invariant under Lorentz transformations, and is also required to be invariant under a continuous group of local transformations called gauge symmetries: $SU(3)_C \otimes SU(2)_L \otimes U(1)_Y$. Each of these gauge symmetries have a relation with fundamental forces whose interaction is described by the SM:

- $SU(3)_C$ is related to the strong nuclear force sector in which the relative conserved charge is the colour (C), and that is described by the theory of Quantum Chromo-Dynamics (QCD);
- $SU(2)_L \otimes U(1)_Y$ represents the symmetry group of the unified electromagnetic and weak interactions, referred to as electroweak sector, with the weak isospin (L stands for left-handed) and the hypercharge (Y) as conserved charges.

In QFT, the constituents of matter are represented by particles obeying to the Fermi-Dirac statistics, called *fermions*, which are represented by spinors ψ with half-integer spin, whose free dynamic is described by the Dirac Lagrangian:

$$\mathcal{L} = \bar{\psi}(i\gamma^\mu\partial_\mu - m)\psi, \tag{1.1.2}$$

with γ^μ being the Dirac matrices and m the mass of the fermion. Fermions interact with each other through the exchange of force-carriers, represented by integer spin particles which follow the Bose-Einstein statistics, called *bosons*. These naturally arise in the theory from the requirement of local gauge invariance. Finally, in the SM only one spin zero

[2] A renormalisable QFT is a theory in which every divergence in the calculation can be regularised and cancelled, yielding finite expressions for measurable quantities [6].

[3] In the following, as common practice in quantum field theories, the terms Lagrangian and Lagrangian density will be treated as equivalent.

fundamental particle is present, the Higgs boson, and the mechanism related to the presence of this particle in the SM is crucial to provide a mass to other particles.

More details on the mathematical formulation of the fundamental interactions and the SM particles are given in the following sections.

1.1.2 Fundamental particles

In the Standard Model, fermions are grouped in *leptons* and *quarks*, which are divided into three so-called *generations*. Each generation contains an up- and a down-type quark, a charged lepton, and a neutral lepton called neutrino. The three generations can be distinguished by the mass of the constituent particles, which differs by many orders of magnitude. For each fermion generation, a corresponding anti-fermion exists, having the exact same properties, but opposite charges.

Leptons

Leptons are grouped in three different families, one for each lepton flavour: electron (e), muon (μ) and tau (τ). As mentioned above, each family is composed by a negatively charged lepton and a neutral lepton called neutrino. As a consequence, charged leptons interact under the electromagnetic and weak forces, whereas the neutrinos only interact under the weak force. As for all fermions, leptons are present also as anti-particles, which share the same properties but have opposite electric and weak charges. Neutrinos are massless in the SM, but experimental evidence of neutrino flavour oscillations [8] implies that neutrinos are in fact massive. The mechanism by which neutrinos have mass is not part of the original SM formulation and represents an indication that the SM is not a complete theory.

Quarks

Quarks are colour-charged particles, divided into up- and down-type depending on the carried electric charge, $Q = \frac{2}{3}e$ for up-type quarks and $Q = -\frac{1}{3}e$ for down-type quarks, where e represents the electric charge of leptons. The name up (u) and down (d) refers to the first generation quarks. The second generation contains the charm (c) and the strange (s) quarks, while the third contains the top (t) and the bottom (b) quarks. Each quark has its own flavour and, as for all fermions, for each quark type an equivalent anti-quark exists, with the same properties but opposite charges. Among all fermions, the quarks are the only elementary particles subject to all three fundamental forces. They exists in nature only as colour-free composite particles, usually composed of a quark-anti-quark pair (mesons) or of three quarks (barions).

Bosons

The electromagnetic, weak and strong forces are all mediated by spin-1 bosons. The electromagnetic interaction between electrically charged particles is mediated by the exchange of a photon, which is massless and neutral. The massive $W^{\pm}$ and Z^0 bosons are the mediators of the weak interaction. The W^+ and W^- bosons carry +1 and -1 electric charge, respectively, and interact only with left-handed fermions and right-handed anti-fermions. The Z^0 boson is neutral and interacts with all fermion and anti-fermions. The electroweak bosons gain mass through spontaneous symmetry breaking, making the weak interaction a short-range force. The strong interaction is mediated by eight massless bosons called gluons, each carrying colour charge, and therefore subject themselves to the strong force. The last piece of the SM is filled by the massive and neutral Higgs boson, whose associated field gives mass to all elementary particles of the theory except for neutrinos, which, as mentioned above, are predicted to be massless in the SM.

A scheme illustrating the SM particles and their classification is presented in Figure 1.1 where the various contours highlight which fermions are subject to each of the three fundamental forces described by the SM. The fourth fundamental force, gravity, is shown being outside the SM.

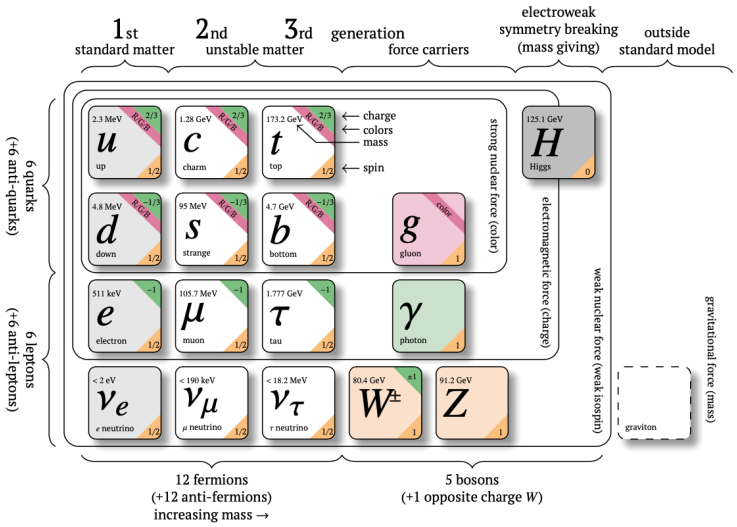

Figure 1.1: Classifications of the SM particles. Fermions are divided into quarks and leptons which are, in turn, split into three generations depending on their mass. Each generation of quarks contains an up-type and a down-type quark, and each lepton family contains a charged and a neutral lepton called neutrino. The three fundamental forces are carried by spin-1 bosons, while the interaction of the elementary particles with the Higgs boson gives them a mass. The contours in the figure show which fermions are subject to which force. Figure from [9].

1.1.3 Quantum Electro-Dynamics

Quantum Electro-Dynamics [10] (QED) is the theory describing the interaction between charged fermions and the electromagnetic field in terms of relativistic QFT. The corresponding Lagrangian can be initially written as the sum of the Dirac Lagrangian, describing the free propagation of a fermion, and the covariant representation of the electromagnetic field described by Maxwell equations:

$$\mathcal{L} = \bar{\psi}(i\gamma^\mu \partial_\mu - m)\psi + \frac{1}{4}F^{\mu\nu}F_{\mu\nu}, \tag{1.1.3}$$

where $F_{\mu\nu} = \partial_\mu A_\nu - \partial_\nu A_\mu$ is the electromagnetic tensor, with $A_{\mu,\nu}$ representing the electromagnetic field. This Lagrangian is invariant under global transformations of the U(1) symmetry group, but in order to be invariant under local gauge transformations described by the continuous function $\alpha(x)$:

$$\psi \to e^{i\alpha(x)}\psi, \tag{1.1.4}$$

the partial derivative $\partial_\mu \psi$ must be replaced by its covariant formulation:

$$D_\mu \psi = (\partial_\mu + ieA_\mu)\psi. \tag{1.1.5}$$

In this way the Lagrangian from 1.1.3 can be re-written as:

$$\mathcal{L} = \bar{\psi}(i\gamma^\mu D_\mu - m)\psi - \frac{1}{4}F^{\mu\nu}F_{\mu\nu} = \bar{\psi}(i\not{\partial} - m)\psi - \frac{1}{4}F^{\mu\nu}F_{\mu\nu} - e\bar{\psi}\not{A}\psi = \mathcal{L}_{QED}, \tag{1.1.6}$$

with $\not{\partial} = \gamma^\mu \partial_\mu$ and $\not{A} = \gamma^\mu A_\mu$. In this Lagrangian, the term $-e\bar{\psi}\not{A}\psi$ represents the interaction between fermions and the massless A_μ field, which represents the photon. Moreover, the electric charge conservation follows from the Noether theorem for this Lagrangian and symmetry group.

1.1.4 Quantum Chromo-Dynamics

Quantum Chromo-Dynamics (QCD) is the theory describing the strong interaction. It is based on the non-abelian[4] $SU(3)_C$ symmetry group, with colour (red, blue and green) as corresponding conserved charge. The strong force is mediated by eight massless and colour-charged bosons, the gluons, which as a result of this also interact with themselves.

The QCD Lagrangian can be derived with the same procedure used for the QED case. In this case, the Lagrangian needs to be invariant under gauge transformations of the $SU(3)_C$

[4] A non-abelian gauge symmetry group is a set of gauge transformations which do not obey the commutative law.

group, represented as:

$$q_i(x) \rightarrow e^{i\vec{a}(x)\cdot\vec{T}} q_i(x), \tag{1.1.7}$$

where $q_i(x)$ is the three-component Dirac spinor representing a quark with colour i, $\vec{\alpha}(x)$ is a vector of eight parameters as a function of the Lorentz coordinates x, and $\vec{T}$ are the eight 3×3 Gell-Mann matrices[5]. The covariant derivative for SU(3) can be defined as:

$$D_\mu = \partial_\mu + i\alpha_s A_{\mu a} T^a, \tag{1.1.8}$$

with α_s being the QCD coupling constant and A^a_μ representing the gluon fields. Therefore, the QCD tensor field $G^a_{\mu\nu}$ assumes the following form:

$$G^a_{\mu\nu} = \partial_\mu A^a_\nu - \partial_\nu A^a_\mu + \alpha_s f^{abc} A^b_\mu A^c_\nu, \tag{1.1.9}$$

where f^{abc} represents the so-called structure constants of the group, obtained from the non-commutative QCD generators, $[T_a, T_b] = i f_{abc} T^c$. In the tensor definition, the non-abelian term $\alpha_s f^{abc} A^b_\mu A^c_\nu$ illustrates the self-interactions of gluons. At this point, the QCD Lagrangian can be written as follows:

$$\mathcal{L}_{QCD} = \sum_{flavours} \bar{q}_i (i\gamma_\mu D^\mu - m)_{ij} q_j - \frac{1}{4} G^a_{\mu\nu} G^{\mu\nu}_a, \tag{1.1.10}$$

with i and j being the colour indices of the quarks running from 1 to 8, and a the colour index of the gluons running from 1 to 8. A distinctive feature of QCD is the so-called colour confinement, which manifests as a consequence of the fact that the running coupling α_s becomes larger at higher distances. This means that free quarks cannot be observed as it is impossible to separate them from a combined state. On the contrary, at small distances the coupling gets weak and quarks can be assumed to behave as free particles. The colourless states in which quarks are confined are called hadrons. In addition, extracting a quark from its bound state is energetically disfavoured such that new quark-antiquark pairs come from the vacuum to form new hadrons with the original quarks. This process is referred to as hadronisation. Hadrons are called mesons if they contain a quark and an anti-quark, or baryons if they contain three quarks.

1.1.5 Electroweak sector

The electroweak theory has been proposed in the late 1960's by Glashow [11], Weinberg [12] and Salam [13], and describes the unification of the electromagnetic and weak interactions under the $SU(2)_L \otimes U(1)_Y$ gauge symmetry group.

[5]The Gell-Mann matrices are eight independent traceless 3×3 matrices introduced by Gell-Mann to generalise the SU(2) Pauli matrices in the context of a SU(3) theory.

The weak interactions are, in analogy with QED, mediated by vector gauge bosons, and two types of weak interactions are experimentally observed: the charged current and the neutral current interactions. The first are mediated by the massive charged bosons $W^{\pm}$, and involve only particles with left-handed chirality[6], while the second type of interactions involving neutral current are mediated by the neutral boson Z^0, which couples also ti particles with right-handed chirality. The Dirac spinors can be projected onto their left-handed and right-handed chirality components using the γ^5 Dirac matrix:

$$\psi_L = \frac{1}{2}(1-\gamma^5)\psi, \tag{1.1.11}$$

$$\psi_R = \frac{1}{2}(1+\gamma^5)\psi, \tag{1.1.12}$$

which leads to a formulation where left-handed particles are grouped in isospin doublets:

$$\begin{pmatrix}\nu_e\\ e\end{pmatrix}_L \quad \begin{pmatrix}u\\ d\end{pmatrix}_L, \quad \begin{pmatrix}\nu_\mu\\ \mu\end{pmatrix}_L \quad \begin{pmatrix}c\\ s\end{pmatrix}_L, \quad \begin{pmatrix}\nu_\tau\\ \tau\end{pmatrix}_L \quad \begin{pmatrix}t\\ b\end{pmatrix}_L, \tag{1.1.13}$$

while right-handed particles form singlets:

$$e_R,\ \mu_R,\ \tau_R,\ u_R,\ d_R,\ c_S,\ s_R,\ t_R,\ b_R. \tag{1.1.14}$$

A right-handed neutrino is not introduced since there is still no observation of this particle. The Lagrangian of the electroweak interactions needs to be invariant under the gauge symmetry group $SU(2)_L \otimes U(1)_Y$ and, therefore, the spinors ψ_L and ψ_R need to transform according to a non-abelian $SU(2)$ rotation and a local change of phase of $U(1)$:

$$\psi_L = e^{i\vec{\alpha}(x)\vec{\sigma}/2} e^{i\beta(x)Y}\psi_L, \tag{1.1.15}$$

$$\psi_R = e^{i\beta(x)Y}\psi_R, \tag{1.1.16}$$

where $\vec{\alpha}(x)$ is a vector of three parameters as a function of the Lorentz coordinates x, $\vec{\sigma}$ are the Pauli matrices generating SU(2), $\beta(x)$ is a real parameter and Y is the generator of the U(1) group.

From the Noether theorem, the invariance of the Lagrangian under these transformations leads to the conservation of two quantities: the *isospin* T and the *hypercharge* Y. The latter is related to the electric charge and to the third component of the weak isospin following the Gell-Mann-Nishijima relation:

$$Y = 2(Q - T_3). \tag{1.1.17}$$

[6]The concept of chirality defines whether a particle transforms under a left-handed or right-handed representation of the Poincaré group.

Moreover, in order to ensure the invariance of the electroweak Lagrangian under the fields transformations described in Eq 1.1.15 and 1.1.16, the covariant derivative is defined, taking the following form:

$$D_\mu = \partial_\mu + igW_\mu^a T_a + ig' B_\mu \frac{Y}{2}, \tag{1.1.18}$$

where T^a represents the three components of the weak isospin, obtained from the Pauli matrices as $T^a = \frac{\sigma^a}{2}$ $(a = 1, 2, 3)$, and Y the group generator of weak hypercharge. Furthermore, the condition of gauge invariance of the Lagrangian introduces also four gauge bosons, three related to the $SU(2)_L$ group: W_μ^a $(a = 1, 2, 3)$, and one for $U(1)_Y$: B_μ, where the coupling constants between the fermions and these new bosons are indicated as g and g' respectively. As a result, the electroweak Lagrangian can be expressed as follows:

$$\mathcal{L} = i\bar{\psi}_L \gamma^\mu D_\mu \psi_L + i\bar{\psi}_R \gamma^\mu D_\mu \psi_R - \frac{1}{4} W_{\mu\nu}^a W_a^{\mu\nu} - \frac{1}{4} B_{\mu\nu} B^{\mu\nu}, \tag{1.1.19}$$

having introduced the tensor fields describing the three $SU(2)_L$ vector fields as:

$$W_{\mu\nu}^a = \partial_\mu W_\nu^a - \partial_\nu W_\mu^a - g\varepsilon_{abc} W_\mu^b W_\nu^c, \tag{1.1.20}$$

with ε_{abc} being the structure constant, and the tensor describing the single vector field of $U(1)_Y$ as:

$$B_{\mu\nu} = \partial_\mu B_\nu - \partial_\nu B_\mu. \tag{1.1.21}$$

Performing a linear combination of the aforementioned tensor fields, the physical fields, corresponding to the vector bosons experimentally observed in nature, can be obtained:

$$A_\mu = \sin\theta_W W_\mu^3 + \cos\theta_W B_\mu, \tag{1.1.22}$$

$$Z_\mu = \cos\theta_W W_\mu^3 - \sin\theta_W B_\mu, \tag{1.1.23}$$

$$W_\mu^\pm = \frac{W_\mu^1 \mp i W_\mu^2}{\sqrt{2}}, \tag{1.1.24}$$

where A_μ is the physical field describing the photon (γ), and Z_μ and $W_\mu^\pm$ describe respectively the observed Z^0 and $W^\pm$ vector bosons. The angle θ_W in Eq 1.1.24 represents the mixing angle of the weak interactions, referred to as weak mixing angle or Weinberg angle, and it can be written in terms of the coupling constants g and g':

$$\sin\theta_W = \frac{g'}{\sqrt{g^2 + g'^2}}, \tag{1.1.25}$$

$$\cos\theta_W = \frac{g}{\sqrt{g^2 + g'^2}}. \tag{1.1.26}$$

The mixing needed to obtain the observed $SU(2)_L$ vector bosons ensures that the $W^{\pm}$ only interact with the left-handed component of the fermionic fields, while the Z^0 boson couples to both left and right-handed particles, although with different couplings.

Finally, it can be noted that, in order to formulate a renormalisable electroweak theory without breaking the symmetry, the corresponding Lagrangian must not contain any mass terms, as shown in Eq 1.1.19. As a consequence both gauge bosons and fermions in the electroweak theory are massless, which appears to be in contrast with experimental results. This issue can be solved by generating the masses without breaking the renormalisability through the mechanism of spontaneous electroweak symmetry breaking. This mechanism is also known as Brout-Englert-Higgs mechanism, from the physicists who first theorised it, and it is briefly described in the following section.

1.1.6 The Higgs mechanism

The Brout-Englert-Higgs mechanism [14,15] solves the problem of a mass term violating the gauge invariance breaking the $SU(3)_C \otimes SU(2)_L \otimes U(1)_Y$ symmetry into $SU(3)_C \otimes U(1)_Y$ and giving mass to the weak bosons of $SU(2)_L$, while photon and gluons remain massless. For what concerns fermion masses, they are instead generated by the Yukawa interaction terms with the Higgs field, as later explained in this Section.

The Brout-Englert-Higgs mechanism first introduces an isospin doublet of complex scalar fields:

$$\phi = \begin{pmatrix} \phi^+ \\ \phi^0 \end{pmatrix} = \frac{1}{\sqrt{2}} \begin{pmatrix} \phi_1 + i\phi_2 \\ \phi_3 + i\phi_4 \end{pmatrix}. \tag{1.1.27}$$

The Lagrangian associated to this field consists of a kinetic term and a potential:

$$\mathcal{L}_{Higgs} = (D_\mu \phi)^\dagger (D^\mu \phi) - V(\phi), \tag{1.1.28}$$

where the covariant derivative is the same one introduced earlier for the electroweak theory, and the potential $V(\phi)$ assumes the following form:

$$V(\phi) = -\mu^2(\phi^\dagger \phi) + \lambda(\phi^\dagger \phi)^2 = -\mu^2|\phi|^2 + \lambda|\phi|^4. \tag{1.1.29}$$

This potential contains a mass term with constant μ^2, and a self-interaction term with coupling constant λ, which has to be positive in order to allow the energy to be bounded from below. Depending on the sign of μ the corresponding minimum of the potential can be degenerate or not, and therefore the potential assumes different shapes. If $\mu^2 > 0$ the potential has a minimum at $\phi_1 = \phi_2 = \phi_3 = \phi_4 = 0$ corresponding to the ground state, i.e the vacuum. This means that the ground state has zero vacuum expectation value, and therefore the $\mathcal{L}_{Higgs}$ describes a scalar particle with mass μ^2 and massless gauge bosons. On

the other hand, if $\mu^2 < 0$ the minimum is degenerate on the hyper-surface defined by the condition: $\phi^\dagger\phi = \sqrt{\frac{-\mu}{\lambda}}$. Therefore, the ground state has a non-zero vacuum expectation value and the potential shows the characteristic "Mexican hat" shape (see Figure 1.2). The symmetry breaking is then obtained choosing the ground state to be $\phi_1 = \phi_2 = \phi_4 = 0$ and $\phi_3 = \sqrt{\frac{-\mu^2}{\lambda}} = \nu$, such that:

$$\phi(x) = \frac{1}{\sqrt{2}} \begin{pmatrix} 0 \\ \nu \end{pmatrix}. \tag{1.1.30}$$

This ground state can be then expanded by applying a perturbation theory parametrised by four scalar fields θ_1, θ_2, θ_3, and $h(x)$, as follows:

$$\phi(x) = \frac{1}{\sqrt{2}} \begin{pmatrix} \theta_1 + i\theta_2 \\ \nu + h(x) - i\theta_3 \end{pmatrix}. \tag{1.1.31}$$

The three scalar fields θ_1, θ_2, θ_3 are massless Goldstone bosons, which do not correspond to any particle observed in nature and can be removed with an opportune $SU(2)$ gauge transformation. As a result, $\phi(x)$ can be expressed by the remaining single massive real scalar field, the Higgs scalar field $h(x)$, as:

$$\phi(x) = \frac{1}{\sqrt{2}} \begin{pmatrix} 0 \\ \nu + h(x) \end{pmatrix}. \tag{1.1.32}$$

The kinetic term of the Lagrangian defined in Equation 1.1.28 can now be evaluated in terms of $\phi(x)$ as follows:

$$(D_\mu\phi)^\dagger(D^\mu\phi) = (\partial_\mu\phi)^\dagger(\partial^\mu\phi) + \phi^\dagger(gW_\mu \times T) + \frac{g'}{2}(B_\mu \times Y)^2\phi = \tag{1.1.33}$$

$$= (\partial_\mu\phi)^\dagger(\partial^\mu\phi) + \left(\frac{g(\nu+h)}{2}\right)^2 W_\mu^+ W^{\mu-} + \frac{1}{2}\left(\sqrt{g^2+g'^2}\frac{(\nu+h)}{2}\right)^2 Z_\mu Z^\mu, \tag{1.1.34}$$

where the observable $SU(2)$ gauge boson $W^\pm$, Z^0 defined in Equation 1.1.24 appear now with their mass terms:

$$m_W = \frac{\nu}{2}g, \;\; m_Z = \frac{\nu}{2}\sqrt{g^2+g'^2}, \tag{1.1.35}$$

which are related to the coupling constants g, g' and the vacuum expectation value $\nu = 246$ GeV. The two mass terms are also related by the following expression:

$$\frac{m_W^2}{m_Z^2 \cos^2\theta_W} = 1. \tag{1.1.36}$$

The vector gauge bosons have gained a mass, while leaving the photon massless, and a new massive scalar boson h arises. New parameters have been introduced, such as the vacuum expectation value of the Higgs field ν, which is related to the fermi constant G_F, λ and the Higgs boson mass m_H, the last two being free parameters of the theory, implying that they can only be determined experimentally.

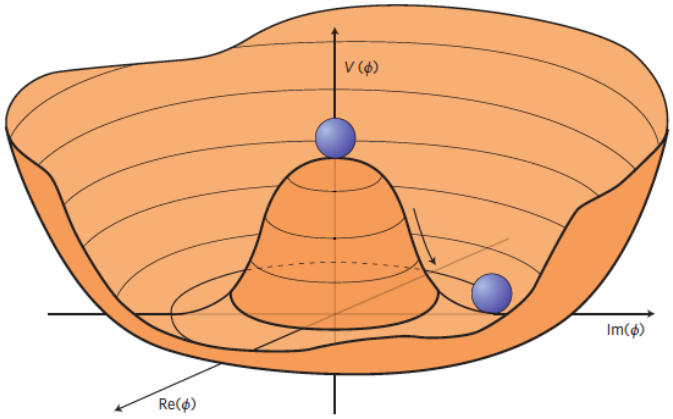

Figure 1.2: Illustration showing the Higgs potential ($V(\phi)$) in the case that $\mu^2 < 0$ and the minimum is at $|\phi^2| = \frac{-\mu^2}{2\lambda}$. The potential presents the distinctive "Mexican hat" shape. Choosing any of the points that sits at the bottom of the potential results in a spontaneous breaking of the rotational $U(1)$ symmetry.

Mass terms in the fermion sector

The fermions acquire mass by interacting with the Higgs boson field. In order to preserve the gauge invariance of the electroweak Lagrangian, the interaction with the Higgs field, and therefore the fermions mass terms, are introduced in terms of an invariant Yukawa Lagrangian of the following form:

$$\mathcal{L}_{Yukawa} = -y_f \bar{l}_L \phi l_R + h.c, \tag{1.1.37}$$

where y_f represents the strength of the Higgs boson coupling to fermions, known as Yukawa couplings, l_L represents the left-handed doublet for leptons or quarks, l_R is the correspondent right-handed singlet and ϕ is the Higgs boson field. Expanding the Higgs field around the ground state from Equation 1.1.32, the former Lagrangian can be re-written as:

$$\mathcal{L}_{Yukawa} = -y_f \frac{\nu}{\sqrt{2}} \bar{l}_L l_R - y_f \frac{h(x)}{\sqrt{2}} \bar{l}_L l_R + h.c. \tag{1.1.38}$$

It can be noticed that the Higgs boson coupling to fermions results to be proportional to the fermions mass:

$$m_f = -y_f \frac{\nu}{\sqrt{2}}. \tag{1.1.39}$$

Fermion masses are a free parameter of the theory, thus not predicted by the SM, and they are experimentally determined.

1.1.7 The Higgs boson at the LHC

The Higgs boson can be produced at the LHC via several mechanisms involving quark or gluon initiated collisions. The four main processes are, ordered by decreasing cross-section values: gluon-gluon fusion (ggF), vector boson fusion (VBF), associated production with a vector boson (VH) and associated production with top quarks ($t\bar{t}H$). The corresponding Feynman diagrams are shown in Figure 1.3.

The ggF process is the production mechanism with the highest cross-section, $\sigma \approx 48.61$ pb, for a Higgs boson with mass $m_H = 125$ GeV at $\sqrt{s} = 13$ TeV [16], and accounting for $\approx 88\%$ of the total Higgs production cross-section at the LHC. Although the ggF mechanism is the dominant production process, it can be experimentally challenging to be studied as the Higgs boson represents the only particle produced in the process. The VBF production has the second largest cross-section, $\sigma \approx 3.77$ pb [16], and is characterised by a clear experimental signature represented by the presence of two energetic jets. In the VH production process, the Higgs boson is produced in association with a W or Z vector-boson. Although its cross-section is fairly small, $\sigma \approx 2.24$ pb [16], it offers a very clear experimental signature when considering the leptonic decay of the vector boson V. Lastly, $t\bar{t}H$ has a cross-section of $\sigma \approx 0.51$ pb [16]. The importance of this production mode is represented by the fact that it allows to probe directly the top-Higgs Yukawa coupling.

In the analysis presented in Chapters 5 and 6, the Higgs boson production mechanism considered are the ggF and WH ones. In addition, there is an ongoing ATLAS effort to exploit also the VBF production that is planned to be further combined to the results obtained by the analysis described in this thesis.

1.2 SM limitations and BSM physics

The SM has been tested with great precision and it has proven to be extremely successful in correctly describing and predicting a large number of physics processes. Among its successes, is worth mentioning the discovery of the Higgs boson by the ATLAS [17] and CMS [18] collaborations at the Large Hadron Collider [19], announced in 2012, which represented a crucial step in the history of particle physics.

Despite its success, the SM fails in giving an explanation for many open questions and

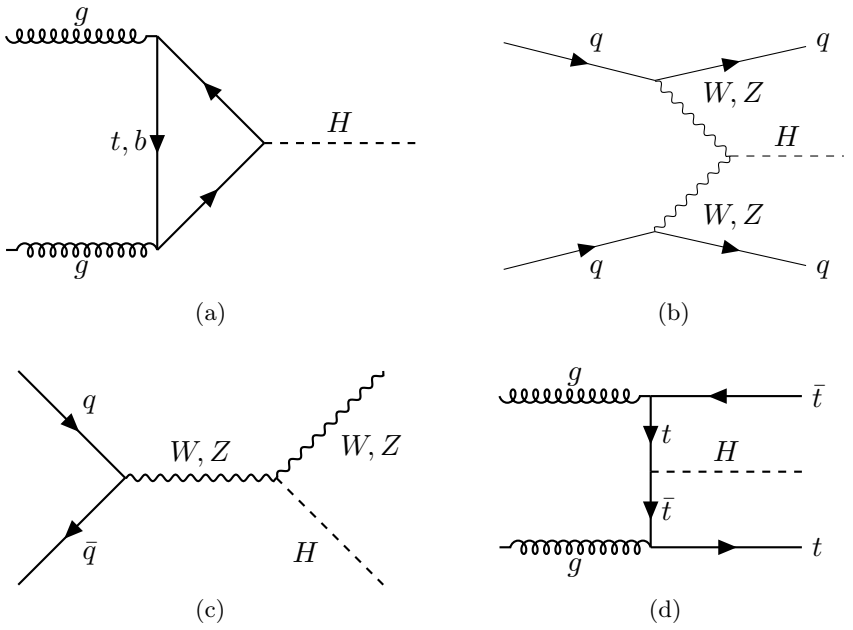

Figure 1.3: Feynman diagrams of the four main production modes for the Higgs boson at the LHC: (*a*) gluon-gluon fusion, (*b*) vector-boson fusion, (*c*) associated production with a vector boson and (*d*) associated production with a top quark.

experimental observations. Some of these are briefly discussed in the following.

One of the main shortcomings is the so-called *hierarchy problem*, which arises from the large discrepancy between the weak and gravitational energy scale [20]. The relatively small Higgs boson measured mass leads to a substantial level of fine tuning in the model, since it requires large cancellations between different terms appearing in the radiative corrections to the Higgs mass. Substantial fine tuning would require new physics at the TeV scale, or the presence of an underlying extended theory.

Another issue comes from the fact that neutrinos are supposed to be massless in the SM, but experimental observations of neutrino oscillations implies that they do have mass. Moreover, upper limits on neutrino masses implies that they are much smaller than the ones of the other particles of the SM. Both can be explained only by BSM physics.

Another shortcoming of the SM is related to the observation that there is significantly more matter than anti-matter in our Universe. If this asymmetry has manifested during the early phases of the Universe, it can only be justified in the SM by a significant violation of the Charge-Parity (CP) symmetry. CP-violation has been observed in the SM, but it is not sufficient to justify the asymmetry, which therefore requires BSM physics explanations.

Finally, an additional observation that hints to BSM physics is due to the experimental cosmological and astrophysical observations suggesting that ordinary matter accounts for only $\sim 5\%$ of the total mass-energy of the Universe. These observations suggest that the Universe is composed for up to $\sim 25\%$ of Dark Matter (DM) [21], which is only inferred through gravitational interaction. DM composition and interactions with SM particles

are still unknown and represents one of the main challenges to unveil BSM physics. The remaining $\sim$ 70% of the Universe energy consists instead of the so-called Dark Energy, which is hypothesised to lead to a repulsive gravitational-like force that tends to accelerate the expansion of the Universe.

Many theoretical models provide a solution to one, or more, of the aforementioned problems and are tested by experimentalists at the LHC in searches for new physics. Unfortunately, at the time this thesis has been written, no evidence supporting one of these BSM physics models has been observed yet. This can be due to the fact that not enough data has been collected yet, or that simply the BSM physics energy scale is beyond the current reach of the LHC. However, another option on the table regards the fact that, maybe, BSM physics is just hiding in plain sight in a phase space currently uncovered by searches for new physics at the LHC. The analysis work described in this thesis sits in this scenario, and in particular in exploring the uncovered regions in the *lifetime frontier* at the LHC.

1.2.1 Long-Lived particles: a different look into BSM physics

The vast majority of searches for new physics BSM at the LHC focus on promptly-decaying particles. However, looking at the SM, particles have lifetimes[7] spanning many orders of magnitude, as it is shown in Figure 1.4. Similarly, BSM theories often predict new particles with a variety of masses and lifetimes. For instance, the long lifetime of a particle can originate by its interactions, which may have a small coupling constant or have a small phase space accessible. Therefore, it cannot be excluded that BSM physics is rich in so-called Long-Lived Particles (LLPs).

Scenarios involving the presence of LLPs have been less extensively explored, and there are still many viable regions of parameter space, which are accessible at LHC energies, that are left uncovered. However, LLPs can in principle travel macroscopic distances in the detector and therefore be extremely challenging to detect, since they can yield a variety of unconventional signatures. Some of the possible LLPs signatures that can be observed in LHC experiments are shown in Figure 1.5 and include: displaced vertices, localised energy deposits in the calorimeter without associated tracks, displaced leptons and lepton pairs, etc.

Targeting these unconventional signatures means that many uncovered BSM scenarios can be explored, but this also implies very often the need for the development of dedicated triggers or object reconstruction algorithms. Moreover, this kind of signatures are also usually very likely to be mimicked by mis-reconstructed objects and detector noise, which limit the use of simulated Monte Carlo events for the background estimation.

For all these reasons, the search for LLPs is still nowadays an extremely challenging topic at modern high energy physics experiments.

[7] In the following, the terms lifetime and mean proper lifetime will be treated as equal, and will both indicate the proper decay time in the frame of reference of the particle.

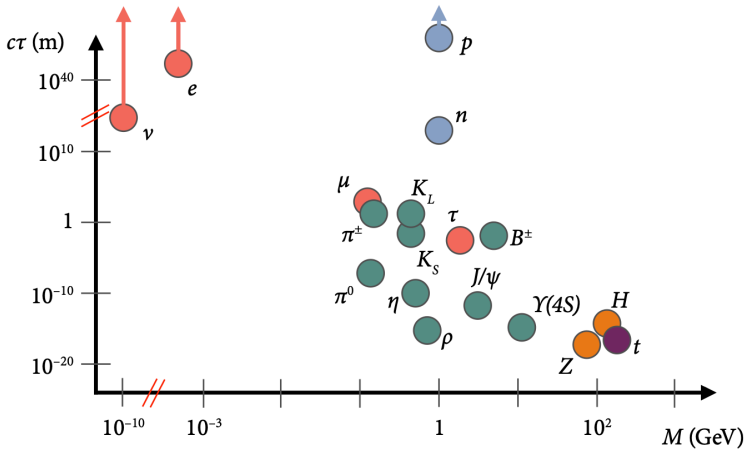

Figure 1.4: Mean proper lifetime, $c\tau$ in meters, as a function of the mass, M in GeV, for different SM particles: baryons (blue), mesons (green), leptons (red), bosons (orange), and quarks (purple). Figure from [22].

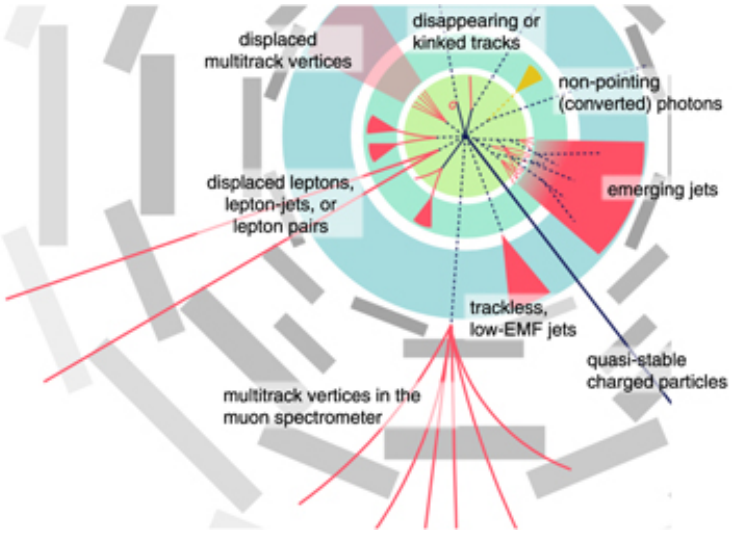

Figure 1.5: Schematic view illustrating the variety of challenging and unconventional experimental signatures that can result from BSM LLPs in general purpose detectors at particle colliders, such as the ATLAS experiment at LHC. In figure the cross-sectional plane in azimuthal angle, ϕ, of the detector is shown. Figure from [23].

1.2.2 Dark sectors

Several BSM theoretical models predict the existence of a complex spectrum of new particles that form a so-called *dark sector*. In order to observe processes involving these new particles, there must be a *portal* that connects the dark sector to the SM. In this scenario, depending on the strength of the coupling to the SM, unstable dark states may be produced, resulting in the presence of LLPs that could decay into SM particles.

There are several ways in which a portal between a dark sector and the SM can occur. It usually includes the presence of one or more dark sector mediator particles coupled to the

SM. The interactions between the two sectors depends on the mediator spin and parity. This mediator can either be a vector, a scalar, a fermion, or a pseudoscalar, and it determines the kind of portal relevant for the interactions between SM and dark sector. There are mainly four portals that are usually considered, depending on the nature of the mediator: vector portal (vector mediator) [24], Higgs portal [25] (scalar mediator), neutrino portal [26] (fermionic mediator), and axion portal [27] (pseudoscalar mediator). Those are arguably the most important ones to consider when discussing dark sectors. In what follows, the focus will be on the vector portal and the Higgs portal, as these are the portals of interest for the analysis presented in this thesis.

The Vector Portal

In the vector portal we have a dark sector charged under a new $U(1)_D$ symmetry involving the presence of a vector mediator particle, referred to as dark-photon (γ_d), coupled to the SM photon via a kinetic mixing term[8] of the following form:

$$\mathcal{L} \supset \frac{1}{2}\varepsilon F'_{\mu\nu}F^{\mu\nu}, \tag{1.2.1}$$

where $F'_{\mu\nu}$ is the tensor field of the dark-photon and ε the arbitrary coupling constant [1]. The dark-photon is considered to be massive in order to have a mean proper lifetime. Moreover, in the following it is assumed that no dark state particles exist below the dark-photon mass, and that it exclusively decays in pairs of charged SM fermion via kinetic mixing[9].

In this scenario, if the dark-photon has a mass $m_{\gamma_d} > 2m_e$, its decay width into pair of charged leptons can be expressed as:

$$\Gamma_{\gamma_d \to l\bar{l}} = \frac{1}{3}\alpha\varepsilon^2 m_{\gamma_d}\sqrt{1-\frac{4m_l^2}{m_{\gamma_d}^2}}\left(1+\frac{2m_l^2}{m_{\gamma_d}^2}\right), \tag{1.2.2}$$

where m_{γ_d} is the dark-photon mass and m_l the mass of the charged lepton considered. If the dark-photon has a mass $m_{\gamma_d} > 2m_\pi$, then it can decay also to quarks and the respective decay width can be written in terms of the ratio:

$$R = \frac{\sigma_{e^+e^-\to hadrons}}{\sigma_{e^+e^-\to\mu^+\mu^-}}, \tag{1.2.3}$$

[8] A similar phenomenology can be obtained assuming that the vector portal between the dark sector and SM is given by a kinetic mixing between the hypercharge electroweak boson B and the dark-photon [28].

[9] The case where the dark-photon is the lightest particles of the hidden sector represents only a subset of the vector portal models. However, this is the scenario that is usually investigated at the LHC, as it involves the possibility of observing dark-photon decays to SM particles. More generally, if the dark-photon is not the lightest particle of the hidden sector, it can decay to dark matter candidates. The latter is investigated by many other non-LHC and non-collider experiments [24].

evaluated at $\sqrt{s} = m_{\gamma_d}$, as:

$$\Gamma_{\gamma_d \to hadrons} = \Gamma_{\gamma_d \to l\bar{l}} \cdot R(\sqrt{s} = m_{\gamma_d}). \tag{1.2.4}$$

As a result of the decay widths defined above, the branching fraction of the dark-photon to SM fermions, depending on its mass, assumes the values shown in Figure 1.6. Consequently, the dark-photon mean proper lifetime (τ_{γ_d}) can be expressed, in seconds, as a function of the coupling and mediator mass, in a good approximation, as:

$$\tau \propto \left(\frac{10^{-4}}{\epsilon}\right)^2 \left(\frac{100\,MeV}{m_{\gamma_d}}\right)^2 [s]. \tag{1.2.5}$$

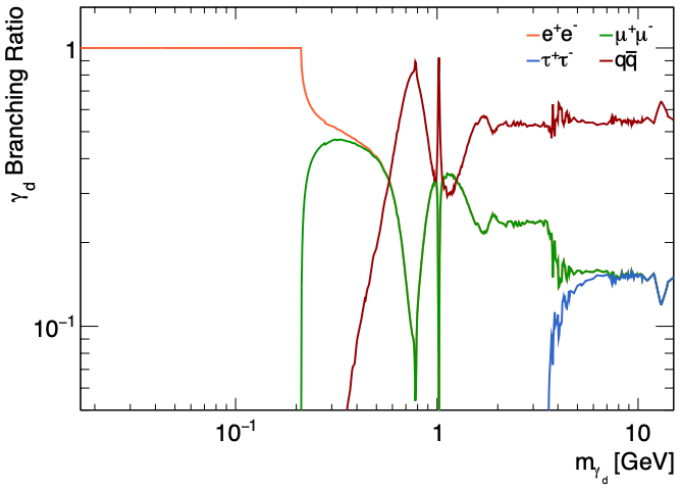

Figure 1.6: Dark photon branching ratio to a pair of charged leptons or quarks. Figure adapted from [1].

Dark sector models of the form described in this section are referred to as simplified models. These models are not the starting point of a theory, but are simple SM extensions focused on the experimental signature, which eventually would arise as a limit of a complete theory.

Accessing the dark sector through the Higgs boson: the Higgs portal

In models of the form described above, involving the presence of a massive dark-photon, the structure of the Higgs sector is modified. An additional term for a Higgs-like boson (H'), with a non-zero vacuum expectation value, should be added to the Lagrangian in addition to the kinetic and interaction terms of the dark-photon. Introducing the field ϕ' related to this new BSM Higgs-like boson, a new potential V should be included in the Lagrangian, assuming the following form:

$$V(\phi, \phi') = -\mu^2(\phi^\dagger\phi) + \lambda(\phi^\dagger\phi) - \mu'^2(\phi'^\dagger\phi') + \lambda'(\phi'^\dagger\phi') + \kappa(\phi^\dagger\phi)(\phi'^\dagger\phi'), \tag{1.2.6}$$

with κ representing the coupling between the SM and BSM Higgs fields.

In an analogous way to what happens for the SM, the electroweak symmetry breaking gives a non-zero vacuum expectation value to the field ϕ', generating the mass terms of the dark sector particles.

In this context, the interaction between the two fields enables decays of the SM Higgs boson into a pair of dark-photons, or other dark sector particles charged under $U(1)_D$, via the so-called *Higgs portal*.

Considering a search for long-lived dark-photons, which represents the focus of this thesis work, being able to access the Higgs portal represents a great opportunity, since this allows to not use the vector portal for both production and decay of the dark-photon. In this way, instead of having to take into account a factor ε^2 in the process, the vector portal coupling is exploited only for the dark-photon decay. Moreover, instead of considering the coupling κ for the dark-photon production via Higgs portal, another parameter is used, which is the branching ratio of the invisible decay of the SM Higgs boson ($B_{H\to inv}$). In the SM, the only way in which the Higgs boson can decay in invisible particles is through the $H \to ZZ^* \to 4\nu$ process, which is predicted to be $B_{H\to ZZ^*\to 4\nu} = B_{H\to inv} = 10^{-3}$. At the time this thesis was written, the constraint on this parameter [29] corresponded to $B_{H\to inv} < 11\%$ @ $95\,\%\, CL$. A larger value of the $B_{H\to inv}$ with respect to the one predicted by the SM could represent an hint of possible Higgs boson decays involving non-SM particles, such as long-lived dark-photons.

Considering the possibility of dark-photons produced via the Higgs portal and decaying through a vector portal allows to explore a previously uncovered region of the parameter space, part of which is accessible in searches for long-lived dark-photons at the LHC. The phase space covered in this way is complementary to the one previously explored by other dark-photon searches (see Figure 1.7), in which a vector portal for both the production and decay of the dark-photon is assumed.

1.2.3 Benchmark models

In the last part of this chapter details are given about the BSM physics processes that are considered as benchmark models for the analysis work detailed in this thesis. Two models are used for the optimisation of the event selections and the interpretation of the final results: the *Falkowski-Ruderman-Volansky-Zupan* (FRVZ) model [30, 31] and the *Hidden Abelian Higgs Model* (HAHM) [28]. In both models, the SM and dark sectors communicate through the Higgs portal for the production of the BSM particles and through a vector portal for the decay of the produced particles.

FRVZ model

In the FRVZ model a pair of dark fermions, f_d, charged under the $U(1)_D$ symmetry, is produced via an exotic decay of the Higgs boson and can lead to final states involving

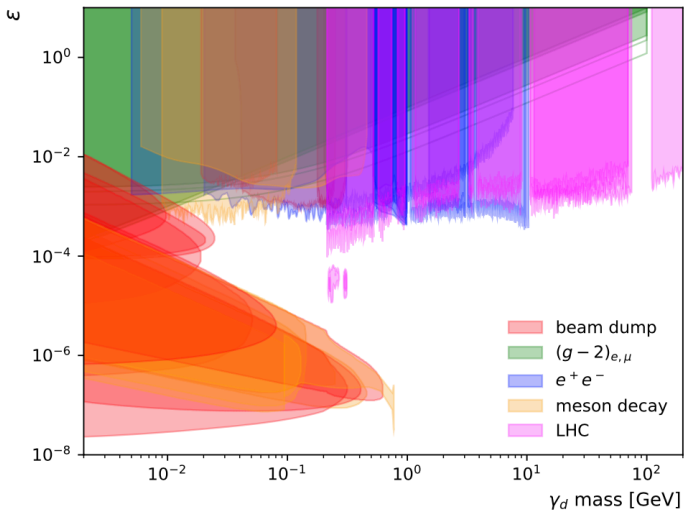

Figure 1.7: Two-dimensional plane as a function of dark-photon mass (m_{γ_d}) and kinetic mixing parameter (ε), where recent constraints set on dark-photon decays are reported for different experiments. Results are shown for beam dump experiments (red), muon and electron magnetic moment (green), experiments at e^+e^- colliders (blue), meson decay (yellow) and LHC experiments (magenta). Part of the phase space left uncovered is accessible in searches for long-lived dark-photons at the LHC, such as the one described in this thesis. References for each of the constraint shown are available in [1].

the presence of either two or four dark-photons, as shown in Figure 1.8. In the two dark-photon case (see Figure 1.8a), the dark fermion decays into a dark-photon and a stable dark fermion, which is assumed to be the *Hidden Lightest Stable Particle* (HLSP) of the dark sector. In the four dark-photon case (see Figure 1.8b), each dark fermion decays into an HLSP and a dark scalar, s_d, that in turn decays into a pair of dark-photons. Moreover, depending on the value of the $U(1)_D$ coupling [32], more dark-photons can be radiated, leading to showers of dark-photons that yield a large number of displaced fermions. For the analysis described in this thesis, the coupling of the $U(1)_D$ is assumed to be less than 0.01, hence the radiation of additional dark-photons is suppressed.

The FRVZ model enables to explore many different kinematic scenarios, controlling the dark sector mass spectrum and the couplings. This is achieved through the presence of intermediate hidden sector particles, with the HLSP mass that determines the amount of missing transverse momentum in the final state, and the dark fermions regulating the boost and the opening angle of the dark-photons in the final state. These characteristics are of particular interest in searches for LLPs at hadron colliders. In the analysis described in Chapters 5 and 6, the masses of the hidden sector intermediate particles, i.e. HLSP, dark fermions and dark scalars, are chosen to be small with respect to the Higgs boson mass and far from the kinematic thresholds in order to achieve a boosted configuration for the final state particles.

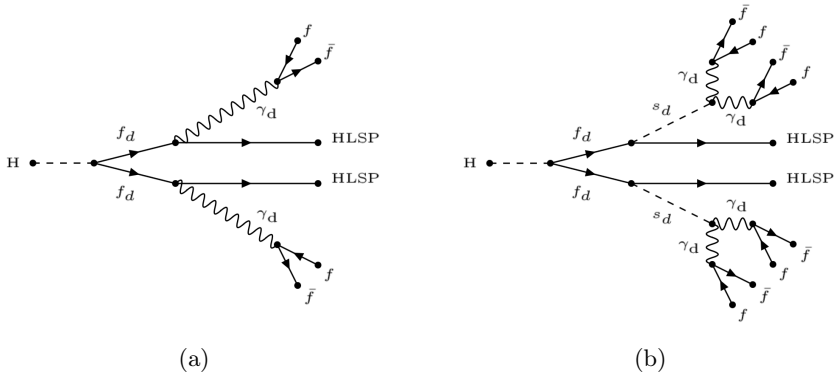

Figure 1.8: Diagrams illustrating the two FRVZ model [30, 31] processes of interest for the dispalced dark-photon jet analysis. In (a), the FRVZ process shown involves the exotic decay of the Higgs boson to a pair of dark fermions, f_d, which subsequently decay into an HLSP and a dark-photon. In (b), the dark fermions decay into an HLSP and a dark scalar, s_d, that in turn decays into a pair of dark-photons. In both diagrams, the dark-photon subsequently decays to pair of charged SM fermions, denoted by f and $\bar{f}$.

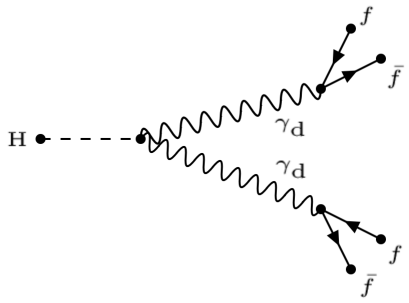

Figure 1.9: Diagram illustrating the HAHM model [28] process considered for the displaced dark-photon jet analysis. The process involves the direct production of two dark-photons from a Higgs boson decay. The dark-photon decays to pair of charged SM fermions, denoted by f and $\bar{f}$.

HAHM model

The HAHM model provides the simplest known minimal setup for a dark sector involving dark-photons produced via exotic decays of the Higgs boson. When comparing it to the FRVZ model, the main difference is that the HAHM model predicts a direct decay of the Higgs boson into a pair of dark-photons, as shown in the diagram presented in Figure 1.9. As for the FRVZ case, this model predicts the production of dark-photons via the Higgs portal, while their decay to SM charged fermions is made possible via the vector portal.

The absence of intermediate dark sector particles in the considered process allows for the production of two highly boosted dark-photons. This feature can be exploited in searches for LLPs at hadron colliders, as it allows for a better identification of the dark-photon decay products.

Chapter 2

The LHC and the ATLAS experiment

The physics analysis described in this thesis work makes use of the data collected by the ATLAS detector, one of the four main experiments situated around the Large Hadron Collider [33], the worlds largest and most powerful particle accelerator. In this chapter, the LHC is introduced together with the ATLAS detectors structure and functionalities.

2.1 The Large Hadron Collider (LHC)

The LHC is located at CERN (Conseil Européen pour la Recherche Nucléaire) near Geneva, Switzerland. The LHC was constructed between 1998 and 2008 and it replaced the Large Electron-Positron collider inside a 27 km long circular tunnel, which is located around 100 m below ground level, crossing the border between Switzerland and France. Both protons and heavy ions can be accelerated in opposite directions within the LHC beam pipes.

The LHC has been in maintenance shutdown since November 2018, after having operated for a three year period at 7 TeV in 2010-2011 and at 8 TeV in 2012, called Run-I, and for a four year period at 13 TeV in 2015-2018, called Run-II. The LHC has resumed operation in the second half of 2022 for the so called Run-III data-taking period.

The work presented in this thesis makes use of the data taken in the Run-II period.

2.1.1 CERN accelerator complex

The CERN laboratory hosts a complex of several accelerators. There, the proton beams are created and accelerated by a sequence of sub-accelerators to the final centre-of-mass energy and collided at different interaction points of the main accelerator, the LHC. A schematic of the CERN accelerator complex [34] is shown in Figure 2.1. Protons are first created from a source of ionised hydrogen atoms and then injected into the first linear accelerator (LINAC2), where they are accelerated up to an energy of 50 MeV before passing in a sequence of circular accelerators. The beam accelerates subsequently through the first circular accelerator, the Proton Synchroton Booster (PSB), reaching an energy of 1.4 GeV,

the Proton Synchrotron (PS), arriving at an energy of 25 GeV, and finally the Super Proton Synchrotorn (SPS), reaching the target energy of 450 GeV. The last acceleration step happens in the LHC where the proton beam reaches the nominal energy.

The collision points host four experiments: ATLAS [35] (A Toroidal LHC ApparatuS) and CMS [36] (Compact Muon Solenoid), which are two multi-purpose experiments, ALICE [37] (A Large Ion Colliding Experiment), designed to study heavy nuclei interactions, and LHCb [38], focused on the study of b-physics.

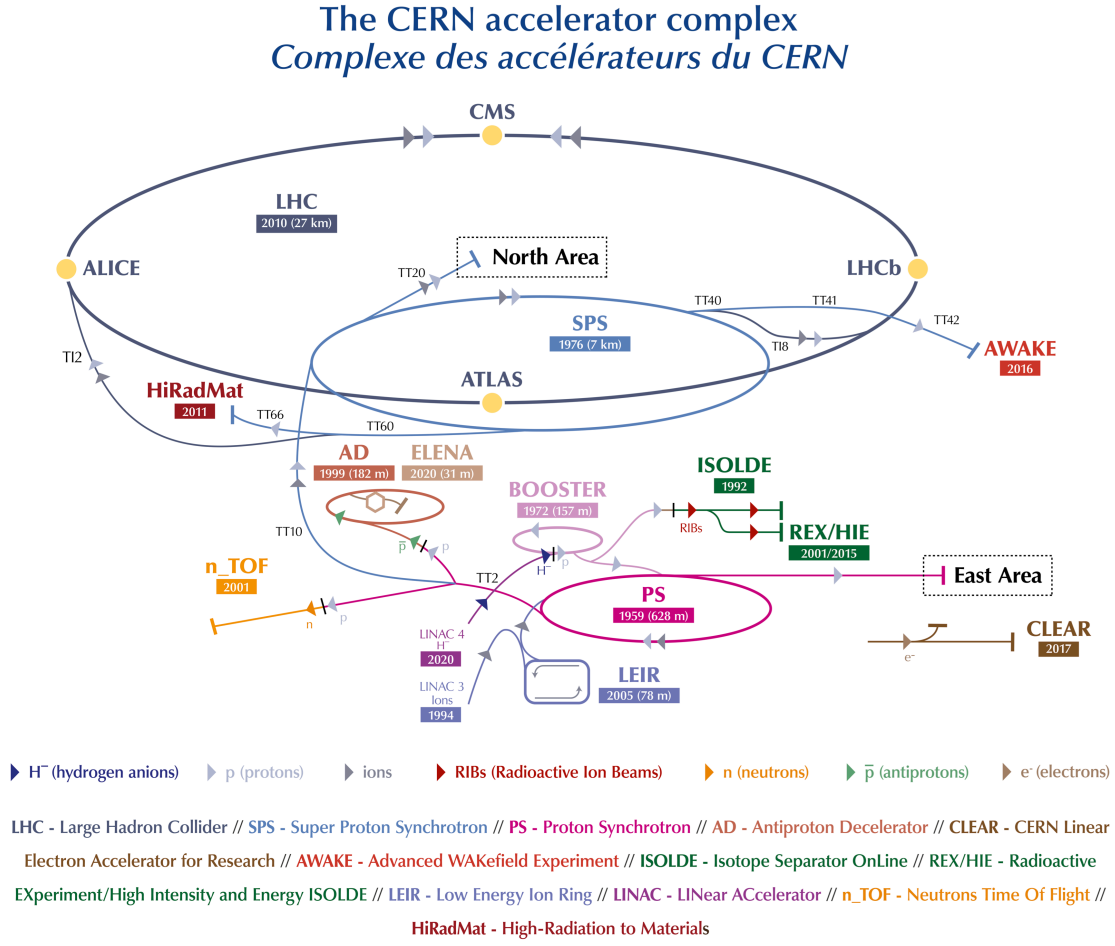

Figure 2.1: Scheme of the CERN accelerator complex and of a subset of the many experiments supported by these accelerators [39].

2.2 Luminosity and pile-up

The proton beams enter the LHC divided in bunches at a frequency of 40 MHz, hence separated in time by 25 ns. The bunch fill pattern is designed to maximise the rate of the collisions for a total of 2556 proton filled bunches in Run-II, out of a maximum allowed of

2808. The number of collisions that can be produced in a particle collider per cm^2 and per second is defined by the instantaneous luminosity, computed as:

$$\mathcal{L} = \frac{N_b^2 n_b f_{rev}}{4\pi\sigma_x\sigma_y} \cdot F \tag{2.2.1}$$

The instantaneous luminosity [33] depends only on the machine characteristics and not on specific physics processes, thus it is a useful parameter when comparing the performance of different accelerator machines. It is proportional to the bunch revolution frequency f_{rev}, the number of colliding particles contained in each bunch, N_b, times the number of bunches, n_b. It is inversely proportional to the root mean square of the beam width in the x and y directions, σ_x and σ_y. Finally, the instantaneous luminosity is corrected by a geometrical factor F which takes into account the crossing angle with which the beams are collided. The total luminosity delivered over a time period is called integrated luminosity and is computed as:

$$\mathcal{L}_{int} = \int \mathcal{L} dt \tag{2.2.2}$$

This is used to quantify the amount of data delivered by the LHC and recorded by the experiment. In Figure 2.2, the integrated luminosity recorded by the ATLAS experiment during Run-II is shown. In this period of data-taking, the LHC delivered 156 fb^{-1} of pp collisions of which ATLAS recorded 147 fb^{-1}, and 139 fb^{-1} are good for physics analysis use.

Pile-up

The very high luminosity delivered by the LHC means that the environment in which the detector and trigger systems have to operate is challenging, having to cope with hundreds of particles in each collision. This shows up in two effects, namely the in-time pile-up, occurring when multiple collisions take place during the same bunch crossing, and the out-of-time pile-up, occurring when the system reads out for a time span longer than the time between two bunch crossings. Pileup effects can be described using as a parameter the average number of interactions per bunch crossings, $\langle\mu\rangle$, computed as follows:

$$\langle\mu\rangle = \frac{L \cdot \sigma_{inelastic}}{n_b \cdot f_{rev}}. \tag{2.2.3}$$

The luminosity-weighted distribution of the mean number of interactions per bunch crossing for the Run-II data-taking is shown in Figure 2.3.

2.3 ATLAS overview

ATLAS is one of the two general purpose detectors and is the largest of all of the LHC experiments, measuring 44 m in length and 25 m in width and weighting around 7000 tons.

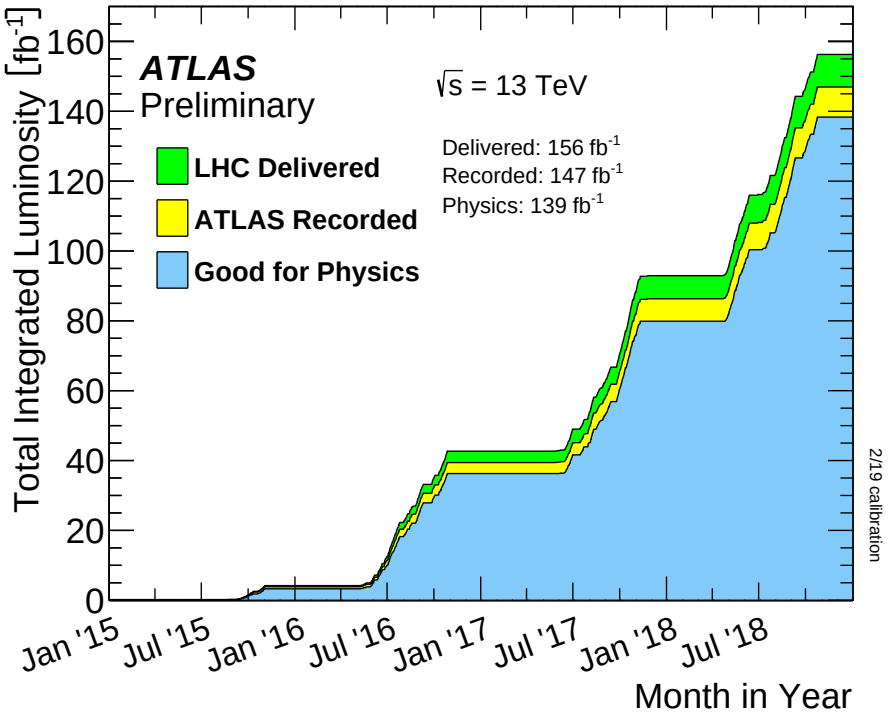

Figure 2.2: Cumulative luminosity versus time delivered to ATLAS (green), recorded by ATLAS (yellow) and determined to be good quality data (blue) during stable beams for pp collisions at 13 TeV centre-of-mass energy in LHC Run-II [40].

The ATLAS detector is designed to provide a near-full 4π coverage in solid angle with tracking and calorimetry through multiple detector subsystems. In Figure 2.4, a schematic diagram of the ATLAS detector and its major subsystems is shown. It can be seen that it is structured in three concentric cylindrical sub-detectors which surround the pp interaction point. The innermost part is the inner detector (ID), which is capable of tracking with high precision all charged particles produced in collisions and enables to reconstruct the vertices of interaction. The ID is followed by the calorimeter system, which comprises an electromagnetic sub-system (ECAL), designed for the identification of electromagnetic showers, and an hadronic sub-system (HCAL), designed to perform an accurate energy measurement of jets and missing transverse momentum. Finally, the muon spectrometer (MS) is dedicated to the identification and high precision measurement of muons and their momentum.

ATLAS coordinate system

ATLAS uses a right-handed coordinate system with the z-axis along the beam pipe, the origin at the interaction point, which is the centre of the detector, and the perpendicular x-y plane, where the positive x-semi-axis points towards the centre of the ring and the positive y-semi-axis points upwards. A reference in cylindrical coordinates, as shown in Figure 2.5,

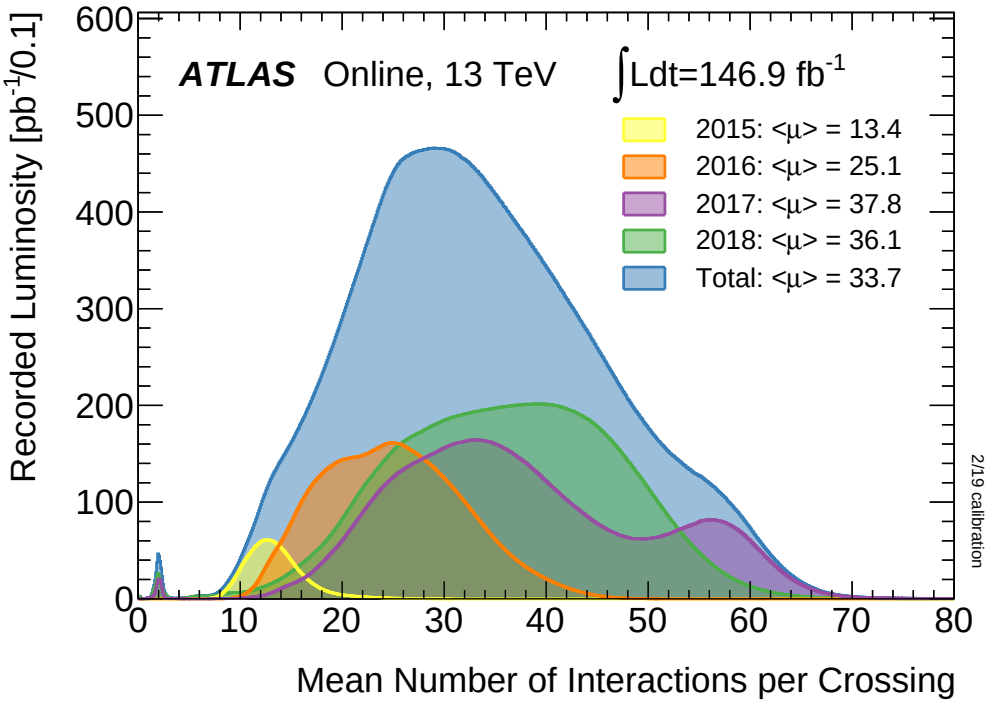

Figure 2.3: The figure shows the luminosity-weighted distribution of the mean number of interactions per crossing for the full Run-II pp collision data-taking at 13 TeV centre-of-mass energy [40].

is also considered, defined by the azimuthal angle ϕ, measured around the beam, and the polar angle θ, measured with respect to the beam axis. Useful kinematic variables can then be defined in this coordinate system to be invariant under Lorentz boost along the longitudinal axis, as in hadron colliders the momentum along the z-axis of the initial system is unknown. An example is the rapidity, which can be defined as:

$$y = \frac{1}{2} \ln \frac{E + p_z}{E - p_z}, \tag{2.3.1}$$

where E is the energy of the particle and p_z is the momentum along the z-axis. In the case where the particle is travelling close to the speed of light, or equivalently in the approximation that the mass of the particle is negligible, we can define another quantity, called pseudorapidity, as follows:

$$\eta = -\ln(tan\frac{\theta}{2}). \tag{2.3.2}$$

Differences in pseudorapidity between particles are independent of the momentum of the colliding partons, which makes η a useful observable. We can define the distance, ΔR,

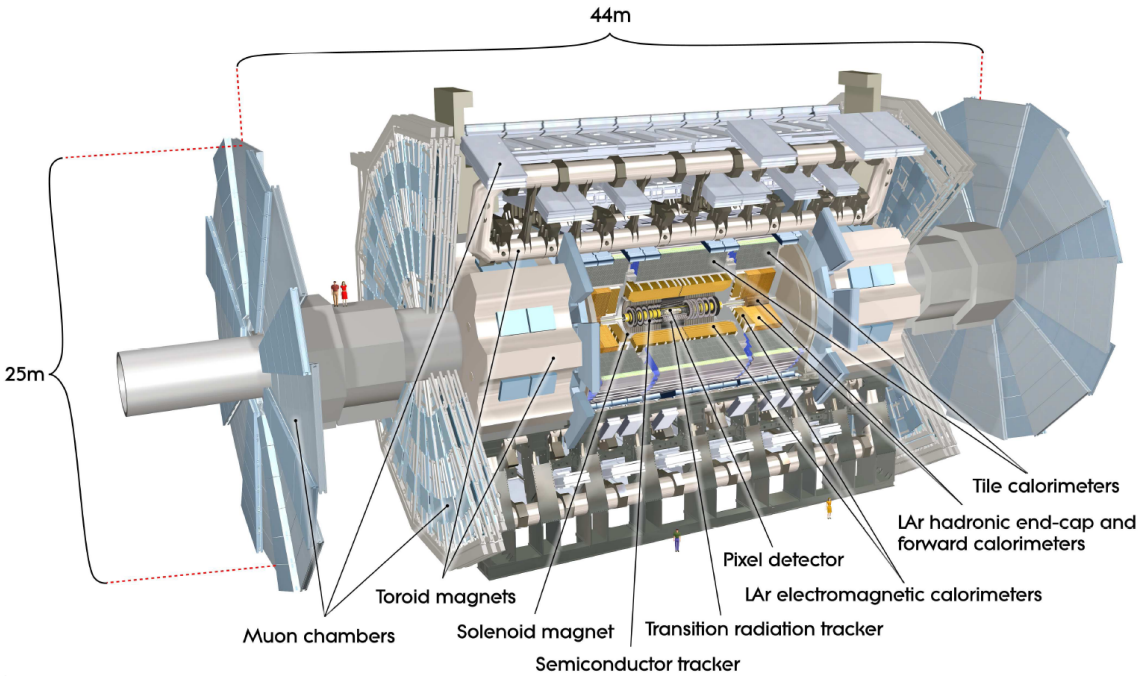

Figure 2.4: Cut-away diagram of the ATLAS detector and its major subsystems [35].

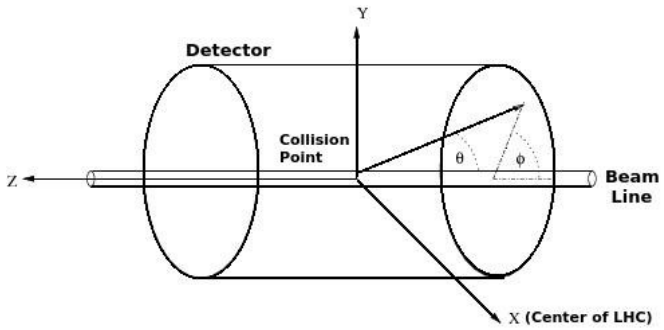

Figure 2.5: Illustration of the ATLAS detector coordinate system.

between objects in the $\eta - \phi$ space as:

$$\Delta R = \sqrt{\Delta\eta^2 + \Delta\phi^2}. \tag{2.3.3}$$

As the partons are highly boosted in the z-direction, and the partonic momentum fraction is not exactly known, object measurements are usually made in the plane perpendicular to the beam, the transverse plane, where we can define two other useful observables: the transverse momentum (p_T) and transverse energy (E_T) of an object as $p_T = psin\theta$ and $E_T = Esin\theta$, respectively.

2.4 Magnet system

A particle with charge q moving at a velocity v through a magnetic field of strength $|\vec{B}|$ experiences a Lorentz force, expressed as:

$$\vec{F} = q\vec{v} \times \vec{B}, \tag{2.4.1}$$

Following the Lorentz force, the momentum of a charged particle entering perpendicularly a magnetic field can be measured by the curvature radius, which is a measure of the deflection of the particle trajectory by the magnet system.

A consequence of this is that, in order to measure high-p_T particles, an intense magnetic field is needed. The ATLAS detector contains the worlds largest superconducting magnet system [41], shown schematically in Figure 2.6, and it is composed of the following superconducting magnets:

- Central Solenoid: provides a 2 T axial magnetic field to the inner detector;
- Barrel Toroid: air-core system that provides a 0.5 T magnetic field in the barrel region of the muon spectrometer;
- End-caps Toroid: air-core system that provides a 1.0 T magnetic field in the end-cap region of the muon spectrometer.

The choice of using an air-core toroid system in ATLAS was made to reduce to a minimum all possible particle interactions with the system material along the flight-path, allowing a precise measurement of the trajectory. The superconductivity of the magnet system is achieved using liquid helium cooled to around 4.5 K.

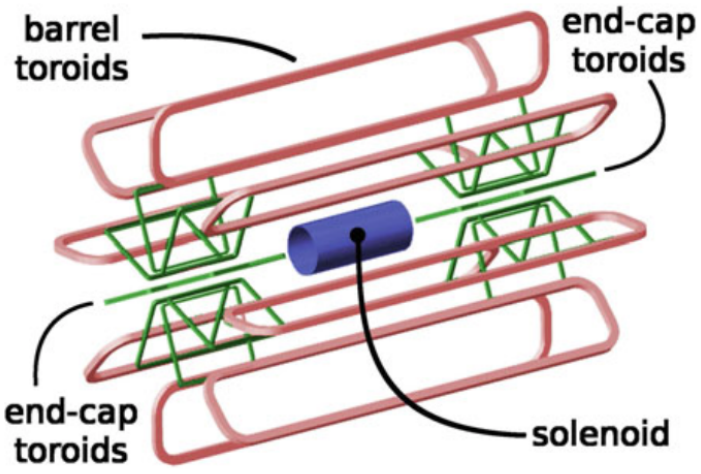

Figure 2.6: Illustration of the ATLAS detector magnetic system [41] with the central solenoid shown in blue, the barrel toroids in red and the end-cap toroids in green.

2.5 Inner Detector

The ATLAS inner detector [42], shown in Figure 2.7, is a tracking detector and is the closest system to the beam pipe. It is immersed in a 2 T magnetic filed provided by the central solenoid, and is responsible for the reconstruction of charged particle tracks and their production vertex. It extends from 33 mm to 1082 mm in radius (see Figure 2.8) and covers the pseudorapidity region of $|\eta| \leq 2.5$. A detector which operates so close to the interaction point needs to be extremely radiation resistant, having to cope with a total fluence of $\approx 1 \times 10^{15}\ n_{eq}/cm^2$ by the end of Run-II, which corresponds to the total luminosity of 159 fb^{-1} delivered by the LHC. The inner detector consists of three different sub-detectors: the pixel detector, the Semiconductor Tracker (SCT) and the Transition Radiation Tracker (TRT).

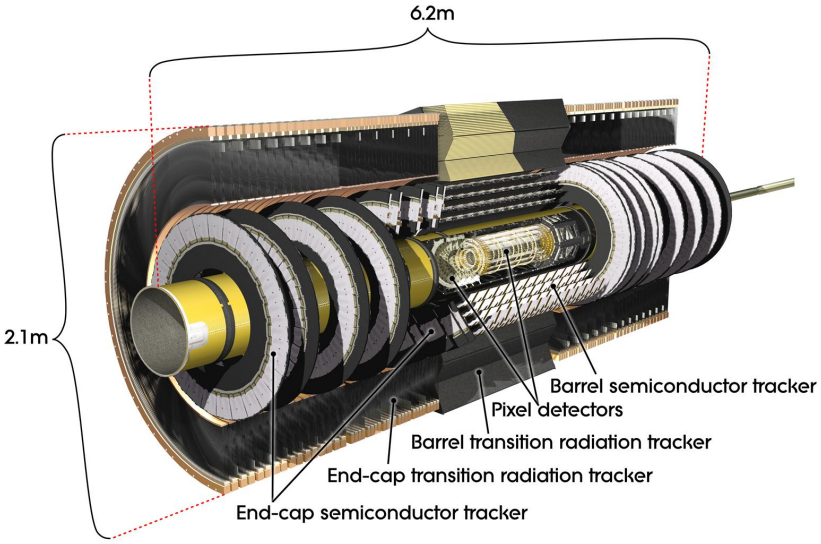

Figure 2.7: Illustration of the ATLAS inner detector system [42].

Pixel detector

The pixel detector [43, 44] is the component closest to the beam pipe and it therefore has to cope with a higher particle flux than any other detector in ATLAS. This requires a high granularity to disentangle tracks from individual charged particles and to identify primary and secondary vertices.

The pixel detector consists of three layers of silicon detectors and is composed of a barrel and an end-cap region. In the barrel region, the layers are situated at radial distances of 50.5, 88.5 and 122.5 mm, while in the end-cap region they are situated at longitudinal distances of 49.5, 58.0 and 65.0 mm from the interaction point. A single silicon pixel of dimension $400 \times 50\ \mu\text{m}^2$ presents a 10 μm resolution in the $R - \phi$ direction and of 115 μm in the z direction. The whole systems contains 1744 sensors with 46080 read-out pixels

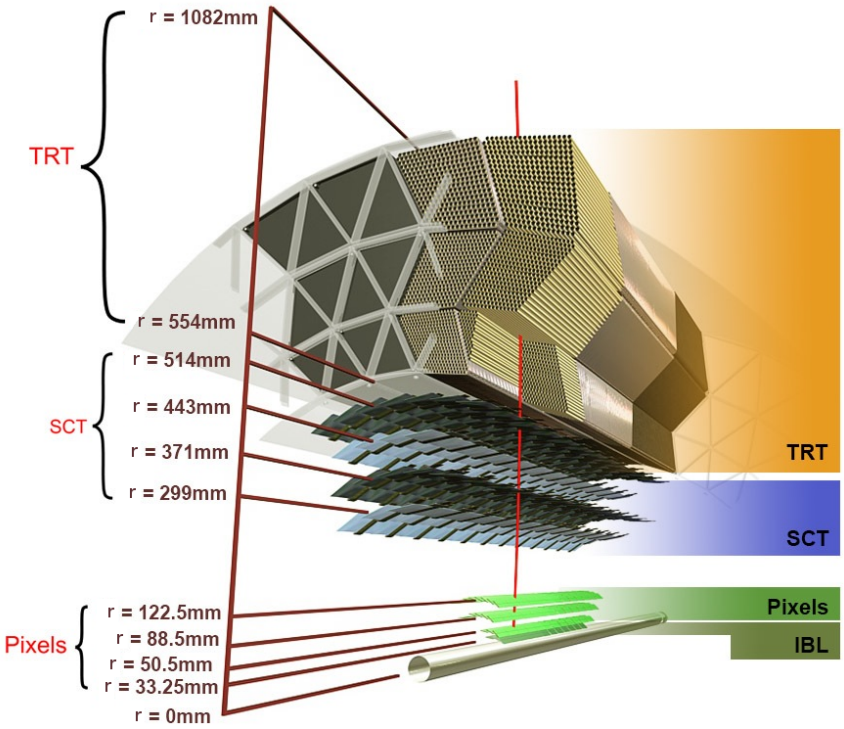

Figure 2.8: Cut-away view of the ATLAS inner detector layers. The figure shows all its components and their relative distances from the interaction point [42].

each, for a total of 80 millions read-out channels. During the 2013-2015 shut-down the pixel detector was extended with a fourth layer, the Instertable B-Layer (IBL), installed at a radius of 33.3 mm. This additional layer improved significantly the inner detector performance recorded in Run-I, enhancing the vertex reconstruction and secondary vertex identification. These features significantly improved the capability of identifying jets coming from b-hadrons. Moreover, it ensured a full ϕ coverage for tracks with an high transverse momentum.

Semiconductor tracker

The semiconductor tracker [45] is designed to provide a high precision measurement of the impact parameter and transverse momentum in the intermediate radial range of the inner detector. The SCT includes four cylindrical layers of silicon microstrip modules placed axially with respect to the beam pipe at radial distances of 300, 373, 447 and 520 mm, and nine disks on each end-cap regions to cover the pseudo-rapidity range of $1.4 < |\eta| < 2.5$ and up to radii of 560 mm. Each of these modules contains 768 readout strips with a 80 μm pitch, arranged in two layers in a stereo configuration, for a total dimension of 6.36×6.40 cm^2. The spatial resolution achieved by the semiconductor tracker is 17 μm in $R - \phi$ and 580 μm in the z direction, and the whole system has a total of 6.3 million readout channels.

Transition radiation tracker

The transition radiation tracker [46] is the outermost part of the inner detector and it consists of straw detectors with a diameter of 4 mm and a 0.03 mm diameter gold-plated tungsten wire in the centre of each straw tube. The tubes were filled during Run-I with a xenon-based gas mixture (70% Xe, 27% CO2 and 3% O), crucial for the particle identification capabilities of this sub-detector based on transition radiation, which is emitted by charged particles traversing a boundary between two dielectric materials. Unfortunately, significant gas leaks were observed during Run-I and it was not possible to fully repair all of them.

As a consequence, during Run-II, all straws belonging to modules with large gas leaks due to cracks were filled with a gas mixture of 70% Ar, 27% CO_2 and 3% O_2. Argon has a much lower efficiency to absorb the transition radiation photons in this energy range, but has similar tracking capabilities as xenon [47]. During Run-III, the majority of the TRT straws are expected to be filled with the argon-mixture gas.

A potential difference of 1.5 kV is applied to the central wire and the surface of the tube, producing an electric current via gas ionisation induced by the transition radiation photons. This current is detectable as a count in the readout system. A significant discrimination power is achieved between electrons and charged pions with energy in the range 1 GeV $\leq$ E $\leq$ 100 GeV. The TRT radial extension goes from 56 to 107 cm, providing a measurement only in the $R-\phi$ ($z-\phi$ in the end-cap) coordinate with a resolution of 130 μm.

The overall inner detector system resolution for charged particles' momentum measurements is:

$$\frac{\sigma(p_T)}{p_T} = 0.05\% \cdot p_T[\text{GeV}] \oplus 1\%; \tag{2.5.1}$$

where the first term represents the intrinsic resolution and the second term the multiple scattering, which is more relevant for particles with low transverse momentum.

2.6 Calorimetry

The calorimeters in the ATLAS detector are designed to absorb and accurately measure the energy of incident particles. The calorimeter system (see Figure 2.9) can be separated into the Electromagnetic calorimeter (ECAL) and the Hadronic calorimeter (HCAL), which are both sampling calorimeters. The ECAL is designed to measure the energies of incident electrons and photons, while the HCAL is designed for measuring the energy of hadrons which interact strongly.

The ATLAS calorimeter systems consists of alternating layers of absorber material and active detector material. When a particle enters the absorber material of a calorimeter, a cascade of particle decays is initiated, known as a shower. Particles interacting via the electromagnetic force produce electromagnetic showers, in which photons subsequently

pair-produce electrons and positrons, both of which undergo Bremsstrahlung radiation of photons.

Particles interacting via the strong force produce much more complex showers. Particle-nucleus interactions in the calorimeters can produce additional hadrons, such as pions. Charged hadrons will lose energy when traversing the absorber material through ionisation processes. In addition, neutral pions in their decay to two photons, $\pi^0 \rightarrow \gamma\gamma$, can induce an electromagnetic shower component.

The radiation length, X_0, of a material is the mean length over which an electron will lose all but $1/e$ of its initial energy through radiative processes, while the interaction length of a material, λ, characterises the mean distance a hadron will travel through a material before undergoing a nuclear interaction. The depth of each calorimeter is optimised to fully contain their respective shower type, hence minimising punch-through into the next detector layer.

The calorimeter system provides coverage in the pseudo-rapidity range $|\eta| < 4.9$ and a full coverage in ϕ, which is needed for precise reconstruction of missing transverse momentum (E_T^{miss}), a key component of many ATLAS searches. The E_T^{miss} is defined as the momentum imbalance in the plane transverse to the beam axis, i.e the resultant of the negative vectorial sum of the momenta of all the particles, based on the conservation of momentum in the plane transverse to the beam axis z, and can be produced for instance by particles that escape the detector undetected such as neutrinos.

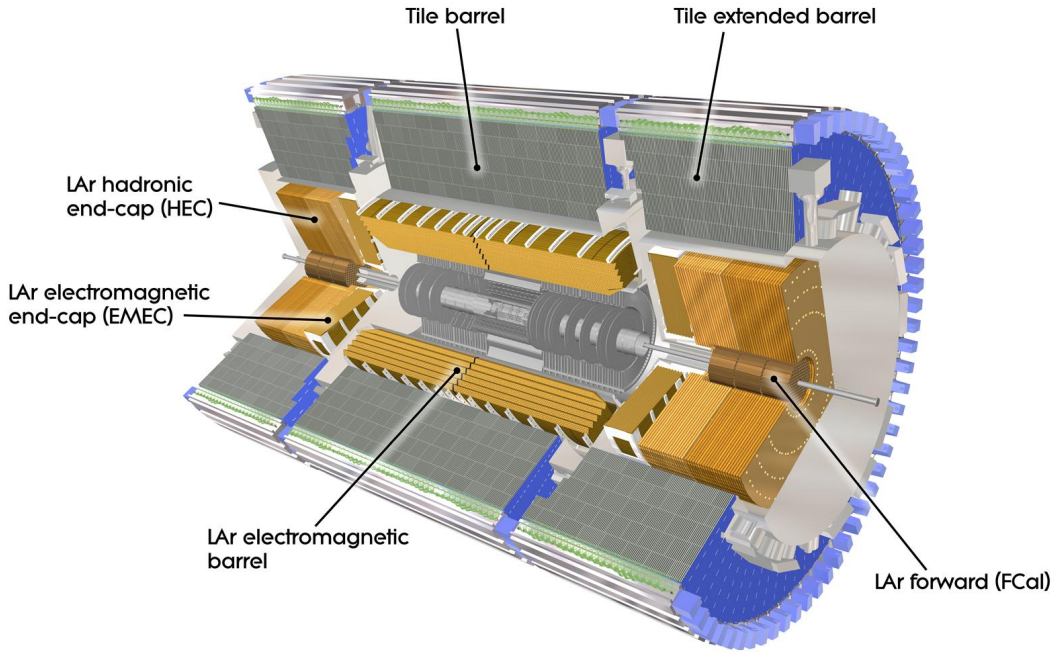

Figure 2.9: Cut-away view of the ATLAS calorimeter system [48].

Electromagnetic calorimeter

In the ATLAS electromagnetic calorimeter [49], lead is used as the passive material and Liquid Argon (LAr) as the active one. This choice of materials has shown a great radiation hardness, preserving high performance for the whole data-taking. The material layers are folded in an accordion geometry, as shown in Figure 2.10, to maximise particle interactions with the different layers and to avoid the presence of possible dead zones.

The total thickness of the ECAL ranges from 22 to 38 (X_0) radiation lengths depending on the η region taken in consideration; this enables to fully contain electromagnetic showers.

To provide a high granularity, the ECAL is segmented into three longitudinal sections and an additional pre-shower (pre-sampler) section with narrow cells.

The ECAL barrel starts at a radius of 1.41 m and ends at 1.96 m with a z extension of $\pm$ 3.21 m, covering the $|\eta| \leq 1.47$ interval. In the $1.37 \leq |\eta| \leq 3.2$ region, the ECAL end-cap starts at $z = \pm 3.70$ m and ends at $z = \pm 4.25$ m. In the region $|\eta| < 1.8$, an additional finely segmented calorimeter layer of LAr and lead is located in the innermost position close to the beam-pipe. The transition region between barrel and end-cap, in the pseudorapidity range $1.37 \leq |\eta| \leq 1.52$, contains a large amount of inactive material providing necessary services to the inner detector. Significant energy loss is recorded in this region, resulting in a low precision measurement, which is often removed in analyses selection.

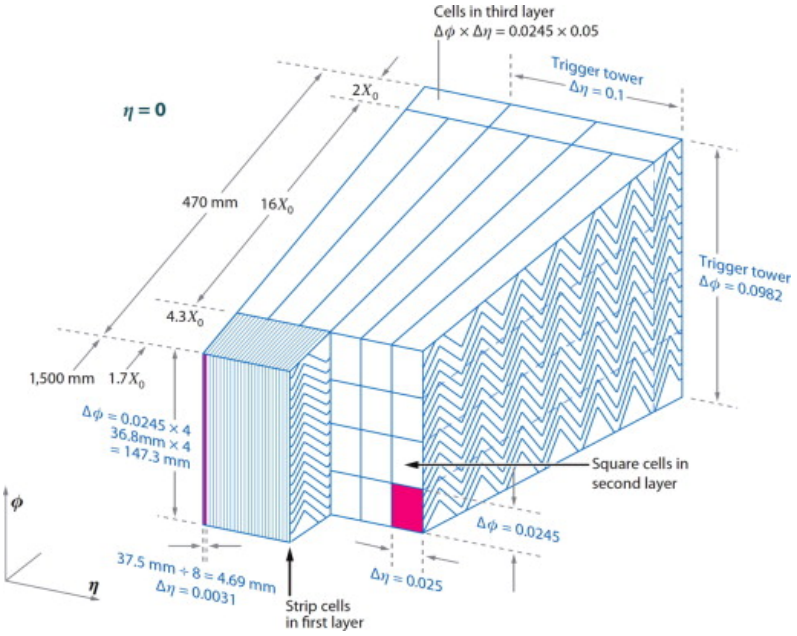

Figure 2.10: Sketch of an electromagnetic calorimeter module where the different layers are clearly visible. The granularity in η and ϕ of the cells of each of the three layers is shown [50].

The whole system is placed inside three independent cryostats to maintain the very

low temperature of 89 K, needed for the correct functioning of the system. The energy resolution of the ECAL is:

$$\frac{\Delta(E)}{E} = \frac{10\%}{\sqrt{E}} \oplus 0.7\%, \tag{2.6.1}$$

where E is expressed in GeV. The first term of the formula is stochastic and related to the calorimeter sampling, while the second one is a constant term related to the non-uniformity of the response of the detector.

Hadronic calorimeter

The hadronic calorimeter is designed to measure the energy deposits and direction of hadronic showers produced by strongly interacting particles. The system provides significant containment of hadronic showers in order to prevent leakages to end up in the muon spectrometer. Furthermore, this guarantees a good missing transverse momentum measurement.

The total amount of material at the end of the active calorimetry region varies between 10 and 18 nuclear interaction lengths (λ).

The HCAL barrels surround the ECAL starting at a radius of 2.28 m and end at 4.25 m with a z extension of $\pm$ 4.10 m, covering the $|\eta| \leq 1.0$ interval. In the end-cap regions, $|\eta| \leq 4.9$, the HCAL starts at $z = \pm 4.3$ m and ends at $z = \pm 6.05$ m. Different sampling techniques are chosen depending on the high radiation environment. The HCAL is divided three sub-detectors: the Tile Calorimeter (TileCal), the Hadronic End-cap Calorimeters (HEC) and the Forward Calorimeter (FCal), which are briefly described in the following.

Tile calorimeter

The hadronic tile calorimeter [51] is located in the barrel covering the $|\eta| \leq 1.0$ region , and has two extensions in the $0.8 \leq |\eta| \leq 1.7$ regions. Steel is used as passive material and scintillating tiles as active material, which produce a signal proportional to the number of secondary particles produced in the interaction. The detector has an energy resolution of:

$$\frac{\Delta(E)}{E} = \frac{50\%}{\sqrt{E}} \oplus 3\%, \tag{2.6.2}$$

where E is expressed in GeV. The first term of the formula is related to the stochastic nature of the development of hadronic showers and the second is a constant term accounting for noise from read-out electronics and other effects.

Hadronic end-cap calorimeter

The Hadronic End-Cap Calorimeter [52] is composed of two independent wheels of radius 2.03 m and covers the range $1.5 \leq |\eta| \leq 3.2$. It uses LAr as active medium and copper

plates as absorbers, as the amount of radiation in the end-caps is greater than in the barrel. The HEC has an energy resolution of:

$$\frac{\Delta(E)}{E} = \frac{50\%}{\sqrt{E}} \oplus 3\%, \tag{2.6.3}$$

where E is expressed in GeV.

Forward calorimeter

The Forward Calorimeter [53] is placed in the high-η region very close to the beam pipe where the particle density is extremely high, covering the region $3.1 \leq |\eta| \leq 4.9$. It is composed of three layers using LAr as active material and copper, for the innermost layer, and tungsten, for the external layers, as abosrbers. The FCAL has a resolution of:

$$\frac{\Delta(E)}{E} = \frac{100\%}{\sqrt{E}} \oplus 10\%, \tag{2.6.4}$$

where E is expressed in GeV.

2.7 Muon spectrometer

The ATLAS muon spectrometer [54] is located in the outermost part of the ATLAS detector and is designed to detect muons, and possibly other charged particles, escaping the calorimeter systems and measure their momentum in a pseudorapidity range $|\eta| < 2.7$, providing also triggering capabilities within $|\eta| < 2.4$.

The MS is composed of very fast momentum measurement chambers and high precision tracking chambers immersed in a toroidal magnetic field, which allows an independent muon transverse momentum measurement.

In the barrel region, $|\eta| \leq 1.05$, three cylindrical layers are situated around the beam axis at radial distances of $\approx$ 5 m (barrel inner, BI), $\approx$ 7.5 m (barrel middle, BM) and $\approx$ 10 m (barrel outer, BO). In the two end-cap regions, $1.05 \leq |\eta| \leq 2.7$, three muon wheels are placed perpendicular to the z-axis at longitudinal distances from the IP of 7.5, 13 and 22 m. The layout of the stations and muon chambers are presented in Figures 2.11 and 2.12.

The overall momentum resolution provided by the muon system is $\sigma(p_T)/p_T \sim$ 2-3%, at 50 GeV, and decreases to $\sigma(p_T)/p_T \sim 10\%$ for a 1 TeV muon.

Muon spectrometer trigger chambers

The barrel region muon trigger system relies on Resistive Plate Chambers (RPC). The RPC is a gaseous detector consisting of two bakelite plates separated by a 2 mm gap filled with a gas mixture of 97% tetrafluoroethane ($C_2H_2F_4$) and 3% isobutane (C_4H_{10}). A high

electric field of 4.5 kV/mm is maintained between the two plates to amplify the primary ionisation of charged particles crossing the detector. The charged induced on metallic strips in the outer sides of the bakelite plates is collected as signal. Two RPC units are placed in each layer orthogonal to one another, providing information on both η and ϕ coordinates. Two layers are installed in the middle station, for the low$-p_T$ trigger, and a third layer is installed in the outer station, for the high$-p_T$ trigger. In the end-cap region, muons are triggered by very thin multi-wire chambers (TGC), designed to have the anode-cathode spacing smaller than the anode-anode spacing for a very short drift time of 20 ns. The chambers are filled with a highly quenching gas mixture of 55% CO2 and 45% n-pentane (n-C_5H_{12}) operating in saturation mode. Both RPC and TGC are also used to improve the measurement along the second coordinate in the non-bending plane ϕ.

Muon spectrometer high precision chambers

The Monitored Drift Tubes (MDT) chambers are used for high precision track measurement in the barrel region and in the end-caps up to $|\eta| \leq 2$. Each side of the chambers is composed of two multi-layers of aluminium drift tubes, with diameter of 30 mm and thickness of 400 μm, filled with a gas mixture of Ar and CO_2 at a pressure of 3 bar. The drift time in each tube is measured by a Tungsten-Rhenium wire placed in the centre, yielding a resolution of 80 μm. The total chamber resolution is 35 μm. In the high occupancy forward region $2 \leq |\eta| \leq 2.7$, where rates greater than 150 Hz/cm^2 are found, the more robust multi-wire strip cathodes chambers (CSC) are adopted. CSC cathodes are segmented in orthogonal strip wires to allow a measurement in both coordinates with a resolution of 60 μm in R and 5 mm in the ϕ direction. These chambers present also a good time resolution of about 7 ns.

2.8 Trigger System

The ATLAS trigger and data acquisition (TDAQ) system [55] has the pivotal task of performing an online event selection while having to cope with the impressive 40 MHz event rate of the Run-II LHC system. A typical ATLAS event occupies a few MB of disk space, hence due to limitation in data storage, computing and transfer rates, it is not realistic to read out and store all LHC events. In addition, most of the data are not of interest for the ATLAS physics program, as the rate is dominated by low-p_T inelastic and diffractive collisions. Therefore, a balance between the data acquisition rates and high efficiency for selecting interesting physics data has to be found, keeping in mind that an event which is not triggered is lost forever.

The ATLAS Run-II TDAQ system is built on two levels of online selection, as shown in Figure 2.13: a first hardware based level-1 (L1), that significantly reduces the initial event rate, and a second software based level (HLT), where the final decision is made.

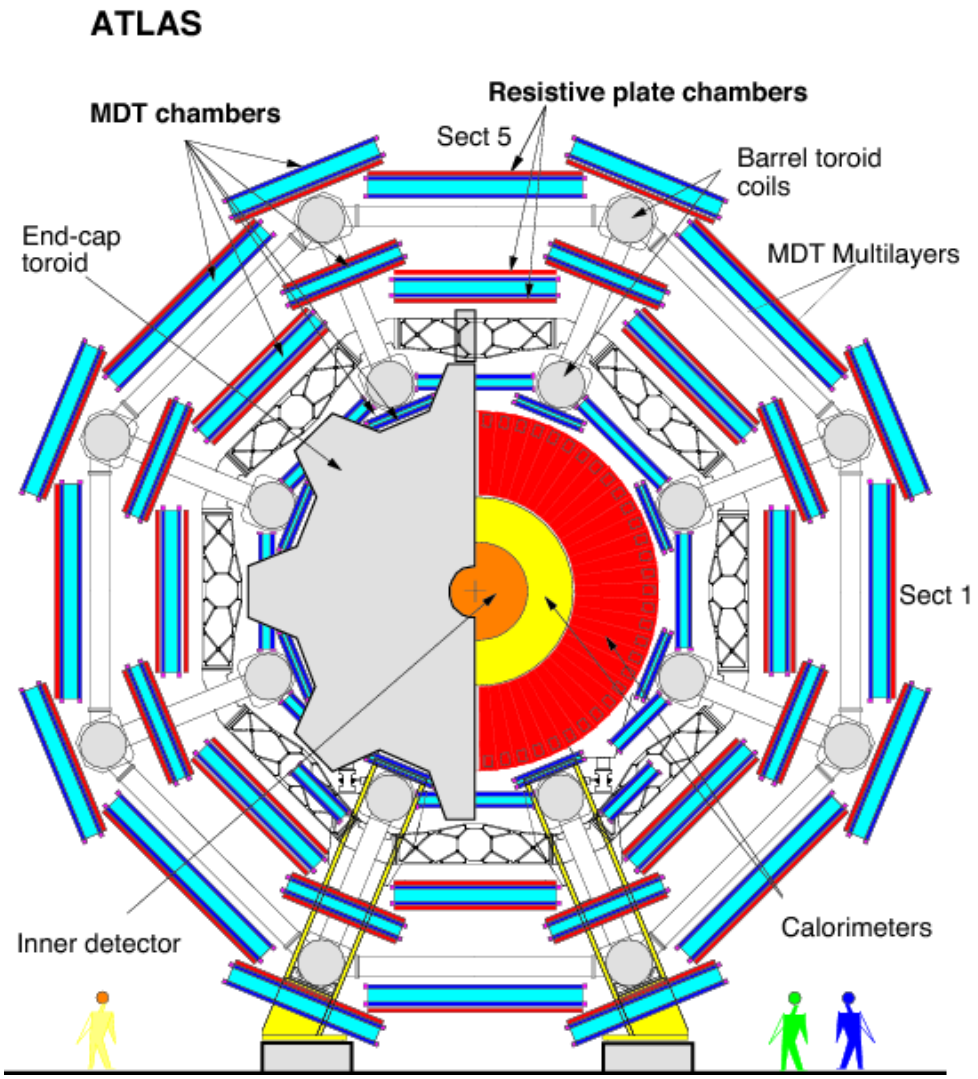

Figure 2.11: Schematic view of the transversal projection of the muon spectrometer [54].

Level-1 trigger

The hardware L1 exploits quickly accessible coarse data from the calorimeters and the muon spectrometer in dedicated regions of interest (RoI). Calorimeters provide information about clusters of energy deposits, missing transverse energy and raw shape dimensions, while the muon spectrometer provides information from trigger chambers about transverse momentum and track position. Making use of those informations, a decision is made in less than 2.5 μs. At L1, the initial event rate of 40 MHz is reduced to 100 kHz.

High level trigger

The software level integrates the data from the regions of interest with the full detector information and runs complex trigger algorithms to select the events. A fast reconstruction step is firstly used for the trigger selection, followed by a more precise refinement similar

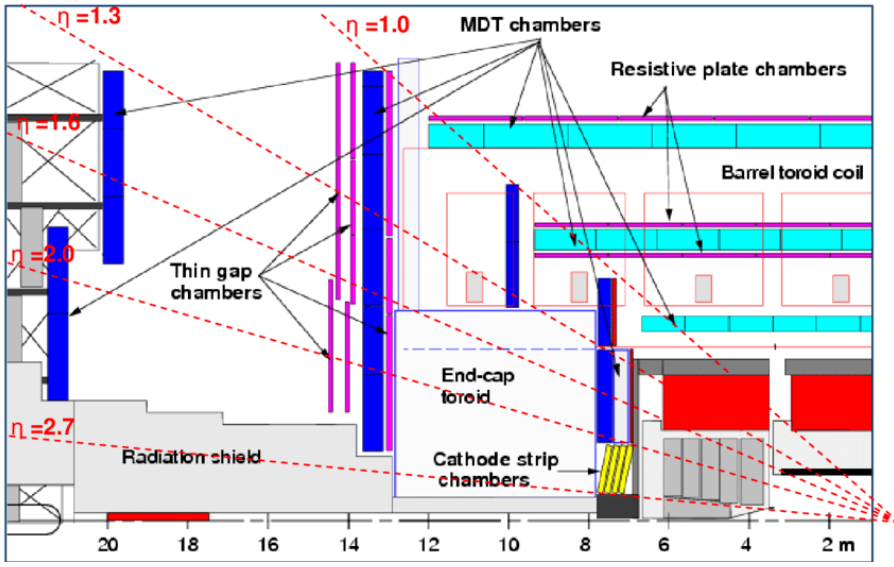

Figure 2.12: Schematic view of the longitudinal projection of the muon spectrometer [54].

to the offline reconstruction. The HLT is the first step in which inner detector information is incorporated in the trigger, where only track information inside identified RoI at L1 are used due processing time constraint. The muon fast reconstruction integrates each L1 muon candidate with MDT data preforming a track fit extrapolated to the inner detector. The ID fast tracking consists in trigger specific pattern algorithms, designed to identify compatible track segments and hit points. Raw calorimetric informations are reconstructed by fast algorithms into cluster and cell objects, which will later be reconstructed in jet, electron, and photon candidates. The HLT allows to make decisions within 0.2 μs and brings the final event rate to 1 kHz.

Level-1 Muon Trigger

The L1 muon trigger processes information from the muon spectrometer in a dedicated region of interest of dimension 0.4×0.4 in $\Delta\eta \times \Delta\phi$ in the barrel, and 0.2×0.2 in the end-caps, matching coincident hits in space and time. Hits collected from the RPC or TGC trigger chambers are used to build hit patterns. If the pattern is contained inside a fixed window pointing to the impact parameter, whose width defines the p_T threshold, the trigger match is done. A hit pattern of a muon with infinite momentum would result in a straight line, therefore a high-p_T muon would fire also low-p_T triggers, which requires fewer coincidences within a trigger window. Instead, a low-p_T muon would fall outside a high-p_T trigger window. Figure 2.14 show a schematic picture of the low-p_T and high-p_T triggers in ATLAS.

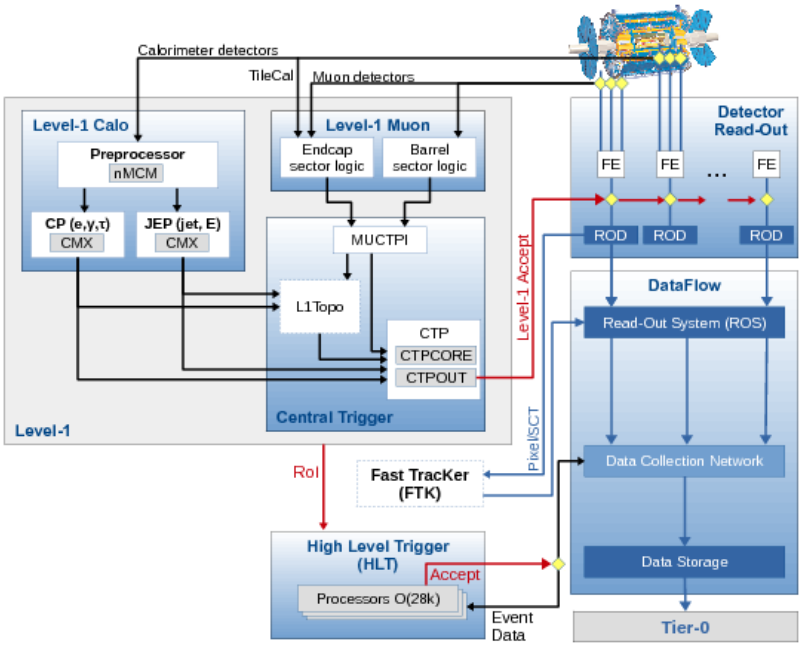

Figure 2.13: Schematic view of ATLAS TDAQ system in Run-II [55].

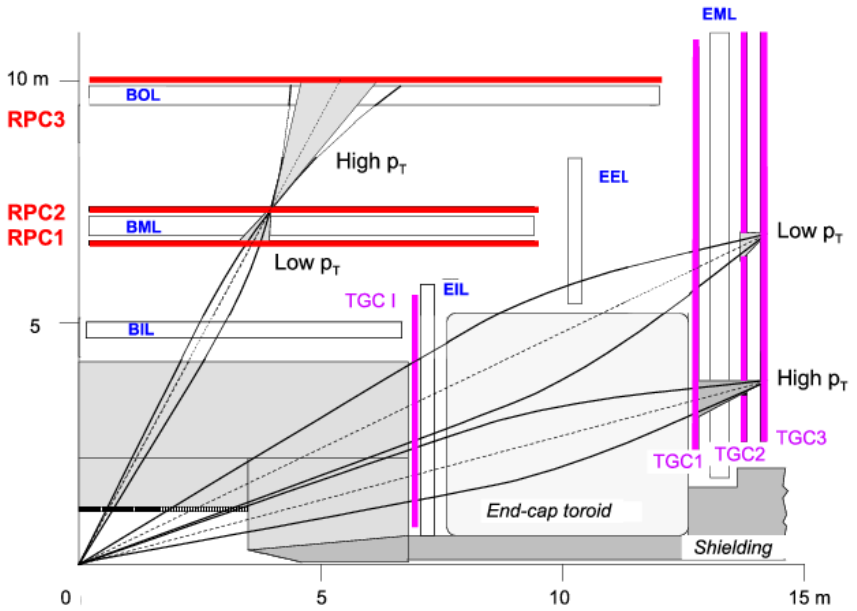

Figure 2.14: Schematic picture showing the L1 muon low-p_T and high-p_T triggers in the ATLAS Muon Spectrometer barrel and end-cap.

Chapter 3

Data and Monte Carlo samples

The aim of this chapter is to discuss the datasets used in the physics analysis later described in Chapters 5 and 6, detailing the running conditions during data-taking and the triggers used to collect the data. In addition, the procedure through which Monte Carlo (MC) samples are generated is discussed, along with a brief discussion of the generators used.

3.1 Datasets

The physics analysis described in Chapters 5 and 6 used data collected by the ATLAS detector during Run-II of the LHC (2015-2018) in pp collisions at $\sqrt{s} = 13$ TeV. In this period a peak instantaneous luminosity of 2.1×10^{34} cm^{-2}s^{-1} was reached, resulting in a mean number of interactions per bunch crossing $\langle\mu\rangle$ of 34 (see Section 2.2). Data quality requirements [56] are applied to ensure that all sub-detectors were operating normally and that the LHC beams were in stable-collision mode. The integrated luminosity of the resulting data sample is 139 fb^{-1} with a 1.7 % uncertainty [57]. The primary measurement of the luminosity is recorded by the LUCID-2 detector [58], which sits 17 m from the interaction point on both ATLAS end-caps and measures the visible number of interactions per bunch-crossing. Each pp collision which produces at least two tracks with $p_T > 0.4$ GeV is classified as an interaction point, being referred to as a collision vertex. The collision vertex in each bunch-crossing which has the highest Σp_T^2 of tracks is identified as the Primary Vertex (PV), while all other vertices are considered pile-up vertices.

The dataset used in the analysis was collected either using a set of triggers specifically designed to target displaced decays, or single-lepton triggers, with requirements on the identification, isolation and transverse momentum of the leptons to maintain high efficiency across the full momentum range, while keeping under control the relative trigger rates. Those triggers are described in detail in Section 3.2.

In addition to the main dataset, also referred to as collision dataset, additional datasets targeting the so-called non-collision backgrounds are collected. Studies on these supplementary datasets are needed since particles generated in those processes can mimic the

long-lived particle signatures of interest for the analysis presented in this thesis.

3.1.1 Cosmic and Beam induced background datasets

During *pp* collisions data-taking, the LHC circulates two counter-rotating proton beams constructed from bunches of protons. However, following LHC injection, not all bunch slots are filled with protons, with the number of unfilled bunches depending on the accelerator filling scheme [19]. Bunch crossing where one or both beams are not filled with protons are ideal for studies on non-collision backgrounds. This term refers to signals seen in the ATLAS detector which have not been produced in standard collisions of the LHC beams, and the main components are beam-induced backgrounds (BIB) and cosmic-ray showers.

A cosmic-ray background enriched dataset is collected during empty bunch crossings (cosmic dataset) and used for the estimation of this background. An empty bunch crossing takes place when neither beam is filled with protons and each empty bunch is separated from filled bunches by at least five empty bunches on each side.

Beam-induced background arises from the unavoidable LHC proton beams losses [59], which interacts with either residual gas in the beam pipe (beam-gas scattering) or with machine elements such as collimators. In both cases, the resulting particles are almost parallel to the beam line (z-axis) and have a large Lorentz boost. Even though BIB in ATLAS is mitigated by the presence of a dedicated shielding placed around the beam pipe, there is still a fraction of these particles that can reach the detector and be a potential background for physics analyses. Due to the peculiar nature of these events, the possible contribution for this background can only be estimated through the aid of a dedicated data sample. For this reason, a BIB [59] enriched dataset is collected during unpaired isolated bunch crossings (BIB dataset) and, by using a different trigger, on colliding bunch crossings (collision BIB dataset). In unpaired bunch crossings, only one of the two beams is filled with protons and is separated from filled bunches by at least three unfilled ones on each side. This dataset is used to identify characteristic features of BIB and to estimate possible residual contamination in the collision dataset. The same triggers adopted to select the dataset used in the analysis (see Section 3.2) were operating during the Run-II data-taking in both the empty and unpaired bunch crossings. The ratio of the number of filled to empty bunch crossings, F_{CR}, is used to scale the number of events in the cosmic dataset to that in the *pp* collision data. It is computed with the following formula:

$$F_{\mathrm{CR}} = \frac{\sum \mathrm{Time}_{\mathrm{paired}}}{\sum \mathrm{Time}_{\mathrm{empty}}}$$
$$\mathrm{N}^{\mathrm{exp.paired}} = F_{\mathrm{CR}} \times \mathrm{N}^{\mathrm{obs.,empty}}. \tag{3.1.1}$$

Where $\sum \mathrm{Time}_{\mathrm{paired}}$ and $\sum \mathrm{Time}_{\mathrm{empty}}$ represents respectively the sum of the time dur-

ing the data-taking where bunch crossings are paired or empty. The scale factors obtained are reported in Table 3.1.

	2015-2016 Scale Factor	2017 Scale Factor	2018 Scale Factor
Tri-muon msonly	2.6	3.03	3.92
CalRatio	2.2	2.2	3.06

Table 3.1: Scale factors obtained using equation 3.1.2, for the triggers used in EMPTY bunch crossings. The scale factors are used to scale the number of events in the cosmic dataset to that in the pp collision data. The trigger naming "Tri-muon msonly" implies that the trigger algorithm searches for three muon candidates, reconstructed using only information obtained from the ATLAS Muon Spectrometer. The "CalRatio" trigger name refers to the fact that jet candidates are selected by the trigger algorithm according to the ratio between the amount of energy released by the jet in the hadronic calorimeter and in the electromagnetic calorimeter.

Finally, cosmic and beam-induced background datasets are subject to the same data quality requirements that are applied to the collision dataset.

3.2 Triggers for event selection

A large fraction of the standard ATLAS triggers [60] are designed and optimised for prompt objects and, therefore, show several limitations in selecting the products of displaced and collimated decays.

For this reason, in the case of gluon-gluon fusion Higgs boson production, dedicated triggers have been used, which are developed to specifically select displaced objects. In the case of Higgs boson associated production with a W boson, single lepton triggers are used, exploiting the presence of a high-p_T charged lepton coming from the W decay. All the triggers used in this analysis are unprescaled during the relative data-taking periods. The triggers used for the ggF process are listed in Sections 3.2.1, 3.2.2 and 3.2.3, while the ones applied to the WH process are listed in Section 3.2.4.

3.2.1 Narrow-Scan trigger

The Narrow-Scan trigger was introduced since the 2015 data-taking and adopts a specialised and novel approach for a wide range of signal models featuring highly collimated muons, such as muons coming from dark-photon decays. The Narrow-Scan algorithm begins with requiring an object at L1 which is consistent with a muon (L1 trigger muon object). Other multi-muon triggers, which usually require more L1 trigger muon objects, have large associated signal efficiency losses in the case where the muons are produced close together. These losses are mainly due to the limited granularity at L1, resulting in fewer reconstructed L1 muon objects and, therefore, a lower trigger efficiency due to the inevitable matching

ambiguity between the L1 and the HLT muon objects. To compensate for the high rate from only one L1 muon object (which is fully matched at HLT), a "scan" is performed for another muon at HLT without requiring it to match a L1 muon object. To limit the online resources consumption, the scan is limited to a narrow cone around the previously fully matched muon, where other muons coming from dark-photon decays are expected to be found. In the trigger used in this analysis, neither of the fully matched HLT muons is required explicitly to have a matching ID track. Additionally, only in the 2016 version of this trigger, the "scanned" muon is explicitly required to be unmatched to an ID track.

In this analysis the trigger is implemented such that the fully matched muon must have $p_{\mathrm{T}} \geq 20$ GeV, while the "scanned" muon must lie in a cone of $\Delta R = 0.5$ around the leading muon and have p_{T} with increasing values according to the instantaneous luminosity delivered by the LHC in order to stay within the allocated trigger rate limits (see Table 3.2).

Period	Integrated Luminosity	Leading muon threshold	"scanned" muon threshold
2015 - all periods	3.2 fb^{-1}	20 GeV	6 GeV
2016 - period A - F	14.9 fb^{-1}	20 GeV	10 GeV
2016 - period G - END	18.0 fb^{-1}	20 GeV	15 GeV

Table 3.2: p_{T} thresholds of the narrow-scan in the 2015-2016 data-taking periods.

Narrow-Scan + X

The narrow-scan trigger is known to be costly in terms of trigger bandwidth and therefore an alternative is needed for luminosities greater than 10^{34} $\mathrm{cm}^{-2}\mathrm{s}^{-1}$. For the 2017-2018 data-taking periods, alternative narrow-scan triggers with additional L1 topological features are used. An additional isolation requirement at HLT on the leading muon, called *iloosems*, which requires the sum of the p_{T} of the tracks around the muon to be less than 3 GeV, has also been added for the 2017-2018 versions of narrow-scan triggers. This new isolation selection helps to further reduce the otherwise overwhelming trigger rate.

The "narrow-scan + muon" uses the same HLT configuration as the 2015 narrow-scan with the addition of *iloosems* isolation requirement, but at L1 it exploits also topological informations to require the same muon satisfying a $p_{\mathrm{T}} > 20\ GeV$ cut (MU20), but adding a non-matched muon satisfying a $p_{\mathrm{T}} > 6\ GeV$ cut (MU6) with $\Delta R(MU20, MU6) > 1$. The MU6 should not be matched to HLT and is enough to reduce the Narrow-Scan input rate such that, even if the CPU per event is relatively high, the overall consumption is tolerable at the rate it runs. This trigger targets events with two back-to-back dark-photons decaying to muons.

The same idea is used for the "narrow-scan + X" triggers, which requires the same L1 MU20 object with the addition of either a jet or measured missing transverse momentum. These two additional triggers target events with two dark-photon jets decaying into muon

and jets.

Table 3.3 summarises the integrated luminosity collected by narrow-scan + X triggers during the 2017-2018 data-taking.

Period	Trigger	Integrated Luminosity fb^{-1}
2017-2018	HLT_mu6_dRl1_mu20_msonly	102.9
2017-2018	HLT_mu20_msonly_dRl1_L1mu20_J40	102.9
2017-2018	HLT_mu20_msonly_dRl1_L1mu20_XE30	102.9

Table 3.3: Narrow-scan + X triggers in the 2017-2018 data-taking periods. The trigger naming conventions are defined as follows: *HLT* indicates a High Level Trigger, μ indicates a muon and the subsequent number indicates the transverse momentum threshold. *dRl1* indicates that the muon candidates must be reconstructed at the Level 1 trigger within a certain ΔR threshold. *msonly* indicates that only muon spectrometer information is used to reconstruct the muon candidate. Finally, in the second and third row of the table respectively, *J40* indicates a jet, with the subsequent number indicating the transverse momentum threshold, and similarly *XE30* indicates missing transverse momentum and relative threshold required.

Narrow-Scan Trigger Efficiency

The Narrow-Scan trigger efficiency can be computed, for our signal models, as a function of different dark-photon variables such as: measured decay length in x-y plane (L_{xy}) and p_T, as shown in Figures 3.1 and 3.2 for 2015-16 and 2017-18 Narrow-Scan respectively.

To evaluate the efficiencies, dark-photons decaying in $\mu^+\mu^-$ are selected at the truth level for which one of the two muons satisfies $p_{\mathrm{T}} > 20$ GeV and the other $p_{\mathrm{T}} > 6$ GeV. As the Narrow-Scan trigger requires two collimated muons, it is expected that its trigger efficiency drops after a certain decay distance from the PV (e.g. ~ 7.5 m in the barrel region, corresponding to the radial position of the RPC Barrel middle layers). Leftover efficiency at high decay distance ≥ 8 is observed in models with boosted configurations in the 2015-2016 Narrow-Scan trigger (see Figure 3.1), due to decays happening in RPC outer layers. Those are less evident or not present in the 2017-2018 Narrow-Scan trigger plots (see 3.2), due to the different trigger algorithms and requirements involved.

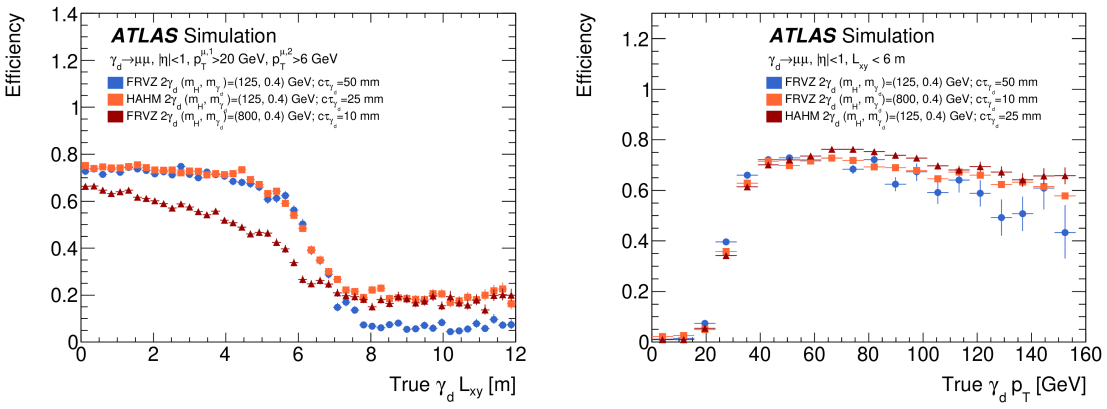

(a) (b)

Figure 3.1: The 2015-16 Narrow-Scan trigger efficiency for events with displaced decays of γ_d in $\mu^+\mu^-$. (a) shows the trigger efficiency for γ_d with $0 < |\eta| < 1.1$ as function of the transverse decay distance L_{xy}. (b) shows the trigger efficiency for γ_d with $0 < |\eta| < 1.1$ as function of the transverse momentum, in events where the γ_d L_{xy} is below 6 m. Uncertainties are statistical only.

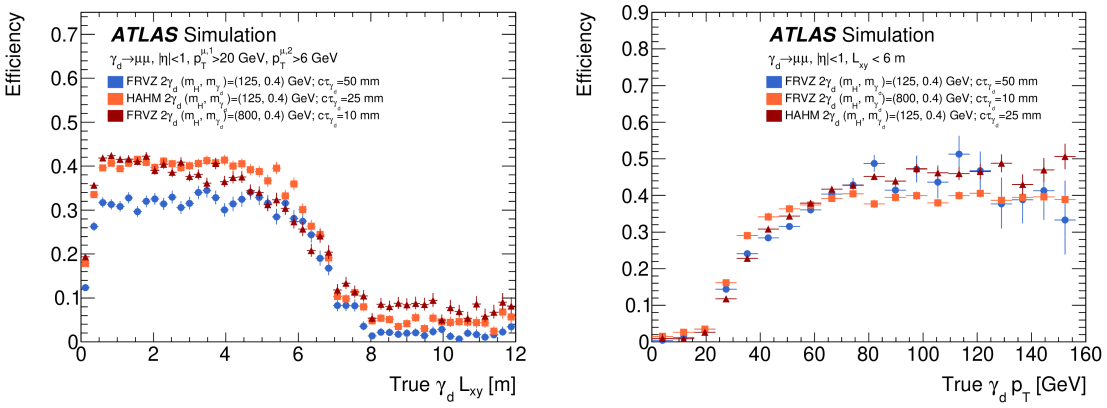

(a) (b)

Figure 3.2: The 2017-18 Narrow-Scan trigger efficiency for events with displaced decays of γ_d in $\mu^+\mu^-$. The efficiency curves shown are the result of the logical or between all the 2017-18 Narrow Scan triggers. (a) shows the trigger efficiency for γ_d with $0 < |\eta| < 1.1$ as function of the transverse decay distance L_{xy}. (b) shows the trigger efficiency for γ_d with $0 < |\eta| < 1.1$ as function of the transverse momentum, in events where the γ_d L_{xy} is below 6 m. Uncertainties are statistical only.

3.2.2 The CalRatio trigger

The CalRatio trigger [61] is designed to identify displaced isolated jets with very low EM fraction. Two types of CalRatio triggers are used, differing only in the `L1` item:

- During 2015 and 2016 runs a L1 tau lepton seed is chosen, motivated by the fact that this L1 item sums energy in a $\eta \times \phi = 0.2 \times 0.2$ region, which may be more suitable for the identification of light LLP decaying in the calorimeter as collimated objects, while a jet trigger sums energy in a wider region (0.8×0.8).

- In 2017 and 2018 runs a different seed is used, which exploits both calorimeter and MS information at L1. In order to fire this trigger, a L1 tau lepton seed requirement must also be met, vetoing the presence of > 3 GeV missing transverse momentum related energy deposits in a $\eta \times \phi = 0.2 \times 0.2$ region around the seed object.

The HLT requires the jet to have $|\eta| \leq 2.4$ to ensure that ID tracks can be matched to it. A selection requirement on the calorimeter energy ratio is then imposed, requiring $\log_{10}(E_{\mathrm{HCAL}}/E_{\mathrm{ECAL}}) \geq 1.2$ (EM fraction < 0.06). Finally, ID track isolation requirements on tracks around the jet axis (no track with $p_{\mathrm{T}} \geq 2\ GeV$ within $\Delta R \leq 0.2$ from the jet axis) are applied. A dedicated procedure to remove mis-identified jets originating from BIB, referred to as BIB removal algorithm, is applied. The BIB removal algorithm relies on cell timing and position; calorimeter hits resulting from BIB will be aligned in a horizontal line parallel to the beam pipe and will have a very specific time distribution. The time and the position of these hits result to be very different from a particle travelling at the speed of light from the IP to the hit location. An inclusive version of the CalRatio trigger is available (identified by the `noiso` string in the HLT chain) , which does not include the BIB removal algorithm and may be used, in combination with a veto on the standard CalRatio trigger to produce a BIB dataset in collision events (collision BIB dataset). The requirement on cell timing imposed by the standard CalRatio trigger is $t_{\mathrm{cell}} > -2\ ns$, thus events in the Collision BIB dataset will only include BIB from the current bunch crossing.

Table 3.4 summarises the integrated luminosity collected by CalRatio triggers during the Run-II data-taking.

The CalRatio trigger is also active during non-standard data-taking periods, such as in empty or unpaired bunch crossings, allowing the production of dedicated BIB and Cosmic enriched datasets.

CalRatio trigger efficiency

In order to evaluate the CalRatio trigger efficiency, the DPJs produced by dark-photon $\rightarrow ee/\ q\bar{q}$ decays in the acceptance region of the ID ($|\eta_{\gamma_d}| < 2.4$) are selected at the truth level.

Chain name	Stream	used in
`HLT_j30_llp_L1TAU60`	Main	2015, Main analysis
`HLT_j30_llp_L1TAU60`	Main	2016, Main analysis
`HLT_j30_llp_L1LLP-NOMATCH`	Main	20172018, Main analysis
`HLT_j30_llp_L1TAU60`	Main	Collision BIB dataset
`HLT_j30_llp_L1TAU30_EMPTY`	Late	`EMPTY` BC
`HLT_j30_llp_L1TAU30_UNPAIRED_ISO`	Late	`UNPAIRED_ISO` BC

Table 3.4: CalRatio triggers in Run-II data-taking periods. The trigger naming convention is defined as follows: *HLT* indicates a High Level Trigger, *j30* indicates a jet and the number indicates the transverse momentum threshold. *llp* indicates that the trigger is suitable for long-lived particles reconstruction. *L1TAU60* indicates that a tau lepton candidate seed is required at the Level 1 trigger, with the number indicating the corresponding transverse momentum thresholds. *L1LLP-NOMATCH* indicates the presence of a Level 1 trigger tau lepton candidate with at least a 30 GeV transverse momentum, with additional requirements on the presence of additional energy deposits in the calorimeters.

CalRatio trigger efficiencies are calculated, respectively, as a function of L_{xy} and of p_{T} for signal events. This is done by requiring, at the truth level, that the γ_d decays in e^+e^- or $q\bar{q}$ in the corresponding η range and with an appropriate decay distance from the interaction point.

Efficiencies for some benchmark signal samples with $m_H = 125\,GeV$ are shown in Figures 3.3 and 3.4 for the 2015-16 and 2017-18 CalRatio triggers, respectively. As clearly visible from the aforementioned figures, the trigger is efficient when most of the γ_d decay close to the transition between the ECAL and the HCAL, while its efficiency drops when approaching the outermost region of the HCAL. Moreover, it is possible to notice that the efficiency for the signal model involving the presence of a 800 GeV Higgs-like scalar is much higher with respect to the other cases, as expected due to its heavily boosted configuration.

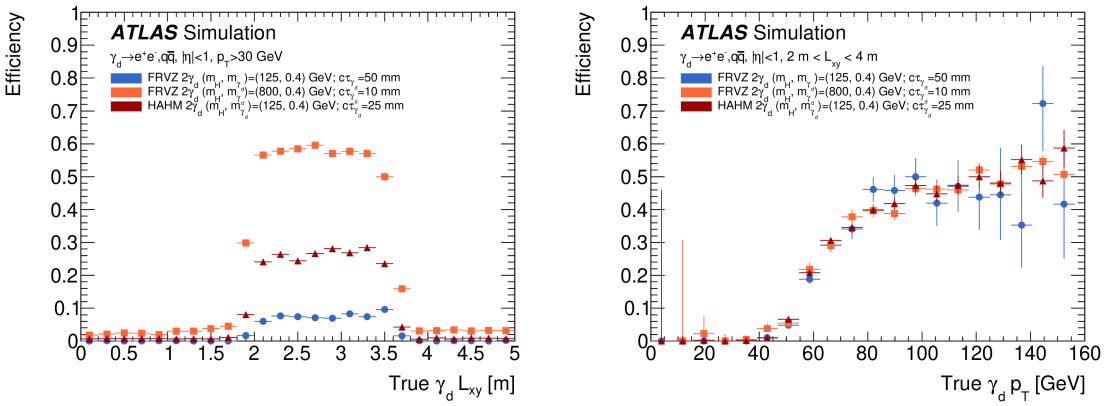

(a) (b)

Figure 3.3: The 2015-2016 CalRatio trigger efficiency for events with displaced decays of γ_d in e^+e^- or $q\bar{q}$. (a) shows the trigger efficiency for γ_d with $0 < |\eta| < 1.1$ as function of the transverse decay distance L_{xy}. (b) shows the trigger efficiency for γ_d with $0 < |\eta| < 1.1$ as function of the transverse momentum in events where the γ_d L_{xy} is between 2 m and 4 m.

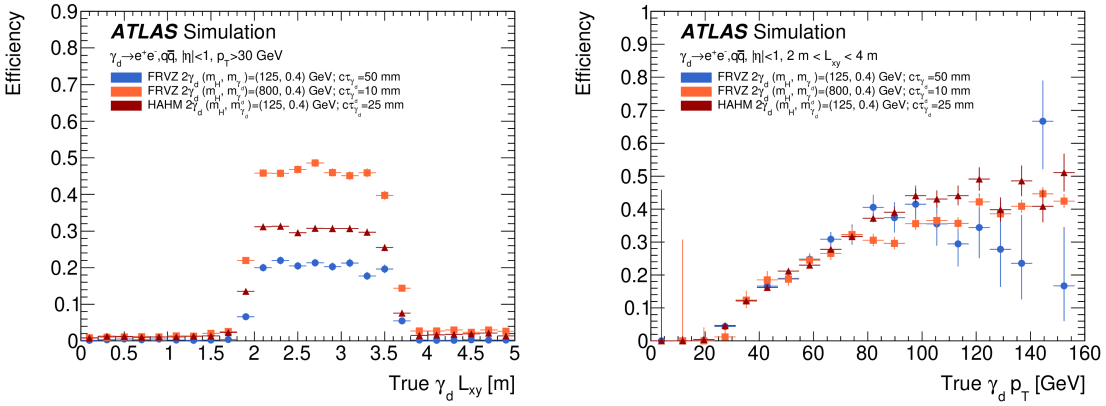

(a) (b)

Figure 3.4: The 2017-18 CalRatio trigger efficiency for events with displaced decays of γ_d in e^+e^- or $q\bar{q}$. (a) shows the trigger efficiency for γ_d with $0 < |\eta| < 1.1$ as function of the transverse decay distance L_{xy}. (b) shows the trigger efficiency for γ_d with $0 < |\eta| < 1.1$ as function of the transverse momentum in events where the γ_d L_{xy} is between 2 m and 4 m.

3.2.3 Tri-muon MS-only

The tri-muon MS-only [61] trigger selects events with at least three L1 muons with $p_{\mathrm{T}} \geq 6$ GeV, confirmed at HLT using only the MS information. It is expected to be very effective in selecting events for the $pp \to H \to 4\gamma_{\mathrm{d}} + X$ process for dark-photons decaying into muons. It is less effective in selecting events for the $pp \to H \to 2\gamma_{\mathrm{d}} + X$ where two close-by muons coming from the same dark-photon need to fall in two separate RoI.

Period	Trigger	Integrated Luminosity
2015 - all periods	HLT_3mu6_msonly	3.2 fb^{-1}
2016 - all periods	HLT_3mu6_msonly	32.9 fb^{-1}
2017 - all periods	HLT_3mu6_msonly	44.3 fb^{-1}
2018 - all periods	HLT_3mu6_msonly	58.5 fb^{-1}

Table 3.5: Tri-muon MS-only trigger in the 2015-2018 data-taking periods. The trigger naming conventions are defined as follows: *HLT* indicates a High Level Trigger, 3μ indicates the request for the presence of three muon candidates, and the subsequent number indicates the transverse momentum threshold. *msonly* indicates that only muon spectrometer information is used to reconstruct the muon candidate.

3.2.4 Single lepton triggers

The events in the WH analysis are triggered with single lepton triggers, with the lepton being either an electron or a muon. The trigger menu used is reported in Table 3.6. Due to the sharp turn-on curve of single lepton trigger efficiencies, a $p_T > 27$ GeV is required for the leading lepton, which has been proved to keep a high signal efficiency in 2015-2018 data-taking.

Period	Trigger	Integrated Luminosity
2015 - all periods	HLT_e24	3.2 fb^{-1}
2015 - all periods	HLT_mu20	32.9 fb^{-1}
2016-18 - all periods	HLT_e26	44.3 fb^{-1}
2016-18 - all periods	HLT_mu26	58.5 fb^{-1}

Table 3.6: Lowest unprescaled single lepton triggers in the 2015-2018 data-taking periods. The trigger naming conventions are defined as follows: *HLT* indicates a High Level Trigger, e or μ indicates the request for the presence a muon, or electron, candidate and the subsequent number indicates the transverse momentum threshold.

3.3 Simulated samples

Simulated samples are used for the analysis optimisation and for the evaluation of the final contribution of the signal processes of interest to this search. They are also needed to better

understand the detector performance, to estimate the systematic uncertainties and are also helpful during the background estimation process.

3.3.1 Event simulation

Each high energy pp collision at the LHC produces hundreds of particles with momentum range spread over many orders of magnitude. Using the factorisation theorem, the description of such interactions can be divided in two terms, depending on the amount of transferred momentum involved.

At energy scales $\gg$ 1 GeV, the hard scattering between the constituents of the protons can be perturbatively computed in terms of the matrix element (ME) of the process. At energies of the order of 1 GeV or lower, many other physics processes of non-perturbative nature arise, leading to the use of simulation models depending on tunable parameters that describe the data. The energy scale around 1 GeV that separates the two terms is known as the factorisation scale, μ_F, and is introduced to remove low energy divergences from the cross-section calculations.

The simulation of an high energy pp collision relies on a variety of programs, based on Monte Carlo methods, which are able to describe the different phases of the proton-proton scattering.

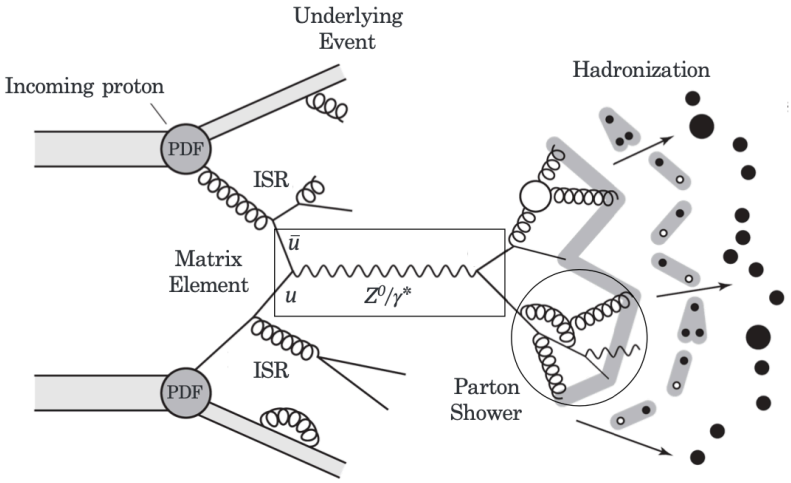

Figure 3.5: A schematic representation of a proton-proton collision as simulated by the event generator. Two partons from the colliding protons, described by the parton density functions, undergo a hard interaction (Matrix Element). Additional hard QCD radiation is produced (Parton Shower), before the final state partons start hadronising (Hadronisation). Additional activity in the event originates from the underlying event [62].

As shown in Figure 3.5, the simulation of a $pp \rightarrow X$ interaction can be divided in different steps: the hard scattering, the parton shower, the hadronisation, the underlying event, and the decay of unstable particles in the final state. The results depend on the distribution of quarks and gluons carrying a fraction of the total momentum of the protons,

the parton density functions (PDFs). Those, as well as the various steps present in MC event generations, are described in the following.

Parton Density Functions

PDFs are obtained from a global fit to the input datasets from Deep Inelastic Scattering (DIS), fixed-target Drell-Yann, and collider experiments, and are extrapolated over a wide range of energies.

Several PDF sets are available (e.g CT [63], NNPDF [64]), making use of different input datasets, value of the factorisation scale, and order of the perturbation theory at which they are calculated.

Matrix Element

The ME represents, as stated above, the hard scattering part of the process and is calculated evaluating the Feynman diagrams representing the process of interest. MEs can be calculated at different orders on QCD. If the calculation is performed at the lowest order, is said to be at Leading-Order (LO) and represents the tree-level process. When moving up considering higher orders we will refer to calculation as Next-To-Leading-Order (NLO), Next-To-Next-To-Leading-Order (NNLO) etc.

In the case of NLO or NNLO simulations, many diagrams describing virtual loops are added to the computation, making the simulation very slow.

Most of the current event simulation in use at LHC employ LO or NLO matrix elements. In order to take into account higher order corrections, the so-called k-factors are used to reweight the LO (NLO) cross-section and they are obtained by the ratio of the total NLO (NNLO) cross-section calculated analytically to the LO (NLO) one from the MC generator.

Parton Shower (PS)

The partons involved in the hard scattering can radiate gluons which can, in turn, split into quark-antiquark pairs or gluons generating a shower of outgoing particles. The parton shower algorithms are used to evolve the hard scatter from the initial energy scale Q^2 down to the hadronisation scale, of order 1 GeV, associated to the confinement of the partons inside the hadrons. The radiation from incoming particles is usually referred to as initial state radiation, while emissions from the final state partons is called final state radiation. In both cases, the probability to radiate a parton is controlled by the so-called Sudakov form factor [65], which describes the probability for a parton q to not radiate in the time interval Δt. This probability depends on the hard scatter energy scale, the parton type and the initial momentum fraction carried.

The radiation emission is controlled by a "time-dependent" variable, ensuring that the subsequent emission happens at lower energy with respect to the previous one. The choice

of the evolution variable can differ across generators: the opening angle (HERWIG [66]) or the transverse momentum (PYTHIA8 [67]) approaches are two possible choices.

After the ME and the PS are simulated a careful matching has to be done in order to remove the overlapping diagrams and cover the entire phase space. The ME is typically used to describe the production of hard and well separated particles, while the PS is employed for soft and collinear particles. The scale at which the two simulations are combined is called matching scale.

Hadronisation

When the partons involved in the PS reach the hadronisation scale, they are combined into colour-neutral states, as required by QCD. The models describing the process of hadronisation depends on many free parameters that have to be tuned to match the data.

There are two main models currently in use to simulate the hadronisation process; the Lund string Model [68], used by PYTHIA, and the cluster model [69], used by HERWIG and SHERPA [70]. The main difference between the two models is that the former transforms the parton system directly into a hadron, while the latter introduces an intermediate stage in which clusters of partons with mass scale of 1 GeV are formed.

Underlying event

The underlying event refers to any additional activity which is not related to the hard process. This includes all interactions involving the partons from the incoming protons not involved in the hard scatter, as well as from any additional partons radiated in the event. These events are simulated using phenomenological models tuned to the data.

Decays of unstable particles

After the hadronisation step, the decays of the several unstable particles produced in the event is simulated and the final state stable particles, that can interact with the detector, are determined.

By default, only decays of particles with a proper decay length of $c\tau < 10$ mm, with τ being the decay time, are handled by the event generator, and their possible interactions with the detector material, as well as their curvature inside the magnetic field, are ignored. An exception is made in the case of long-lived particles, for which this limit on the maximum $c\tau$ is relaxed and therefore their decay is simulated by the event generator also at longer distances.

Particles that are considered stable by the event generator have their decays and interactions with the detector handled by the simulation and are referred to as particle-level objects.

ATLAS detector simulation

Particle-level objects are fed to the ATLAS detector simulation, which is based on the GEANT4 software [71]. The simulation is kept updated and takes into account the complete detector geometry, including misalignments or distortions, detector performances and data-taking conditions.

The output of the simulation consists of a list of "hits" representing all the information on the energy deposits, positions and times in the sensitive material of the detector. At this stage, simulated hits are used as input to a digitisation step, overlaid with simulated hits from pile-up and backgrounds originating from the LHC beams. The digitisation step also simulates the electric signals induced in the read-out components of the detector and possible electronic noise.

The last step of the ATLAS simulation is the reconstruction, which combines the information from the different sub-detectors to reconstruct the actual physics object that produced the signal. The reconstruction is performed both on data and MC generated events.

For all the signal and background samples considered, in order to model the effect of pile-up, simulated inclusive pp events are overlaid on each generated event and reweighted to match the conditions of the 2015-2018 data sample. The multiple interactions were simulated with Pythia8.210 [72] with the A3 tune [73] and the NNPDF2.3lo set of parton distribution functions [64].

3.3.2 Signal samples

MC simulated event samples are used to model the BSM signals. Signal samples modelling the production of dark-photons via a 125 GeV Higgs portal were generated with MadGraph5_aMC@NLO 2.2.3 [74] interfaced to Pythia 8.186 [72] for the parton showering and hadronisation. The matrix-element calculation was performed at tree level. The PDF set used for the generation is NNPDF2.3lo [64].

Higgs boson production via gluon-gluon fusion and in association with a W boson is included. The predicted Standard Model cross-sections for these two processes, assuming $m_H = 125.09$ GeV, are respectively 48.61 pb [75, 76] and 1.37 pb [16, 77]. A second set of signal samples was generated, modelling the production via gluon-gluon fusion of a high-mass (800 GeV) Higgs-like scalar mediator with the same decay modes as in the 125 GeV mass case. Effects of higher-order QCD corrections on the p_T of the Higgs boson, evaluated using a reweighting procedure [78], change the signal selection efficiency by less than the MC statistical accuracy and are therefore neglected. The cross-section for a 800 GeV Higgs calculated at N3LO [76] is set for reference as $\sigma_{\text{BSM}} = 5$ pb.

A dark-photon with a mass m_{γ_d} up to a few GeV that mixes kinetically with the SM photon will decay into leptons or light quarks, with branching fractions that depend on its mass [1, 31, 79]. Taking as an example a dark-photon mass of 0.4 GeV, the dark-

photon decay branching ratios are expected to be 45% e^+e^-, 45% $\mu^+\mu^-$, and 10% $q\bar{q}$ [31]. The mean proper decay length $c\tau$ of the dark-photon is a free parameter of the model. In the generated samples, cτ was chosen such that, accounting for the boost of the dark-photon, a large fraction of the decays, on average around 80-90%, occur inside the sensitive ATLAS detector volume (i.e. up to 7 m in radius and 13 m along the z-axis from the centre of the detector).

The decays of the Higgs boson into dark-photons through dark fermions or directly into two dark-photons were simulated at matrix element level during the generation. In the case of the FRVZ model (see Section 1.2.3), the mass of dark fermion f_d was chosen to be small relative to the Higgs boson mass and far from the kinematic threshold at $m_{\mathrm{HLSP}} + m_{\gamma_\mathrm{d}} = m_{f_\mathrm{d}}$. In the case of the HAHM model (see Section 1.2.3), the Higgs boson decays directly into two dark-photons. Finally, an additional set of events has been generated fixing the branching ratio of the dark-photon to hadronic decays only. These samples have been used only for the optimisation of the neural network taggers and are not used for the statistical analysis.

The mass range of the dark-photon in the simulated samples is 17 MeV - 15 GeV, with the lower bound motivated by the recently proposed $X17$ particle [80] and upper bound motivated by the low Lorentz boost configuration involved with increasing masses of the dark-photon. For each mass sample, the choice of the corresponding proper decay length $c\tau$ was made in order to allow on average around 80-90% of the dark-photon decays to occur inside the ATLAS detector volume, resulting in $c\tau$ values ranging from 10 mm to 1000 mm. In order to fully exploit the coverage of the analysis in the phase space, consisting of the dark-photon mass m_{γ_d} and proper decay length $c\tau$, a dedicated re-weighting procedure is used (see Chapter 6). More details on the signal samples can be found in Chapter 5.

3.3.3 SM background processes

There are several SM processes that could lead to potential sources of background for the analysis described in this thesis. Simulated samples are generated to study those backgrounds. Since different Higgs boson production modes are considered, the relative impact of some of these processes will vary depending on the production mode under study.

The main source of background for the ggF production comes from multijet events. The relative MC samples were generated with Pythia 8.210 using the same tune and PDF used for the production of signal samples.

In the case of the WH associated production, the SM processes that could lead to potential sources of background include W+jets, Z+jets, $t\bar{t}$, single-top-quark, WW, WZ, and ZZ production events. Among these, the main contribution is given by the W/Z+jets processes.

W+jets, Z+jets , WW, WZ, and ZZ events were generated using Sherpa 2.2.2 [81] with the NNPDF 3.0 NNLO [63] PDF set.

Single top and $t\bar{t}$ MC samples were generated using POWHEG-BOX 1.2856 [82] and PYTHIA 6.428 [83] with the PERUGIA2012 [84] tune for parton showering and hadronisation, and CT10/CTEQ6L1 [85, 86] PDF sets.

Finally, MC samples of $J/\Psi \to \mu\mu$ events are generated to evaluate systematic uncertainties for muon trigger and reconstruction efficiencies. The MC samples are generated using PYTHIA8+PHOTOS++ [87] with the A14 tune for parton showering and hadronisation and the CTEQ6L1 PDF set.

Chapter 4

Objects reconstruction and identification

The elementary particles, produced in LHC collisions and used for physics results, are not directly observed in the ATLAS detector. Those particles are detected through their interaction with the various sub-systems of the detector. In order to search for the particles produced in the collision, effective reconstruction and identification algorithms are needed. In this chapter, the identification and reconstruction techniques of the different physical objects in ATLAS are described. A particular focus is put on muons, electrons and jets, the main objects of interest in the analysis work described in this thesis. Standard object definitions are usually recommended by the ATLAS collaboration, but further optimisation can be done at analysis level to improve the selection and maximise the sensitivity to the signal of interest. The reconstruction is a multi-stage process designed to find particle-like signatures starting from tracks and calorimeter clusters of deposited energy, built using the detector signals. The reconstructed objects are then combined and classified into high-level physics objects, e.g electrons or jets, with all the measured physical properties, such as their momenta, energy or charge.

4.1 Track and vertex reconstruction

Tracks

Tracks are one of the most basic elements used for particle reconstruction in ATLAS. They are reconstructed from hits in the inner detector. Pixel and SCT hits are clustered to improve the accuracy of the position measurement and to reduce the noise from front-end electronics. After cluster creation, the track-finding algorithm searches for three-point tracks in the silicon detectors [42]. These tracks are then extrapolated into the outer regions of the tracking detector by iteratively associating new clusters to the track and updating the track parameters.

This algorithm is designed to find charged particles arising from the collision point. The hits from the TRT are combined in an opposite direction, as they are extrapolated towards the silicon detectors by a back-tracking algorithm. This algorithm finds tracks which do not originate from the interaction region.

The tracks reconstructed by the track-finding algorithm are required to have transverse momentum $p_T > 500$ MeV. The space coordinates of a track are also important. They are described by the shortest distance in transverse and longitudinal direction between the interaction point and the track. These are also known as the transverse impact parameter, denoted as d_0, and the longitudinal impact parameter, denoted as z_0.

Since multiple tracks might share the same hit, an ambiguity-solving algorithm is run. A score is assigned to each track, based on the χ^2 of the track fit, on its p_T, and on the number of holes in the track, which is defined as the number of expected hits which are not present in one layer of the inner detector.

Vertices

Tracks are used to define another basic element used for particle reconstruction in ATLAS, the vertices. The point where the hard scattering occurred is the primary vertex, defined as the one with the highest sum of the square of transverse momenta of the associated tracks. If the particles produced in the primary vertex live long enough to decay further away, a secondary vertex is formed.

Vertices are reconstructed using an iterative vertex finding algorithm [88]. Vertex reconstruction proceeds by calculating the crossing point of several tracks and iteratively adding or discarding all tracks that are respectively compatible or incompatible with originating from this crossing point. In this process, the vertex position is updated with each change of the track association.

Secondary vertices provide crucial information for heavy flavour identification, since heavy flavoured hadrons usually have long lifetimes, such that they can decay several millimetres from the collision point.

4.2 Electrons

Electrons are reconstructed with combined information from energy deposits in the ECAL and associated tracks in the inner detector. Once the electron candidates are reconstructed, they must undergo an identification procedure. The electron candidates are discriminated from background by a likelihood-based identification algorithm, which exploits several properties from track information to calorimeter shower shapes. Correctly identified electrons are then classified in three quality categories, referred to as working points: loose, medium, and tight. Electrons selected by a tighter working point are also contained in the looser selections. The electron identification algorithm performance is presented in Figure 4.1 for

electrons from $Z \to e^+e^-$ events as a function of the electron E_T and η.

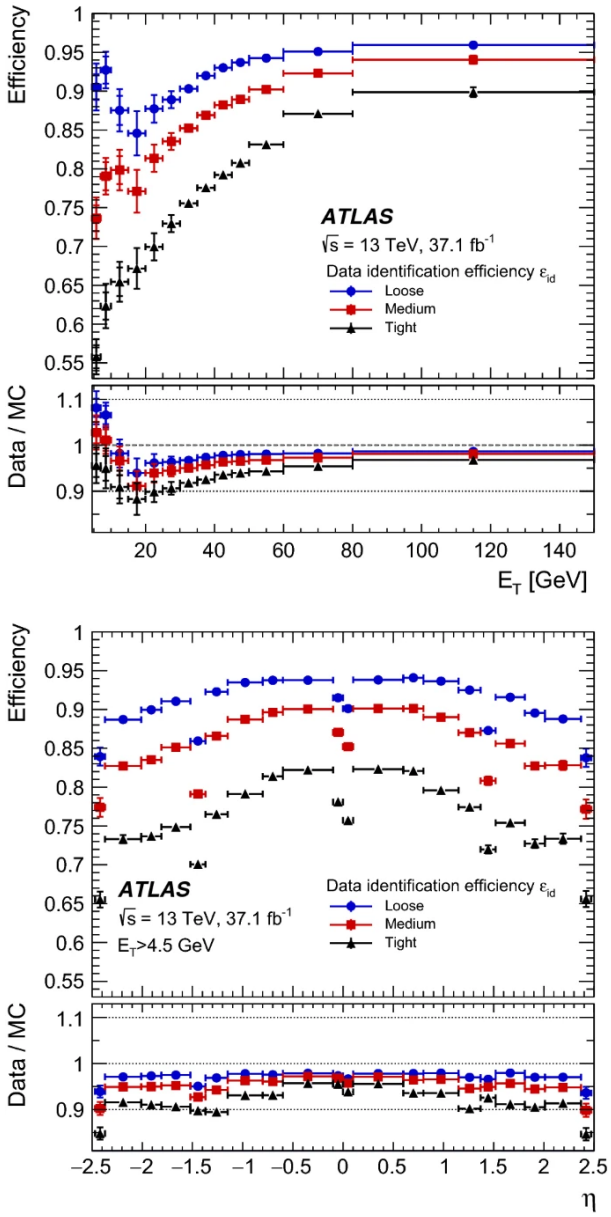

Figure 4.1: Measured electron-identification efficiencies in $Z \to e^+e^-$ events for the loose (blue circle), medium (red square), and tight (black triangle) operating points as a function of transverse energy (up) and η (down) [89].

High energy electrons tend to deposit more energy in the last ECAL layers or in the early HCAL layers, presenting narrower cascade shapes. To take into account this effect, the loose and medium selections criteria are constructed to be robust against E_T dependence.

Additional cuts on electron discriminating variables are included in the tight selection to maintain a good efficiency for electron candidates with high E_T. Requirements on the number of hits in the ID are added to the electron selection to further suppress background

from non-prompt electrons, such as electrons originating from converted photons.

Analyses using low energy electrons usually choose a tight isolation requirement for high background rejection, while those using high energy electrons may prefer a loose isolation for a high signal efficiency.

In the analysis presented in this thesis, electron candidates are reconstructed from isolated electromagnetic calorimeter energy deposits matched to inner detector tracks. They are required to have $|\eta| < 2.47$, a transverse momentum $p_T > 20$ GeV, and to satisfy the "tight" identification requirement. Candidates within the transition region between the barrel and endcap electromagnetic calorimeters, i.e $1.37 < |\eta| < 1.52$, are not considered. In addition, tracks associated with an electron candidate are required to pass a cut on the significance of the transverse impact parameter, d_0, of $|d_0|/\sigma(d_0) < 5$, and on the longitudinal impact parameter, z_0, $|z_0 \sin(\theta)| < 0.5\ mm$, with θ being the polar angle that the particle forms with beam axis.

Finally, the scalar sum of the p_T of tracks within a variable-size cone around the electron must be less then 15% of the electron p_T, excluding tracks associated with the electron itself, and the sum of the transverse energy of clusters of calorimeter cells in a cone of $\Delta R = 0.2$ around the electron must be less than 20% of the electron p_T, also in this case excluding clusters already associated with the electron object.

4.3 Muons

ATLAS muon reconstruction [90] exploits the information provided by the inner detector and the muon spectrometer sub-detectors, leading to four muon types being defined:

- Combined (CB): combination of the independent tracks reconstructed in the inner detector and muon spectrometer. Provides the best purity and best momentum resolution;

- Segmented-tagged (ST): inner detector track associated with at least one local track in the MDT or CSC chambers. The ST selection is used for low-p_T muons or muons falling outside the muon spectrometer acceptance regions;

- Calorimeter-tagged (CT): combination of inner detector tracks and matched energy deposits in the calorimeter compatible with a minimum ionising particle. This identification criteria is optimised to recover acceptance in the region $|\eta| < 0.1$, where the ATLAS muon spectrometer is only partially instrumented to allow for cabling and services.

- Standalone (SA, msonly): reconstruction using only the information provided by the muon spectrometer. The muon track is required to have hits in at least three layers in the barrel or in the end-caps, and to be compatible with a muon originating from

the impact parameter. In standard analyses SA muons are used in the pseudorapidity outside the inner detector range $2.5 \leq |\eta| \leq 2.7$;

In the analysis presented in this thesis, Standalone muons are used in the whole pseudorapidity range to select displaced decays that would not leave any track in the inner detector. In addition, the analysis loosens the standard SA criteria requiring to have at least two hit in the barrel, instead of three, to be able to reconstruct dark-photon decays that occur after the innermost MDT layer.

Muon identification algorithms, similar to the ones used for electrons, are also used to suppress the background, which comes primarily from pion and kaon decays. In this way four working points are defined:

- Loose: designed to maximise the reconstruction efficiency while providing good-quality muon tracks;
- Medium: designed to minimise the systematic uncertainties associated with muon reconstruction and calibration. Only CB and MS muons are considered, with additional requirement on the number of hits in muon chambers, and a loose requirement on the compatibility between p_T measurements in the inner detector and muon spectrometer;
- Tight: selected to maximise the purity of muons at the cost of some efficiency losses. Only CB muons with at least two hits in muon spectrometer and satisfying the medium criteria are considered. Additional requirements on normalised χ^2 of the track fit and the compatibility between inner detector and muon spectrometer p_T measurements is employed to further reject background;
- High-p_T muons: optimised for searches for high-mass resonances, in order to maximise the momentum resolution for muons with $p_T > 100$ GeV, CB muons satisfying medium requirements and having at least three hits in three MS stations are included. Regions of the muon spectrometer where the alignment is suboptimal are vetoed.

The displaced dark-photon jet analysis adopts the medium selection to maximise the reconstruction efficiency while retaining good quality muons. The medium quality efficiency for prompt muons as a function of the p_T is presented in Figure 4.2, obtained with $Z \rightarrow \mu^+\mu^-$ and $J/\Psi \rightarrow \mu^+\mu^-$ samples.

ATLAS standard muon isolation is not adopted in the analysis as no tracks are expected in the inner detector for the signal of interest. Only a custom isolation is applied in the analysis. Muon candidates are reconstructed in the region $|\eta| < 2.5$ from muon spectrometer tracks matching inner detector tracks. They are required to have $p_T > 20$ GeV and satisfy the "medium" identification requirements defined in [90]. These requirements are based on the number of hits in the different inner detector and muon spectrometer subsystems, and on the ratio of the measured charge and momentum (q/p) divided by the sum in quadrature of their corresponding uncertainties. Tracks associated to muon candidates are required to

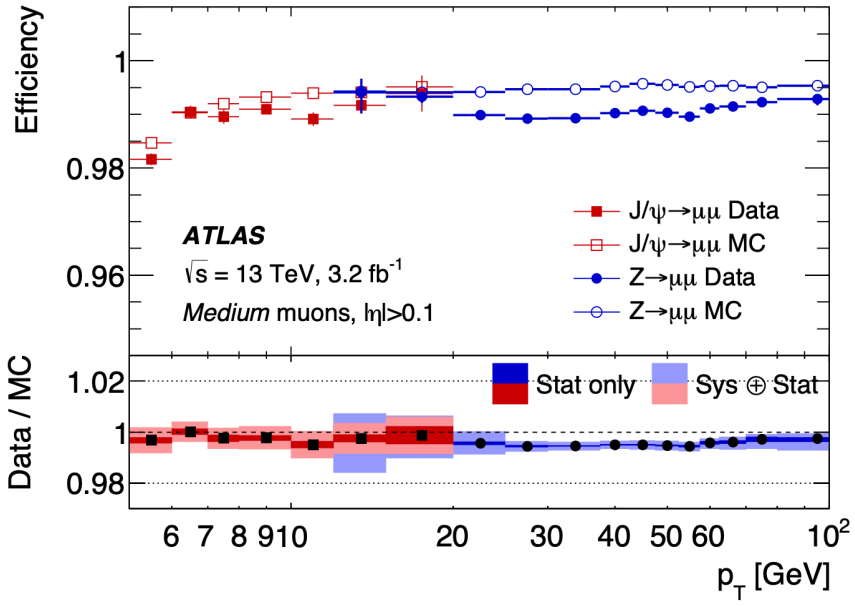

Figure 4.2: Reconstruction efficiency for the medium muon selection as a function of the transverse momentum of the muon, in the region $0.1 < |\eta| < 2.5$ obtained with $Z \to \mu^+\mu^-$ and $J/\Psi \to \mu^+\mu^-$ events [90].

pass a cut on both transverse and longitudinal impact parameter, similarly to the electron case, of $|d_0|/\sigma(d_0) < 3$ and $|z_0 sin\theta| < 0.5$ mm respectively.

Finally, the scalar sum of the p_T of tracks within a variable-size cone around the muon, must be less then 15% of the muon p_T, excluding tracks associated with the muon itself, and the sum of the transverse energy of clusters of calorimeter cells in a cone of $\Delta R = 0.2$ around the muon must be less than 30% of the muon p_T, also in this case excluding clusters associated with the muon. This is done in order to avoid a possible overlap with other objects.

4.4 Jets

The hadronisation of quarks and gluons produces a spray of collimated hadrons called jet. In the analysis described in this thesis, jets are originated by displaced dark-photon decays into electron or hadron pairs in the hadronic calorimeter. These jets are expected to be isolated in the inner detector, with most of the energy deposits occurring in the HCAL, and to appear to be narrower than ordinary jets.

ATLAS jets are reconstructed from topological clusters of energy deposits in the calorimeters using the anti-k_t clustering algorithm [91,92] with a distance parameter $R = 0.4$. Anti-

k_t is a sequential clustering algorithm based on the evaluation of the distance d_{ij} between two clusters (i, j) and the distance d_{iB} between the pseudo-jet and the beam (B), defined as:

$$d_{ij} = min(p_{T,i}^{2p}, p_{T,j}^{2p}) \cdot \frac{\Delta R_{ij}^2}{R^2},\ d_{iB} = p_{T,i}^{2p}, \tag{4.4.1}$$

where $p_{T,i}^{2p}$ is the transverse momentum of the i-th object and p is the algorithm parameter $p = -1$. The clustering begins with the hardest constituent i as seed. For each iteration, all distances d_{ij} between the i-th constituent and all other constituents j are computed. If the minimum value of the d_{ij} set is smaller than d_{iB}, then the i-th and the j-th constituent are combined into a single pseudo-jet summing the four-momenta. In the following iteration, the pseudo-jet will be used as seed and the i-th and j-th constituents will no longer be considered. Instead, if $d_{ij} \geq d_{iB}$, the pseudo-jet is considered as a jet. Clustering ends when only jets are left in the event. This algorithm tends to cluster soft particles with hard objects before clustering between themselves. For example, an isolated hard particle will cluster all soft particles within a $2R$ distance in a size R cone, resulting in a conical-shape jet. The algorithm is, therefore, sensitive only to hard particles proximity at the disadvantage of soft radiation. Jet objects are then calibrated in energy to correct for non-linearities in the calorimeter response, leakage and mis-reconstruction by weighting the energy deposits arising in the ECAL and HCAL accordingly. An additional correction due to pile-up may be also applied.

In the analysis detailed in the following chapters, the anti-k_t is used with a jet radius parameter $R = 0.4$. Only jet candidates with $p_T > 20$ GeV and $|\eta| < 4.9$ are considered.

Jet Vertex Tagger

The Jet Vertex Tagger [93] (JVT) is a technique used in ATLAS for pile-up suppression. JVT uses a multivariate combination of the following pile-up sensitive track information:

- Jet Vertex Fraction (JVF): defined as the ratio of the scalar sum of the transverse momentum of the associated tracks that originate from the PV to the scalar sum of the transverse momentum of all associated tracks, corrected with the average scalar sum of pile-up associated tracks. It is used to select jets originating from the PV;

- R_{pT}: defined as the scalar sum of the transverse momentum of the tracks that are associated with the jet and originate from the hard-scatter vertex, divided by the fully calibrated jet p_T, which includes pile-up subtraction.

In Figure 4.16, the distribution of JVF and R_{pT} are presented for pile-up (PU) and hard- scatter (HS) jets with $20 \leq p_T \leq 30$ GeV.

The JVT uses a k-nearest neighbour (kNN) algorithm [94] trained on these two variables to differentiate between pile-up jets and jets originating from the primary vertex. The tagger output is shown in Figure 4.4a for pile-up and hard-scatter jets. As shown in Figure 4.4b,

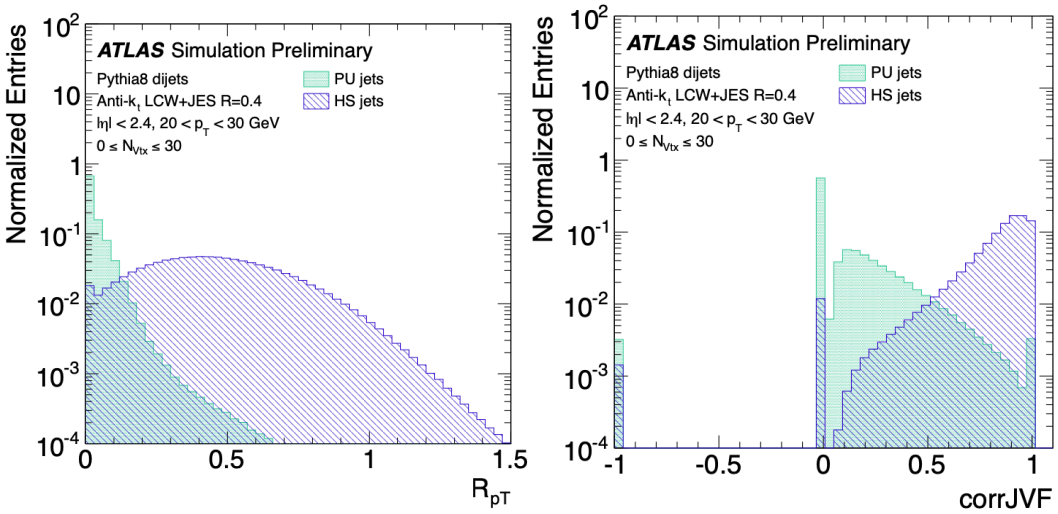

(a) (b)

Figure 4.3: JVT input variables distribution [93], R_{pT} (a) and JVF (b) for pile-up (PU) and hard-scatter (HS) jets with $20 \leq p_T \leq 30$ GeV.

the JVT signal efficiency is independent of the number of PV in the event, therefore optimal for pile-up suppression and robust against its increase. Since dark-photon jets produced in the hadronic calorimeter have a JVT output distribution similar to the one of pile-up jets, in this search the JVT output is used oppositely to the typical ATLAS implementation.

Jet energy scale and resolution

The jet energy calibration is needed to compensate for all possible detector loss effects in the calorimeters, e.g. presence of dead detection material or reconstruction inefficiencies. The goal is to correct the jet energy to the true process, this operation is referred to as Jet Energy Scale (JES) calibration process. JES calibration starts with pile-up subtraction and origin correction, which has the aim to make the jet point back to the hard-scatter vertex. The topological clusters kinematic properties are then recomputed leaving the energy unchanged. Finally, the jet response is corrected by applying energy corrections in transverse momentum and pseudorapidity bins from the simulated MC jet response (E_{reco}/E_{truth}). The calibration process is described in detail in Ref. [95].

The systematic uncertainties associated to the calibration procedure are taken into account. The JES uncertainty is well described by the variation applied by the calibration to the mean value of the jet response distribution.

An additional source of systematic uncertainty arises from the Jet Energy Resolution (JER), which quantifies the width of the Gaussian jet response distribution. The JER uncertainty takes into account many different effects, from the stochastic nature of hadronic showers to electronic noise.

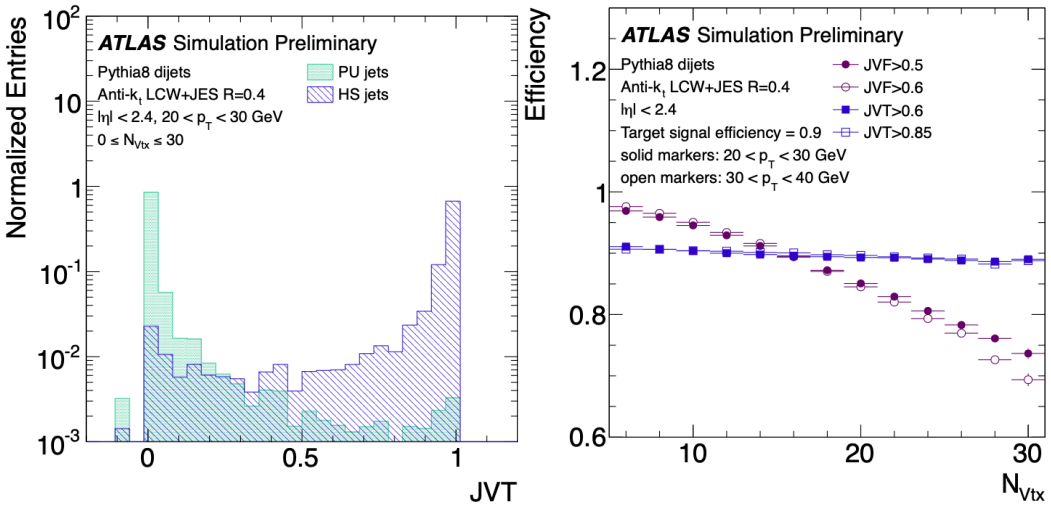

(a) (b)

Figure 4.4: (a) JVT output distribution for pile-up and hard-scatter jets. (b) Primary-vertex dependence of the hard-scatter jet efficiency for $20 \leq p_T \leq 30$ GeV (solid markers) and $30 \leq p_T \leq 40$ GeV (open markers) jets for fixed cuts of JVT (blue square) and JVF (violet circle) such that the inclusive efficiency is 90 %.

Jet cleaning

The anti-k_T procedure might lead to the reconstruction of spurious jet objects, referred to as fake jets. Fake jets are usually rejected in analyses through a set of selections called jet-cleaning criteria [96]. However, in this analysis, standard procedures of jet-cleaning cannot be utilised because they would suppress jets with high values of E_{HCAL}/E_{ECAL}, which represents the ratio between the energy released by a jet in the hadronic calorimeter (E_{HCAL}) and in the electromagnetic calorimeter (E_{ECAL}), which is a typical discriminant used for the identification of a signal displaced jet.

A dedicated cleaning algorithm for displaced jet in the HCAL has been developed, referred to as Loose-LLP, and is applied to the jet objects, with no requirements on the ratio E_{HCAL}/E_{ECAL}. Jets are required to have transverse momentum $p_T > 20$ GeV and $|\eta| < 2.5$. In addition to this, the weighted mean time difference between $t = 0$ (bunch-crossing time) and the time of the energy deposit in the calorimeter cells is required to be in the range [-4 ns, 4 ns] to reduce cosmic-ray background and beam-induced background jets. No cleaning is applied to jets with $|\eta| > 2.5$ as they lie outside the coverage of the ATLAS inner detector.

4.4.1 Prompt jets

A standard collection of prompt jets is also considered in the analysis. This collection is used in the selection to veto VBF events, and in the associated production category

those jets are used to reduce the amount of multijet background events. Standard jets are required to have a p_T greater than 20 GeV and an absolute pseudo-rapidity less than 4.9. Standard jets are calibrated following the standard ATLAS procedure. To reduce the effects of pile-up, jets with $p_T < 120$ GeV and $|\eta| < 2.5$ are required to have a significant fraction of their associated tracks compatible with originating from the primary vertex, as defined by the jet vertex tagger [93]. This requirement reduces the fraction of jets from pile-up to 1%, with an efficiency for hard-scatter jets of about 90%.

Finally, jets which are already used to reconstruct a dark-photon jet are removed from this collection in order to avoid any overlap between the two collections.

4.4.2 Identification of b-jets

For both measurements of SM processes and searches for BSM physics, identifying jets originating from b-quarks is extremely important. b-quarks produced in the hard scatter hadronise and then travel a significant distance before decaying. The result of this is the presence of a second decay vertex, distinct from the primary vertex, with tracks which have large impact parameters. This distinctive signature enables jets originating from a b-quark to be "tagged". In ATLAS, jets containing b-hadrons (b-tagged) are identified with the MV2c10 algorithm [97, 98], a multivariate discriminant that makes use of track properties. Jets are considered to be b-tagged if they fulfil a requirement that has 70% average efficiency for jets containing b-hadrons in simulated $t\bar{t}$ events. The rejection factors for light-quark and gluon jets, jets containing c-hadrons, and hadronically decaying τ-leptons in simulated $t\bar{t}$ events are approximately 301, 38, and 8, respectively.

Simulated events are corrected for differences from collision data in b-tagging efficiencies and b-tagging mis-tag rates [98–100]. Corrections are also applied to account for minor differences between data and MC simulation in the single-lepton trigger, reconstruction, identification and isolation efficiencies [101, 102].

In the analysis presented later in this thesis, b-tagging is used to veto events containing b-tagged jets.

4.5 Overlap Removal

During the reconstruction process, it can happen that the same energy deposit is associated to multiple objects. This issue is solved with an overlap removal process. Jet candidates within an angular distance $\Delta R = \sqrt{(\Delta y)^2 + (\Delta\phi)^2} = 0.2$ of a lepton candidate are discarded. Remaining lepton candidates within $\Delta R = \min[0.4, 0.04 + p_T(\mu)/(10\ GeV)]$ of a jet are then discarded to suppress bottom and charm hadron decays. When considering muons, if the jet has fewer than three associated tracks, the muon is retained and the jet is discarded instead, in order to avoid inefficiencies for high energy muons undergoing significant energy loss in the calorimeter. Finally, any electron candidate sharing an inner

detector track with a remaining muon candidate is also removed.

4.6 Missing transverse momentum

The missing transverse momentum vector p_T^{miss}, whose magnitude is denoted by E_T^{miss}, measures the momentum imbalance in the transverse plane in the event. If a particle produced in a pp collision escapes ATLAS undetected, as for neutrinos or other neutral weakly interacting particles predicted by several BSM theories, it will cause a momentum imbalance in the transverse plane. Other effects that may lead to an E_T^{miss} contribution are object mis-reconstruction or the presence in the event of particles escaping a not completely hermetic detector.

Missing transverse energy is characterised by a hard term, which includes all the fully reconstructed objects, and a soft term, which includes contributions from detector signal objects not associated with any specific reconstructed object. It is defined as the negative vector sum of the momenta of the respective calibrated objects and computed as follow:

$$\vec{E}_T^{miss} = -\left(\sum_{i \,\epsilon\, hard\ terms} \vec{p}_{T,i} + \sum_{i \,\epsilon\, soft\ terms} \vec{p}_{T,i} \right) \tag{4.6.1}$$

In the analysis described in Chapters 5 and 6, a loose E_T^{miss} cut is applied to ensure orthogonality with respect to the VBF dark-photon jet analysis in order to allow a future combination between the analyses. In addition, in the WH category, an E_T^{miss} cut is applied in order to reduce contributions from standard model backgrounds.

Part II

Search for light long-lived neutral particles in Full Run-II ATLAS data

Chapter 5

Dark-Photon Jets and the Full Run-II displaced analysis

This chapter summarises the methods and tools used to perform the search for light long-lived neutral particles described in this thesis. The main target of the analysis are long-lived dark-photons, with masses ranging from twice the electron mass and up to 15 GeV, arising from Higgs Boson decays. Two different Higgs production mechanisms are taken in consideration, ggF and WH production. Values of the kinetic mixing term in the range $10^{-7} < \epsilon < 10^{-4}$ are probed. The mass and kinetic mixing values probed are chosen in such a way that the dark-photon results to have a non-negligible lifetime. This is due to the existing relation between those three quantities, as shown in Equation 1.2.5. The dark-photon is also expected to be produced with large Lorentz boost, given the fact that its mass ranges in values much lower than the Higgs Boson mass. As a consequence of this, the dark-photon decays far from its primary production point, generating collimated groups of leptons and light quarks that form a jet-like structure, which are referred to as Dark-Photon Jets (DPJs).

The chapter is organised as follows. An overview of the analysis is given in Section 5.1. The types of DPJs, as well as the tools used for their reconstruction, are introduced in Section 5.2. The Machine Learning (ML) methods adopted in this analysis are presented in Section 5.3. The event selection is described in Section 5.4. The treatment of the various backgrounds, and the description of the background estimation techniques, is presented in Section 5.5.

The results and the methods used to draw statistical conclusions from the analysis are later described in detail in Chapter 6.

5.1 Analysis overview

The DPJ signature represents a tough challenge for both the trigger and the reconstruction capabilities of the ATLAS detector, which is optimised for prompt decays. Moreover, differ-

ent signatures are generated depending on the nature of the dark-photon decay. The DPJs are characterised by an unconventional experimental signature, which can be exploited to remove a large fraction of events, not of interest for the analysis. However, this has also the disadvantage of bringing into play unusual events, such as beam-beam remnants, cosmic rays and punch-through jets, that can mimic the DPJ signature. For this reason, dedicated ML methods used for signal selection and background rejection have been developed. In the displaced DPJ analysis, the events are classified in two mutually exclusive search categories, referred to as gluon-gluon fusion selection and WH associated production selection, which are designed to target the production of dark-photons in these two Higgs boson production modes. The event selection aims at the identification of six orthogonal Signal Regions (SRs), where events are selected depending on the relative Higgs boson production mode and on the number and type of reconstructed DPJs. Of all the different background contributions, the one due to rare jets, from either multijet events or V+jets events, is expected to be the leading one and is estimated with a data-driven method. Other backgrounds, when present, are either reduced to a negligible level or estimated in a control sample and taken into account during the data-driven estimation.

5.2 Dark-Photon Jets

Dark-photon jets are a custom physics object built with the aim of identifying displaced long-lived particles decaying in collimated muon, electron or quark pairs. The cuts listed in the following have been tuned on the simulated samples to correctly reconstruct the dark-photons in the investigated mass and lifetime ranges. Those cuts are the same used in the previous version of this analysis [3]. Depending on the decay mode of the dark-photon, two definitions of DPJs are used:

- **μDPJ**: a dark-photon decaying into a pair of muons is expected to leave two collimated standalone tracks in the muon spectrometer, with no jets found in a cone of $\Delta R = 0.4$. A DPJ satisfying these characteristics is classified as a muonic DPJ (μDPJ).

- **cDPJ**: a dark-photon decaying into a displaced electron or quark pair, is searched for as an energy deposit in the calorimeters identified as a single jet with an EM fraction (f_{EM}), defined as the ratio of the energy deposited in the EM calorimeter to the total jet energy, below 0.4. In addition, no associated standalone muon tracks has to be found in a cone of $\Delta R = 0.4$ around the jet. A DPJ with these characteristics is classified as calorimeter dark-photon jet (cDPJ).

A graphical representation of the two DPJ categories is shown in Figure 5.1. More details on the properties and the reconstruction of DPJs is given in the following.

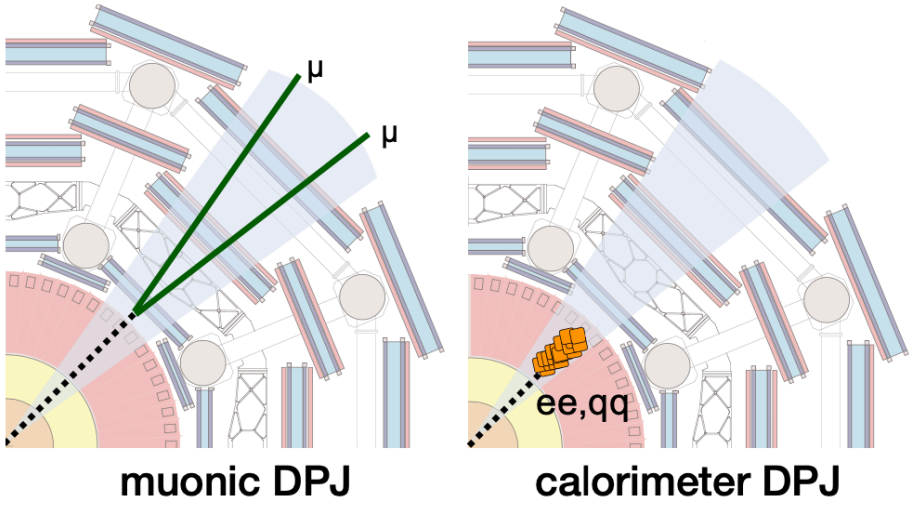

Figure 5.1: Graphical representation of the two DPJ categories: μDPJ (left) and cDPJ (right). Muonic DPJs are built from at least two collimated standalone muon spectrometer tracks, required to not be matched to any jet. Calorimeter DPJs are built from jets with EM fraction below 0.4, not matching any standalone muon spectrometer track.

5.2.1 Muonic dark-photon jets

As mentioned above, a dark-photon decaying into a pair of muons is expected to leave two collimated standalone muon tracks in the muon spectrometer. Standalone MS tracks [90] are formed by requiring at least two matched segments in the muon spectrometer, which are fit with a primary vertex constraint. In addition, a special selection on the standalone track information obtained from the Muon Spectrometer is needed:

- in order to discard muons originating from the primary vertex, the track must not have been used to build a combined muon;
- only standalone MS tracks in the pseudorapidity interval $|\eta| < 2.4$, corresponding to the ATLAS inner detector coverage, are selected;
- candidates with pseudorapidity in the range $1.0 \leq |\eta| \leq 1.1$ are rejected to avoid the transition region of the muon spectrometer between barrel and endcap.

μDPJ reconstruction

Muonic dark-photon jets are reconstructed using the Cambridge-Aachen clustering algorithm [103] that combines all the standalone MS tracks lying within a cone of fixed size in (η, ϕ) space. The algorithm used has remained unchanged since the previous version of this analysis [3]. The algorithm starts from the highest-p_T standalone MS track, searching for additional standalone MS tracks within the $\Delta R \leq 0.4$ cone around the initial track momentum vector. If a second standalone MS track is found in the cone, the axis of the cone is changed to the vector sum of the momenta of the two tracks; the search is repeated

until no additional tracks are found in the cone. μDPJs are required to have at least two muon spectrometer tracks and they are discarded if a jet is found within $\Delta R \leq 0.4$ from a μDPJ. This is done to ensure the orthogonality between reconstructed DPJs of different types.

The μDPJs reconstruction efficiency can be defined as the ratio of the number of dark-photons decaying in $\mu^+\mu^-$ which are found in a $\Delta R = 0.4$ cone around a μDPJ and the total number of dark-photons decaying in two muons. The reconstruction efficiency is shown in Figure 5.2 for μDPJ objects with $|\eta| < 1$ as a function of L_{xy} and transverse momentum of the dark-photon for few benchmark signal scenarios relative to the HAHM and FRVZ model. The discrepancies between the signal scenarios shown are expected, as the topology of the decay depends on the different kinematics of each configuration. A drop in efficiency is expected for dark-photon decays which occur after the middle layer of the muon spectrometer (∼6 m in the barrel region), where muons can no longer be reconstructed.

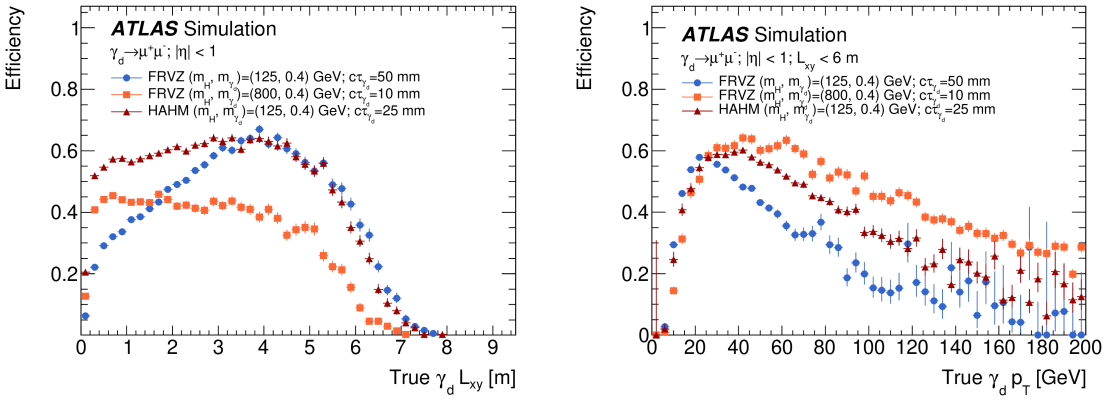

(a) (b)

Figure 5.2: The reconstruction efficiency for μDPJ objects in the decay of a γ_d to muon pairs. Figure (a) shows the reconstruction efficiency for γ_d with $0 < |\eta| < 1.1$ as function of the transverse decay length L_{xy}. Figure (b) shows the reconstruction efficiency for γ_d with $0 < |\eta| < 1.1$ as function of the γ_d transverse momentum, in events where the γ_d L_{xy} is below 6 m. The differences between the various signal scenarios are expected as the topology of the decay depends on the different kinematics of each configuration. Finally, a drop in efficiency is expected for dark-photon decays occurring after the middle layer of the muon spectrometer (∼6 m in the barrel region).

5.2.2 Calorimeter dark-photon jets

Calorimeter dark-photon jets aim to identify a dark-photon decaying into a displaced electron or quark pair outside the radial acceptance of the ATLAS ECAL. Given the high boost of the dark-photon, the resulting electrons and quark pairs will be highly collimated.

Therefore, the cDPJ is searched for as an energy deposit in the calorimeters identified as a single jet, reconstructed and calibrated with the same algorithms described in Section 4.4, and satisfying the following requirements:

- The jet must have $f_{EM} < 0.4$, $p_T > 20$ GeV and must lie within the pseudorapidity interval $|\eta| < 2.5$.
- No standalone muon spectrometer track must be identified in a cone of $\Delta R = 0.4$ centered around the jet axis.
- The jet is required to satisfy a looser object quality criteria with respect to the main jet selection, referred to as Loose-LLP in Section 4.4, and no selection on jet-vertex tagger is applied in order to retain high efficiency for the targeted signals.
- Candidates in the transition region between the barrel calorimeters and the endcap cryostat are removed by requiring the fraction of the energy released by the jet in the Tile Gap scintillators to be less than 10% of the total jet energy, since many fake jets with low f_{EM} are identified in this region due to the partial coverage of the calorimeter.
- In order to avoid selecting events where most of the energy associated with a jet could be produced by localised noise, events are rejected if the leading jet has $> 90\%$ of its energy associated with a single constituent cluster or layer within the LAr calorimeter.

The cuts listed above are the same used in the previous version of this analysis [3].

$cDPJ$ reconstruction

The cDPJ reconstruction efficiency can be defined, similarly to the μDPJ, as the ratio of the number of dark-photons decaying in e^+e^- or $q\bar{q}$, which are found in a $\Delta R = 0.4$ cone around a $cDPJ$, and the total number of dark-photons decaying in electron or quark pairs.

The reconstruction efficiency is shown in Figure 5.3 for dark-photons with $|\eta| < 1.1$ as a function of L_{xy} and transverse momentum for several benchmark signal samples. In the case of the efficiency shown as a function of p_T, an additional requirement is applied on the true dark-photon L_{xy} to be between 2 m and 4 m. A γ_d decaying into quarks or electrons is reconstructed only within the HCAL fiducial volume.

5.3 Neural Network taggers for background rejection

The analysis work detailed in this thesis makes use of unconventional signatures, given the exotic nature of a search for long-lived particle decays. This can be an advantage, since the reconstruction of dedicated objects like the displaced dark-photon jets, described in the previous section, enables to remove a large fraction of events, not of interest for

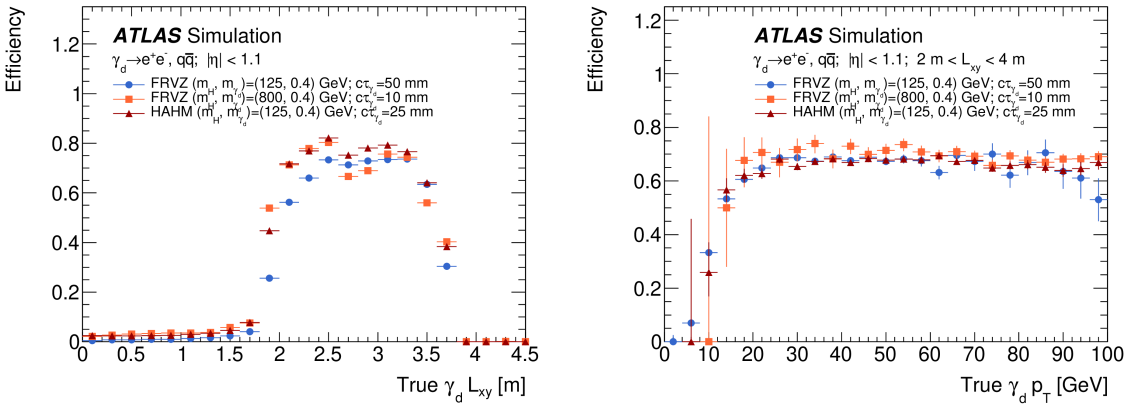

(a) (b)

Figure 5.3: The reconstruction efficiency for cDPJs produced by the decay of γ_d in e^+e^- or $q\bar{q}$. Figure (a) shows the reconstruction efficiency for γ_d with $0 < |\eta| < 1.1$ as function of the transverse decay length L_{xy}. The efficiency drop at 2.5 m corresponds to the end of the first layer of the HCAL. Figure (b) shows the reconstruction efficiency for γ_d with $0 < |\eta| < 1.1$ as function of the transverse momentum, in events where the γ_d L_{xy} is between 2 m and 4 m.

the analysis, collected during the LHC data-taking. However, this has the consequence of bringing into play unusual events which can easily mimic the DPJ signature, originating either from rare multijet events or non-collision background. Those kind of backgrounds, in the vast majority of physics analyses, can be severely suppressed using tight object quality criteria, as the signatures they produce are substantially different with respect to more conventional ones originated from prompt jets or leptons. Those criteria can however reduce significantly the reconstruction efficiency of LLP signatures such as DPJs, which usually rely on looser constraints on reconstructed objects. Therefore dedicated algorithms based on data, referred to as taggers, have been developed by the analysis team in order to estimate the contribution of these backgrounds. The author has contributed to the testing of these taggers but was not involved in the development of the architecture of the neural network based taggers.

5.3.1 The Cosmic-ray muon tagger

Cosmic-ray muons are produced by the shower of highly energetic particles interacting with Earth's atmosphere and are sufficiently penetrating to be able to reach the ATLAS detector cavern, placed more than 100 m underground.

Cosmic-ray muons that cross the detector in time coincidence with a *pp* interaction and produce hits in the muon spectrometer constitute the main source of background to the μDPJ. Moreover, it can also happen that cosmic-ray muons passing through the ATLAS

hadronic calorimeter leave radiative energy deposits that can be reconstructed as cDPJ since those hits are not associated to an ECAL activity nor to tracks in the inner detector.

On the bright side, these muons have a characteristic timing and geometrical pattern, due to the fact that they are originated outside the detector, with timing uncorrelated to LHC collisions and with unusual direction of their momentum. A cosmic-ray enriched dataset, collected during empty bunch crossings, is used to study the characteristics of this background and, for the case of μDPJs, to train a Neural-Network (NN) based tagger, developed in order minimise the contribution from this background. The NN is trained to classify each stand-alone muon spectrometer track constituting a μDPJ based on the following quantities:

- **the longitudinal impact parameter** z_0: the minimum separation in the z-coordinate between the muon track and the primary vertex, measured at the point of closest approach of the muon track to the beam line. Signal muons, despite being displaced, are expected to point to the PV due to the high Lorentz boost, resulting in a distribution peaked around zero. Given the displacement of the dark-photon, no inner detector hits are expected and the correct PV identification relies on initial state radiation jets. Those jets are very likely to originate from the hard scatter vertex, resulting in a correct identification of the PV. On the other hand, cosmic-ray muons do not have a preferred direction along the z-coordinate, resulting in a broad, almost flat, z_0 distribution;

- **timing measurements from the muon spectrometer**: time of the muon track corrected by the time of flight from the interaction point [104]. Looking at the time differences between the RPC middle layer (t_1^*) and RPC outer layer (t_2^*) of the MS, it is possible to identify the direction of flight of the muon (outgoing or incoming), as described in Equation 5.3.1 and schematically shown in Figure 5.4. This variable is important only in the ATLAS north hemisphere, $\phi > 0$, where signal muons and cosmic muons have opposite directions. Two peaks are expected: one for the cosmic-ray muons, at $\sim$ 20 ns (twice the time of flight from the RPC middle layer to the RPC outer layer), and one for the signal muons, peaked at $\sim$ 0 ns. When the timing difference from the outer layer and the pivot layer, which corresponds to the top layer of the RPC middle station of the MS, is zero or not available due to missing hits in one or the other RPC layer, the muon timing is not used by the NN. This is obtained providing a fifth input variable to the NN, whose value is 1 when the timing information should be used, 0 otherwise. The network is trained on a balanced sample of events in which this variable is 0 or 1, avoiding the possibility to learn discriminating features from this variable only;

$$
\begin{aligned}
&T(\text{High Pt}) = t_2^* - t_2^{\text{flight}} \\
&T(\text{Low Pt}) = t_1^* - t_1^{\text{flight}} \\
&\Delta T(\text{High-Low})(\text{for collisions}) = 0 \\
&\Delta T(\text{High-Low})(\text{for cosmics}) = -2(t_2^{\text{flight}} - t_1^{\text{flight}}) = \\
&-2(\text{time of flight})
\end{aligned}
\tag{5.3.1}
$$

- **the track angular direction (η and ϕ)**: cosmic-ray muons are expected to come from the top of the ATLAS detector, resulting in a peaked η distribution and in a double-peak ϕ distribution. Signal muons, on the contrary, are expected to have no preferred direction in the azimuth angle, resulting in a flat distribution and a much less peaked pseudorapidity distribution.

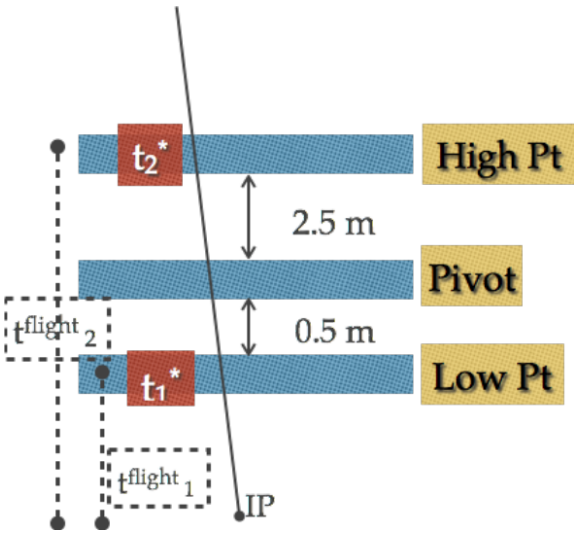

Figure 5.4: Visual scheme of the muon timing variable computation described in Equation 5.3.1. The pivot layer corresponds to the top layer of the RPC middle station of the MS.

The variables described above are shown in Figure 5.5 for standalone muon spectrometer tracks collected respectively in the cosmic-ray dataset and in a benchmark FRVZ signal sample with a dark-photon mass of 0.4 GeV and SM Higgs Boson ($m_H = 125$ GeV).

The neural network that has been developed by the analysis team is a Dense Neural Network (DNN) , implemented using Keras [105] with the Tensorflow backend [106]. Keras is a deep learning Application Programming Interface which enables to build neural networks in a simplified language, using pre-built arrangement of neurons called layers. The tagger is trained as a binary classifier with the purpose of assigning a score close to 1 to muon

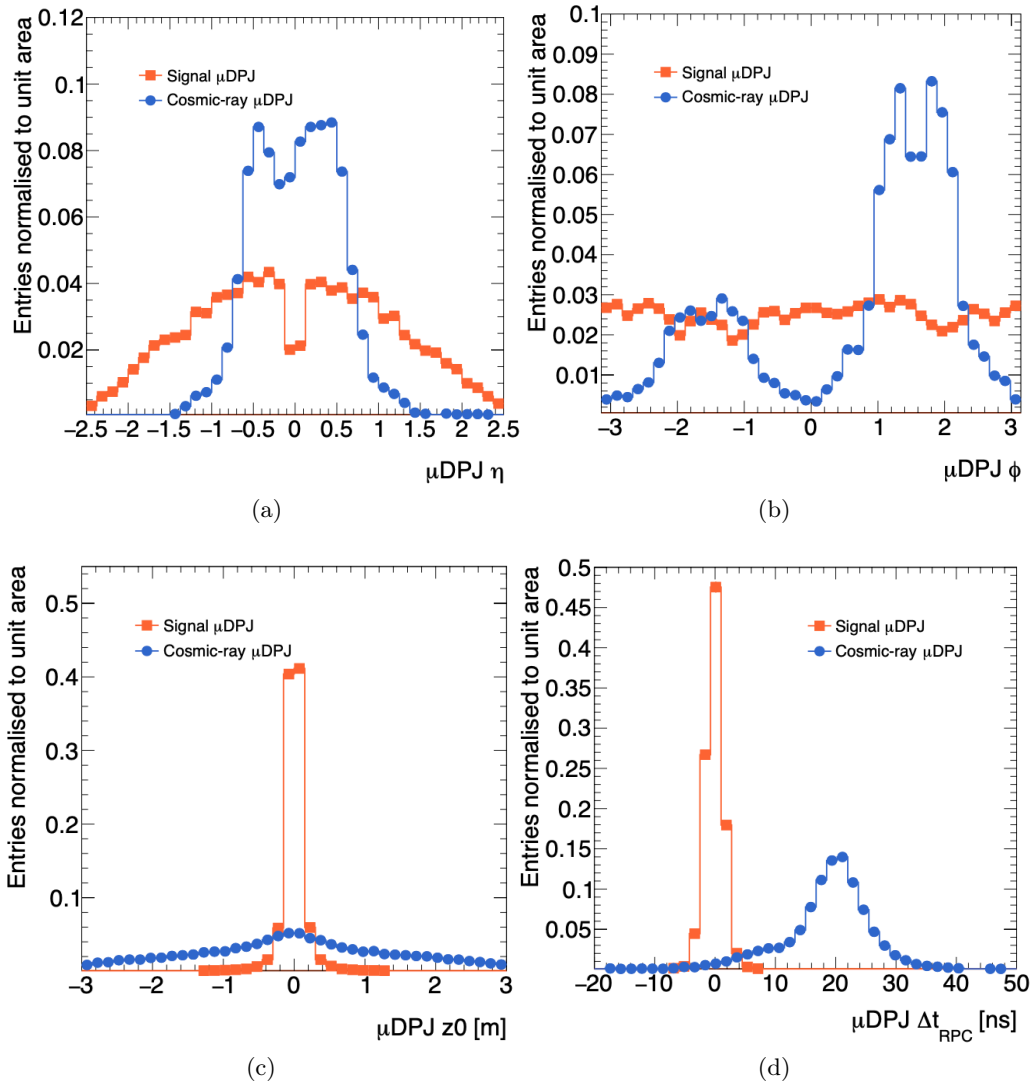

Figure 5.5: Distribution of the variables used to discriminate between muon spectrometer tracks from the cosmic-ray dataset and dark-photon signal events, with reference in this case to a benchmark FRVZ signal sample with a dark-photon mass of 0.4 GeV and SM Higgs Boson ($m_H = 125$ GeV). The η and ϕ coordinates of the tracks are shown in figures (a) and (b), while the impact parameter $z0$ and the RPC timing difference Δt_{RPC} are shown respectively in (c) and (d).

spectrometer tracks which originate from the IP and 0 to the ones produced by cosmic-ray muons. Various configurations were tried, with different number of layers, from two to four, and neurons for each layer, 16 to 128 were tried. The best configuration has been found to be a three dense hidden layers DNN, with 32, 64 and 128 neurons respectively. For an optimal training, a balanced mixture of $\sim$ 90k μDPJs from the cosmic-ray dataset and from MC signal samples, with a dark-photon mass of 0.4 GeV and $m_H = 125$ GeV, is used, where half of the events have been used for validating the training procedure.

Due to the fact that the information on the Δt_{RPC} is not always available, an additional fifth "dummy" variable is fed to the DNN, which has an assigned value of 1 when the timing information is available and 0 otherwise. As stated above, performing the training of the network on a balanced sample of muon tracks in which this variable is 0 or 1, the network learns to use the Δt_{RPC} only when it is available, avoiding the possibility of learning discriminating features based on the additional variable alone.

An output layer with a sigmoidal activation function returns a binary classification score between 0 and 1, which can be interpreted as the probability for a μDPJ's constituent track to originate from a dark-photon decay. This is shown in Figure 5.6 for some benchmark signal scenarios and for data from the cosmic dataset. It can be noticed how the DNN output separates really well the background (dashed green area) from the various signals (coloured lines). In the analysis, a μDPJ is accepted if all its constituents have a cosmic-ray tagger output score greater than 0.5. This selection was optimised to retain a high signal efficiency: signal μDPJs are selected with an efficiency above 95% for transverse decay lengths L_{xy} up to 5 m and for dark-photon p_T down to 20 GeV. In this case, a background rejection of 90% is achieved.

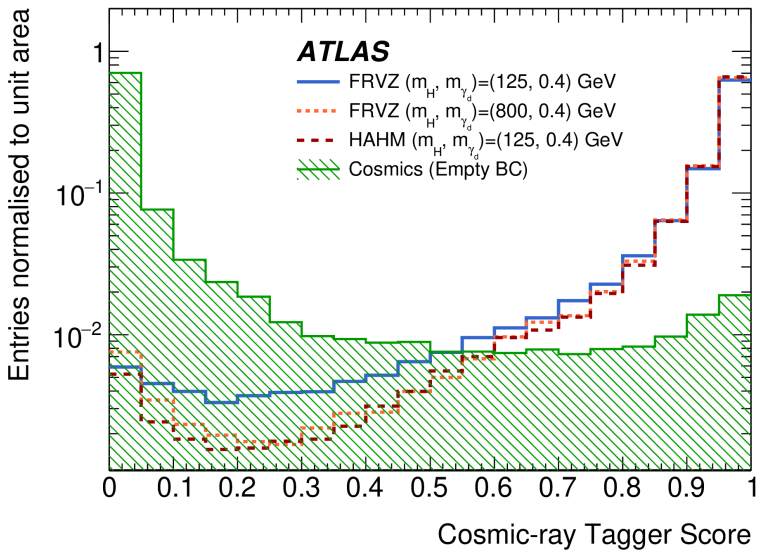

Figure 5.6: The cosmic-ray tagger output score for few signal scenarios and data from the cosmic dataset.

5.3.2 The QCD neural network tagger

SM jets can be misidentified as DPJs. These jets are generated both in multijet events, which represents the main background for the ggF category of the analysis, and in associated production with the W and Z vector boson (V+jet events), representing the main background for the WH category of the analysis.

In the context of this analysis, jets that can be misidentified as DPJs are usually either:

- so-called "punch-through jets", which are jets with such large momentum that the relative hadronic shower can not be entirely contained within the calorimeter. As a consequence, many collimated tracks can be seen in the muon spectrometer, mimicking the typical signature of muonic DPJs;

- jets with a large neutral component which can be a relevant source of fake calorimeter DPJs, since they lead to many mis-reconstructed tracks in the inner detector.

Both multijet and V+jets processes have a production cross-section of several orders of magnitude higher than the signal processes considered. Therefore, even if these jets are rare, they yield a huge amount of background events. The number of misidentified DPJs from rare jets is partially reduced by the selections applied in the definition of μDPJ (see 5.2.1) and cDPJ (see 5.2.2).

The estimate of the residual contributions from these rare events is challenging and, due to the limited MC samples statistics available, a data-driven approach is utilised.

In order to reduce this kind of background, a dedicated per-jet tagger, referred to as QCD tagger, has been developed by the analysis team to discriminate jets originating from displaced dark-photon decays from rare jets. The tagger is based on a Convolutional Neural Network (CNN), implemented as in the case of the Cosmic-ray tagger using Keras, and it assigns a score ranging from 0 to 1 to each reconstructed cDPJ, where a value close to 1 means that the jet is more likely to have been originated in a signal event, and a value close to 0 that it is more likely to come from a background event.

The tagger is built using 3D images and is inspired by the concept of face recognition which has become widely used in artificial intelligence. The concept of jet images has been previously applied in high energy physics in the context of jet tagging [107, 108]. An ATLAS study has also being published [109] about a CNN-based jet tagger, exploiting 2D jet images built from calorimeter clusters.

The QCD tagger developed in the context of this analysis extends the network architecture and concept described in [109], using a 3D representation of jet energy deposits. The addition of a third dimension, allows to better exploit features related to long-lived particles like the unconventional distribution of energy along the depth of the calorimeter. This marks the first time 3D images have been exploited in this search.

Neural network inputs and structure

Ideally, individual calorimeter cells informations could be used to build the jet images, since they provide the most granular information on the energy deposits in the ATLAS calorimeters. However, retaining all the informations relative to the calorimeter cells would be too expensive in terms of disk occupancy and, therefore, only caloclusters are saved, for

which the information on the (η, ϕ) coordinates of its centroid and the fraction of energy associated to it in each calorimeter sampling is available.

The images used as input to the QCD tagger are built dividing the (η, ϕ) space around the jet axis, defined as the direction of its momentum vector, in a 15×15 grid centered in the jet axis and corresponding to a $\eta \times \phi = 0.9 \times 0.9$ area, so that each cell cluster of this 2D grid corresponds to a 0.06×0.06 portion of the (η, ϕ) space. A third axis is then added to take into account the EM and HCAL calorimeters samplings as an additional coordinate. The resulting 3D grids are composed of cell clusters which contain the total energy released in the corresponding (η, ϕ) coordinates and calorimeter sampling. In order to exploit the full calorimeter volume, three 3D grids are produced: one accounting for the barrel samplings, one for the tile extended barrel and one for the endcap.

The 3D grid representing the jet energy deposits are then converted to tensors and sent as input to a convolutional neural network. CNNs are usually based on an initial set of convolution layers, which are helpful in extracting features from the images, followed by a dense neural network which performs the final classification. As mentioned above, the network input consists of three 3D tensors and three blocks of convolutional layers are used. Each block consist in two repetitions of a sequence of layers made of a 3D convolution layer, batch normalisation, leaky ReLu, 3D MaxPooling and Dropout. The outputs of these three blocks of the network are passed to three respective Dense layers with ReLu and then are finally merged together and processed by a dense neural network with a sigmoidal activation function. This results in a classification with output score ranging from 0 to 1. A scheme showing the arrangement of all the layers used for the definition of the QCD tagger is presented in Figure 5.7.

Neural network training and performance

The neural network training is performed using two datasets:

- a signal dataset obtained from reconstructed cDPJs from dark-photon decays. Only the *ggF* FRVZ samples with a 400 MeV dark-photon mass are considered, with an equal number of cDPJ selected, from both the samples where the production is initiated by the SM Higgs boson and the 800 GeV Higgs-like heavy scalar. No trigger has been applied in producing this dataset, in order to retain statistics, and all the simulated events have been considered;

- the background sample is obtained from simulated multijet events. The production of these MC samples is sliced in function of the p_T of the leading parton and the slices used have 60 GeV $< p_T <$ 400 GeV. As for the signal, no trigger requirement has been applied in order to retain statistics.

In order to perform an unbiased validation and avoid overtraining effects on the neural network, the original sample of $\mathcal{O}$(250k) cDPJs, from both signal and background events,

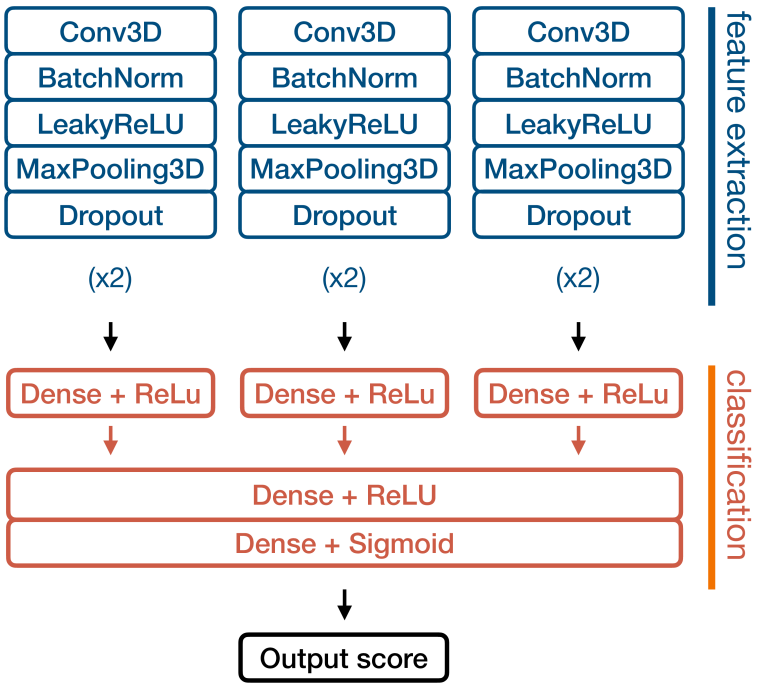

Figure 5.7: Schematic illustration of the layers used for the definition of the QCD tagger. The three convolutional layers at the top receive as inputs the three 3D tensors built from the 3D jet images, then a dense neural network performs the classification step. Three blocks of convolutional layers are used, with each block consisting in two repetitions of a sequence of layers: a 3D convolution layer, batch normalisation, leaky ReLu, 3D MaxPooling and Dropout. The outputs of these three blocks of the network are passed to three respective Dense layers with ReLu activation function, and are subsequently merged together and processed by a dense neural network. The output layer of the network has a sigmoidal activation function which provides a classification with output score ranging from 0 to 1.

was split 75% - 25% in a training and a validation dataset, where the latter is not used at the training step but only for an estimation of the performances of the tagger.

The distribution relative to the output score of the QCD tagger is shown in Figure 5.8a for three different signals with dark-photon mass $m_{\gamma_d} = 400$ MeV, relative to the HAHM model and FRVZ model with either SM Higgs boson and the 800 GeV Higgs-like heavy scalar, compared to multijet background MC events. In Figure 5.8b, the same distribution is shown for the FRVZ model with SM Higgs boson production and different dark-photon masses, compared also in this case to multijet background MC events.

In both cases, a good separation between QCD and signal samples can be seen. To have a glimpse of the network performances, an unoptimised cut applied as example at 0.5 on the output score, considering the signal distribution relative to the FRVZ sample with $m_{\gamma_d} = 400$ MeV and $m_H = 125$ GeV, is found to have a 92% signal efficiency while obtaining a 90% background rejection. This tagger is used for the identification of all the

signal regions of the analysis that include calorimeter DPJs.

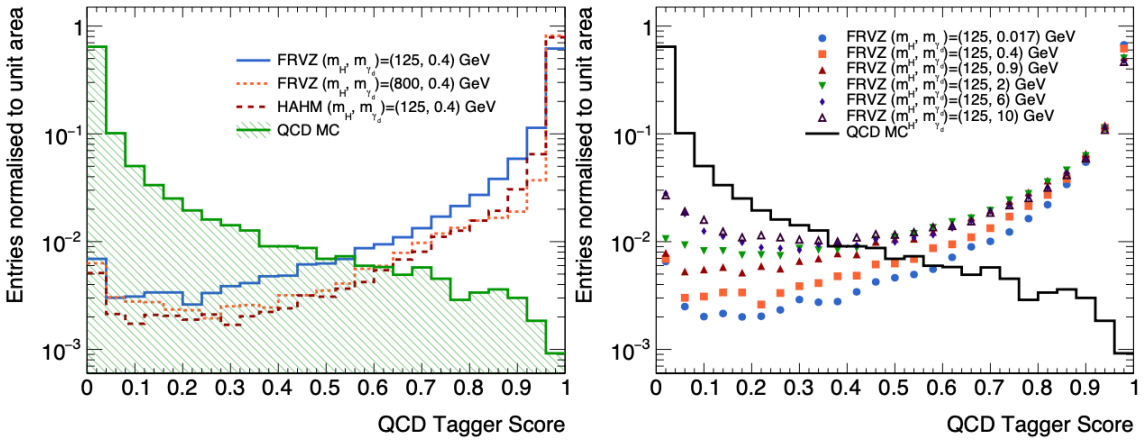

(a) (b)

Figure 5.8: The output score distribution of the QCD tagger is shown for cDPJs from QCD multijet events and different set of signals: in (a) different samples with a dark-photon mass of 0.4 GeV are shown, while the distributions relative to different mass points of the FRVZ model are shown in (b).

5.3.3 The BIB neural network tagger

In the context of the analysis presented in this thesis, a potential source of background arises from high energy muons originating from the hadronic showers induced by beam losses, as described in Section 3.1.1. These muons are mostly unaffected by the shielding and can leave radiative losses in the calorimeter, that can be reconstructed as cDPJs. As mentioned in Section 3.1.1, a dedicated BIB-enriched sample has been collected from ATLAS Run-II collision data, as no MC simulation is available.

BIB events have some peculiar features, which are helpful to reduce their contribution:

- due to the interaction of the BIB muons with the magnetic field generated by the LHC dipoles and quadrupoles, they are either deflected in the $x = 0$, $y = 0$ planes, if they are at a distance $r \leq 1$ m from the interaction region, or in the $y = 0$ plane otherwise. As a consequence, these muons have a characteristic ϕ distribution peaked around $\phi = 0$ and $\pm\pi$, as shown in Figure 5.9 a;

- the timing information relative to hits in the ATLAS sub-detectors are always corrected by a factor that accounts for the expected time of flight from the interaction point. This means that reconstructed objects are expected to have a timing distribution peaked around 0, while a BIB that produces a hit in a given (r,z) position produces a much broader distribution, as shown in Figure 5.9 b.

BIB-induced jet timing distribution features are even more emphasised when looking at a 2D plane of timing versus pseudorapidity, as shown in Figure 5.10 for cDPJs collected

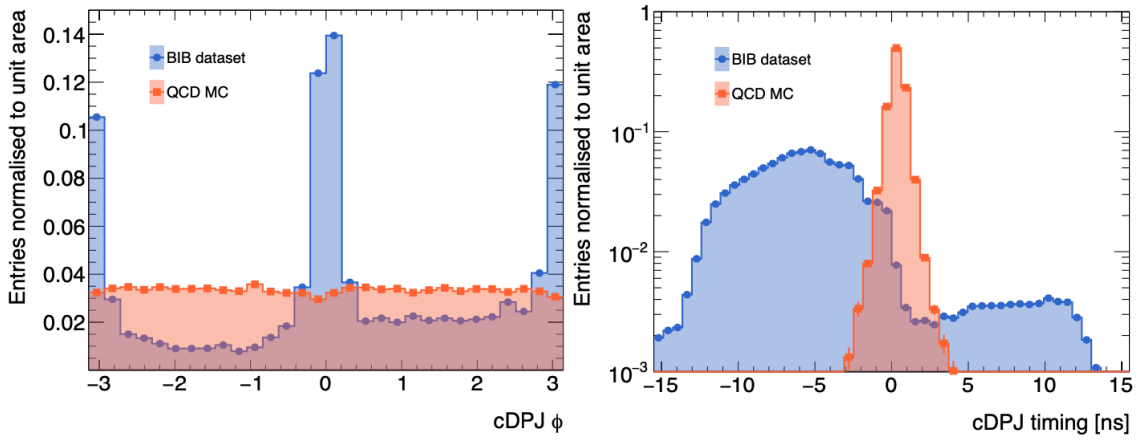

(a) (b)

Figure 5.9: Distributions are shown for two relevant variables variables, comparing cDPJs reconstructed from BIBs and multijet simulated events. The ϕ distribution is shown in (a) with the characteristic peaks around $\phi = 0$ and $\pm\pi$ and the timing of the cDPJ is shown in (b).

in the BIB dataset. In this figure, a residual of jets from collision products is still present and can be seen in the region with $t \sim 0$ and $|\eta| < 1$.

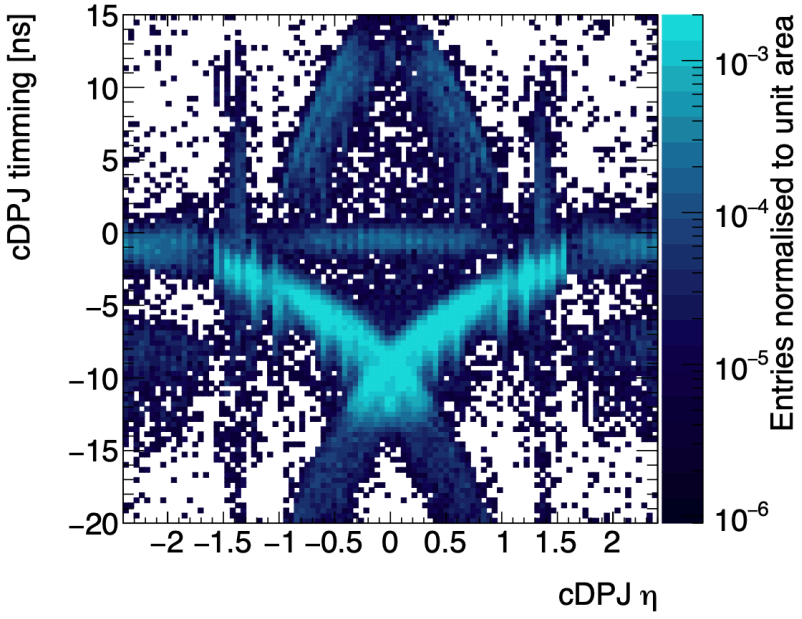

Figure 5.10: 2D plane showing cDPJ timing as a function of the pseudorapidity for cDPJs reconstructed in the BIB dataset.

The aforementioned timing and (η, ϕ) variables, together with BIB calorimetric energy deposit informations, are widely used in ATLAS to discriminate BIB-originated jets from prompt jets, but are not as powerful when having to discriminate BIB jets from signal

cDPJs from dark-photon decays.

In order to enhance the discrimination power between mis-identified cDPJs due to BIB events and signal cDPJs, a dedicated per-jet tagger has been developed, referred to as BIB-tagger, which makes use of the same approach developed for the QCD tagger. Jet images can be helpful to exploit the characteristic hit pattern left by BIB originated jets in the calorimeters to discriminate those jets from the ones originating from the interaction point.

The 3D images are produced with the same procedure used for the QCD tagger, and also the network architecture is identical, with the only addition of passing as inputs to the dense neural network stage also the (η,ϕ) jet coordinates. The training process of this tagger is performed using two datasets, one built using cDPJs reconstructed in the BIB dataset and another one made of cDPJs from dark-photon decays produced by the decay of a heavy Higgs. The choice of using signal events with heavy Higgs production in the training step comes from the fact that SM Higgs signals have a lower efficiency of the CalRatio triggers. Those triggers are applied when collecting the BIB dataset, and are also applied to the signal datasets. This is done in order to avoid a possible bias in the training, caused by the fact that the CalRatio triggers select jets with very low f_{EM}.

The validation of the training is performed separating the initial input dataset of $\mathcal{O}$ (130k) jets in two 75% - 25% samples used respectively for training and validation. The resulting output score distributions of the BIB tagger are shown in Figure 5.11 for BIB cDPJs and for various signal samples, showing that the network performance remains very similar also for the signals not included in the training samples.. In particular, Figure 5.11a shows the distributions for three different signals with dark-photon mass $m_{\gamma_d} = 400$ MeV, relative to the HAHM model and FRVZ model with either SM Higgs boson and the 800 GeV Higgs-like heavy scalar, while Figure 5.11b shows the same distribution for the FRVZ model with SM Higgs production and different dark-photon masses, where in both cases the signal distributions are compared to BIB background events.

From the aforementioned figures it can be seen that a good separation between signal and background is achieved. A selection on the output score of the BIB tagger, applied for instance at 0.5, yields a signal efficiency of 71% and a background rejection of 88%.

5.4 Event selection

In the displaced DPJ analysis, the events are classified into the two exclusive search categories, based on the charged lepton multiplicity and aimed at different production mechanisms of the Higgs bosons from which the dark-photons originate, namely ggF and WH associated productions.

The ggF category targets events with no charged lepton candidates, while in the WH category the presence of exactly one charged lepton is required, expected to originate from the leptonic decay of the W boson ($W^{\pm} \to \ell^{\pm}\nu$).

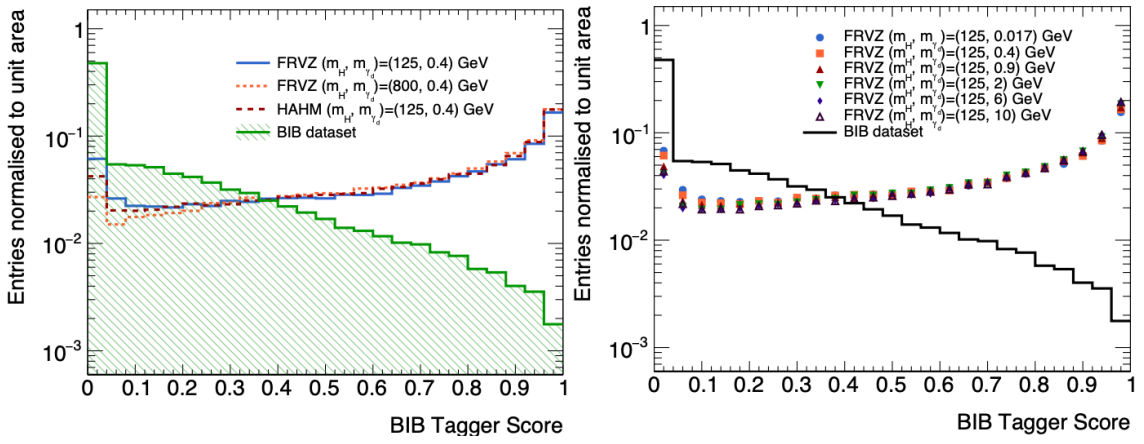

(a) (b)

Figure 5.11: Distributions are shown for the output score distribution of the BIB tagger for cDPJs from BIB jets and different set of signals: in (a) different samples with a dark-photon mass of 0.4 GeV are shown, while the distributions relative to different mass points of the FRVZ model are shown in (b).

In both categories, one or more DPJs reconstructed and selected satisfying the criteria described in Section 5.2 are required in the event. If more than two DPJs are reconstructed, the one with the highest transverse momentum, labelled as leading DPJ, and the one farthest in $\Delta\phi$ from the leading one, labelled as far DPJ, are used to classify the event. Each search category further divides the events into different orthogonal search channels based on the number of μDPJs and cDPJs, yielding a total of six orthogonal signal regions (SRs), three for each category, that were optimised in terms of discovery sensitivity. More details on the event selection used in the two categories and the definition of the corresponding SRs are given in the following sections.

5.4.1 Gluon-gluon fusion production event selection

The event selection for the *ggF* production category, aiming at both SM Higgs boson and the bSM Higgs-like scalar production, is mainly divided in two steps.

To begin with, the events are required to pass a series of requirements referred to as pre-selection:

- first, events must be accepted by one or more of the three dedicated triggers targeting displaced objects, Tri-muon MS-only, CalRatio and Narrow-Scan, described in Section 3.2;
- it is required that all sub-detectors were fully operational and that the event figures in the Good Runs List;
- the presence of at least one primary vertex is required;

- the presence of a prompt muon or electron with $p_T > 27$ GeV in the event is vetoed in order to ensure the orthogonality with the WH category;
- events are rejected if they have $E_T^{miss} > 225$ GeV and two jets with a combined invariant mass larger than 1 TeV. This is done to allow in the future a statistically-independent study of a Vector Boson Fusion production mode category.

Events passing the pre-selection listed above are then required to have two or more reconstructed DPJs and are subject to further requirements depending on the leading and far DPJ types combination and the trigger requirement they have satisfied. This leads to the definition of three different analysis channels for the ggF category:

- $ggF_{2\mu}$: events in this channel must be selected by one of the two displaced muon triggers (Narrow-Scan and Tri-muon MS-only) and both leading and far DPJ have to be of the muonic type;
- ggF_{2c}: events in this channel must be selected by the CalRatio trigger and both leading and far DPJ have to be calorimeter DPJs;
- $ggF_{c+\mu}$: events in this channel must be selected by the Narrow-Scan trigger, with the leading and far DPJ being one of muonic type and the other of the calorimeter type.

In each of these channels, a dedicated set of discriminating variables, listed below, are then used to apply additional selections in order to further mitigate the number of background events entering the relative signal region:

- Cosmic-ray tagger score: the output score of the Cosmic-ray Tagger for each μDPJ found in the event;
- t_{cDPJ}: the measured time associated to a cDPJ in the event;
- $|\Delta t_{\text{cDPJs}}|$: the absolute difference of the times associated with each of the cDPJs in the pair is used in the ggF_{2c} channel to further reduce contributions from cosmic rays and BIBs.
- JVT: the JVT score of a cDPJ that can be used to reject candidates that are likely to originate from the primary proton-proton interaction;
- BIB tagger score: the score assigned to each cDPJ by the BIB tagger;
- $\Delta\phi_{\text{DPJ}}$: the azimuthal angular difference between the leading and far DPJ. Signal events are expected to contain anti-aligned DPJ pairs;
- $\max(\sum p_{\text{T}})$: the maximum value of $\sum_{\Delta R=0.4} p_{\text{T}}$ among the two DPJs, where $\sum_{\Delta R=0.4} p_{\text{T}}$ represents the scalar sum of the transverse momenta of all tracks enclosed within $\Delta R = 0.4$ around the direction of the DPJ momentum vector. Displaced DPJs are expected to cause very limited activity in the volume of the inner detector;

- $\prod$ QCD tagger: the product of the cDPJ tagger scores of the two DPJs, or the single QCD tagger score when only one cDPJ is available.

The selections applied using the above defined variables are summarised in Table 5.1. Each of the cuts presented in the table have been chosen to maximise the signal significance, as defined in [110]. The final estimate of the residual background events entering the signal regions is then performed with a data-driven method, relying on the use of the $\prod$ QCD tagger, $\max(\sum p_{\mathrm{T}})$ and $\Delta\phi_{\mathrm{DPJ}}$ variables, which will be later described in Section 5.5.

Table 5.1: Definition of the SRs used in the *ggF* selection. All SRs require at least two DPJs, but only the leading and the far DPJs are considered for the event classification. Dashes indicate the cases when the respective requirement is not applied. The DPJ cuts presented in the table have been chosen to maximise the signal significance, as defined in [110].

Requirement / Region	$\mathrm{SR}^{\mathrm{ggF}}_{2\mu}$	$\mathrm{SR}^{\mathrm{ggF}}_{2\mathrm{c}}$	$\mathrm{SR}^{\mathrm{ggF}}_{\mathrm{c}+\mu}$
Number of μDPJs	2	0	1
Number of cDPJs	0	2	1
Tri-muon MS-only trigger	yes	-	-
Muon narrow-scan trigger	yes	-	yes
CalRatio trigger	-	yes	-
Cosmic tagger score	< 0.5	-	< 0.5
$\lvert t_{\mathrm{cDPJ}}\rvert$ [ns]	-	< 4	< 4
$\lvert \Delta t_{\mathrm{cDPJs}}\rvert$ [ns]	-	< 2	-
cDPJ JVT	-	< 0.4	-
$\Delta\phi_{\mathrm{DPJ}}$	$> \pi/5$	$> \pi/5$	$> \pi/5$
BIB tagger score	-	> 0.2	> 0.2
$\max(\sum p_{\mathrm{T}})$ [GeV]	< 4.5	< 4.5	< 4.5
$\prod$ QCD tagger	-	> 0.95	> 0.9

5.4.2 WH associated production event selection

The WH category event selection is organised as follows. First, a so-called preselection is applied, consisting of the following requirements:

- events are required to satisfy the trigger requirements of at least one of the single lepton triggers listed in Section 3.2.4. The offline requirements on the p_T, identification and isolation of the lepton are tighter than those applied online, in order to avoid trigger threshold effects and be on the trigger efficiency plateau [111];

- similarly as for the ggF category, it is required that all sub-detectors were fully operational and that the event is included in the Good Runs List; moreover the presence of at least one one primary vertex is required;

- events are rejected if they have $E_T^{miss} > 225$ GeV and two jets with a combined invariant mass larger than 1 TeV. This is done to allow in the future a statistically-independent study of a Vector Boson Fusion production mode category;

- possible contributions from single-top and $t\bar{t}$ processes are reduced by requiring three or fewer jets with $p_T \geq 30$ GeV and vetoing the presence of b-tagged jets (see Section 4.4.2) in the event;

- the presence of exactly one reconstructed prompt muon or electron with $p_T > 27$ GeV is required, with the lepton being of the same flavour as the trigger that accepted the event;

- it is required that no additional prompt muons or electrons with $p_T > 10$ GeV are reconstructed, in order to reduce possible contributions from Z+Jets events;

- events are required to have $E_T^{miss} > 40$ GeV and the transverse mass [1], m_T, computed using the prompt lepton and E_{miss}^T informations, is required to be above 30 GeV. This is done in order to match the signature from the presence of a W boson in the event.

The cuts listed above are aimed at reducing to negligible level all sources of background with the exception of W+Jets events, which are more challenging to tackle and are reduced in further selection steps. After these selections have been applied, the background is totally dominated by W+Jets events, accounting for $\approx 98\%$ of the total background. Moreover, unlike what happens for the case of the ggF category, in the case of the WH category there is no contribution from non-collision backgrounds (i.e. cosmic-ray muons and BIB). This is achieved thanks to the use of prompt object triggers and the other requirements needed for the selection of a leptonically decaying W boson in the event.

Events passing the pre-selection step are then separated into three orthogonal search channels based on the numbers of reconstructed μDPJs and cDPJs and their type combination:

- WH_c: events in this channel are selected requiring the presence of exactly one reconstructed DPJ being of the calorimeter type;

- WH_{2c}: this channel requires the presence of two or more reconstructed DPJs in the event, with both leading and far DPJ being of the calorimeter type;

[1] The transverse mass is defined as $m_T = \sqrt{2p_T^\ell E_T^{miss}(1 - cos\Delta\phi)}$, where $\Delta\phi$ is the azimuthal angle between the vectors defining the missing transverse momentum and the lepton transverse momentum (p_T^ℓ).

- $WH_{c+\mu}$: events in this channel are selected requiring the presence of two or more reconstructed DPJs are, with leading and far DPJ being one of cDPJ and one of the μDPJ type.

It can be noticed that only two out of the three analysis channels in the WH category have the same DPJ type and number combination described in the case of the ggF category. The absence of a purely-muonic DPJ channel is motivated by the fact that, mainly because of the much lower cross-section of the $WH(W^{\pm} \to \ell^{\pm}\nu)$ process with respect to ggF, feasibility studies performed in the initial stage of the analysis have shown this channel would have had a negligible acceptance with respect to the corresponding selection of the ggF category, and therefore it has been not developed further. On the other hand, thanks to the WH production mechanism, and thus the ability to exploit the single lepton triggers, the aim is for the WH analysis category to be sensitive in the hadronic channels and to be competitive with the ggF analysis. Therefore, the WH category focuses only on the channels containing calorimeter DPJs adding with respect to the ggF category a channel with exactly one reconstructed cDPJ (WH_c).

An additional selection is applied to each of the three WH channels, involving a set of discriminating variables, some of which are also used in the ggF channels selection (see Section 5.4.1):

- m_T: a further cut on the transverse mass, in addition to the one applied at pre-selection, can be helpful in reducing possible contributions from V+Jets events;

- t_{cDPJ}: the measured time associated to a cDP in the event;

- JVT: the JVT score of a cDPJ can be used to reject candidates that are likely to originate from the primary proton-proton interaction;

- cDPJ width: the p_T-weighted sum of the $|\Delta R|$ between each energy cluster and the jet axis. Jets from DPJs are expected to be narrower on average than ordinary jets since they are produced just before or inside the calorimeters.

- min($\Delta\phi$): minimum azimuthal angular distance between each DPJ considered in the selection and the $\mathbf{p}_{\mathrm{T}}^{\mathrm{miss}}$ vector.

- min(QCD tagger): the minimum QCD tagger score, computed considering up to two cDPJs.

The selections that have been made in order to define the WH channels signal regions, shown in Table 5.2, are defined to reduce as much as possible the background contributions, and are chosen to maximise the signal significance, as defined in [110]. Events falling in the WH_c channel are required to have $m_T \geq 120$ GeV, since the second dark-photon is expected to decay outside the detector volume and therefore yield a higher E_T^{miss}. In addition, a cut

on cDPJ p_T is also applied in order to further reduce the initially overwhelming W+Jets background, which is in this region significantly higher than in the other two WH channels because of the requirement of having only one reconstructed DPJ.

Table 5.2: Definition of the signal regions used in the WH selection. In signal regions requiring at least two DPJs, only the leading DPJ and the far DPJ are considered for the event classification. Each DPJ SR is exclusive in the number of DPJs in the event. Dashes indicate cases where a requirement is not applied. The DPJ cuts presented in the table have been chosen to maximise the signal significance, as defined in [110].

Requirement / Region	$\mathrm{SR}_{\mathrm{c}}^{\mathrm{WH}}$	$\mathrm{SR}_{\mathrm{2c}}^{\mathrm{WH}}$	$\mathrm{SR}_{\mathrm{c}+\mu}^{\mathrm{WH}}$
Number of μDPJs	0	0	1
Number of cDPJs	1	2	1
Single-lepton trigger (μ, e)	yes	yes	yes
m_{T} [GeV]	> 120	-	-
$\lvert t_{\mathrm{cDPJ}} \rvert$ [ns]	< 4	< 4	< 4
leading (far) cDPJ width	< 0.08	< 0.10 (0.15)	< 0.1
cDPJ p_{T} [GeV]	> 30	-	-
JVT	< 0.6	< 0.6	< 0.6
min($\Delta\phi$)	$< 3\pi/5$	$< 3\pi/10$	$< 7\pi/20$
min(QCD tagger)	> 0.99	> 0.91	> 0.9

The final estimate of the residual W+Jets background events entering the three signal regions is performed, as in the case of the ggF category, with a data-driven method relying, in this case, on the use of the min($\Delta\phi$) and min(QCD tagger) variables. This method is described in detail in the following section.

5.5 Background estimation

The estimation of the residual background events entering the signal regions of the analysis is performed using a fully data-driven technique referred to as ABCD method. This method is used to estimate the background due to multijet events in the ggF category and from W+Jets events in the WH category. In addition, a description of treatment of the non-collision backgrounds is given in Section 5.5.2, which, as previously mentioned, affects only the ggF selection.

5.5.1 The ABCD method

The ABCD method is a simplified matrix method that relies on the assumption that the background events distribution can be factorised in the plane of two uncorrelated variables,

divided in four regions: A, B, C, D. In this plane, the signal region is identified as the region A while, inverting the selections on the two variables, three further control regions can be defined as region B, C, and D. The two variables used can be both continuous observables (e.g. the output score of a neural network tagger), or a discrete binary requirement (e.g. a veto on additional leptons in the event). The only requirement for the ABCD method to work is that the signal is mostly contained in region A, while the background is uniform in the plane defined by the four regions.

Considering the case of two continuous variables, namely x and y, that are used to define the signal region and three control regions, the number of background events in a given region (N_i, with i = A, B, C, D) is proportional to its area and the four regions can be defined as follows:

- Region A (signal region): $x_2 \leq x < x_3 \cap y_1 \leq y < y_2$,
- Region B: $x_2 \leq x < x_3 \cap y_2 \leq y < y_3$,
- Region C: $x_1 \leq x < x_2 \cap y_2 \leq y < y_3$,
- Region D: $x_1 \leq x < x_2 \cap y_1 \leq y < y_2$,

where the number of background events in region A can be evaluated as:

$$N_A = \frac{N_B N_C}{N_D}. \tag{5.5.1}$$

For the above statement to be true, the two variables need to be sufficiently uncorrelated only for background events, hence it does not matter if there is an obvious anti-correlation in the signal distribution. A schematic representation of an ABCD plane, with the four regions defined as described above, is shown in Figure 5.12.

The requirement of having a uniform distribution of the events in the ABCD plane for the background is not strictly necessary for the ABCD method to work, as long as the ratios of events N_C/N_D and N_B/N_A are found to be equal. If this condition is not satisfied, the method should be properly validated taking into account this effect.

The same applies to the assumption that all the events recorded in region B, C, and D, are background events. If we have a non-negligible signal leakage in any of these regions, it is sufficient to have a reliable prediction for the signal strength that can be subtracted in order to take into account the possible effects and that the fraction of signal events is low with respect to the background yields.

In addition, the presence of secondary sources of background in the plane is not an issue. In fact, as long as an estimate of these backgrounds is available, event yields in one or more regions of the plane can be subtracted before computing the expected background for the signal region.

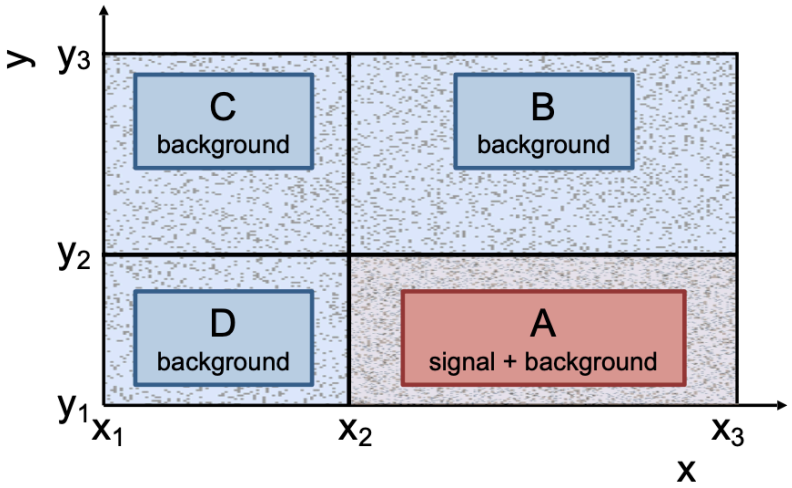

Figure 5.12: Schematic representation of an ABCD plane where background events are distributed uniformly in the plane defined by the two uncorrelated variables x and y, and where the signal is fully contained in region A. The two variables used, need to be sufficiently uncorrelated only for background events and, therefore, it does not matter if there is an obvious anti-correlation in the signal distribution.

Likelihood based ABCD

Instead of applying the standard arithmetic ABCD calculation to obtain a prediction, which corresponds to apply Equation 5.5.1, a likelihood-based approach can be used.

A likelihood-based approach to the ABCD method consists of building a four-bin statistical model taking into account the underlying relationship between the background events in the different regions. This method is more robust against control regions with small number of events and allows to take into account possible small signal contamination in the control regions. The resulting fitted likelihood describes the signal and background expectations in each region, defined by products of Poisson functions, and can be expressed as follows:

$$\mathscr{L}(N_A, N_B, N_C, N_D | s, b, \tau_B, \tau_C) = \prod_{i=A,B,C,D} \frac{e^{-n_i} n_i^{N_i}}{N_i!}, \tag{5.5.2}$$

where N_A, N_B, N_C, N_D, are the number of events observed in each region in data, τ_B and τ_C are the nuisance parameters that hold the arithmetical relation between region A and regions B, C and D, and n_i are linear combinations of the signal and background expectations in each region, taking the following form:

$$\begin{aligned} n_A &= s + b \\ n_B &= s\epsilon_B + b\tau_B \\ n_C &= s\epsilon_C + b\tau_C \\ n_D &= s\epsilon_D + b\tau_B/\tau_C \end{aligned}$$

where s is the signal and b is the background yield in region A. The signal contamination in the region i is described by the coefficient ϵ_i. All the parameter values are allowed to float in the fit to the four data regions.

More generally, a preliminary estimate of the expected number of background events can be performed using the arithmetic approach shown in Equation 5.5.1, but the final results of the background estimation should be extracted by a fit of the statistical model described above.

ABCD planes in the Displaced DPJ analysis

Each of the six orthogonal signal regions are defined in correspondence with an ABCD plane, constructed by either inverting or relaxing the requirements on two variables defining the respective signal region.

Several studies have been made in order to identify the best possible sets of variables to be used. The ones that have been chosen, listed in the following, are the pairs of variables that maximise the signal significance, as defined in [110], in each signal region while satisfying the ABCD method requirements described earlier:

- $\boldsymbol{max \sum p_T}$: displaced DPJs are expected to be highly isolated in the inner detector. This variable is used in all ggF analysis channels to define the control regions B and C, relaxing the cut from 4.5 GeV up to 20 GeV;

- $\boldsymbol{|\Delta\phi_{DPJ}|}$: signal DPJs are expected to be back-to-back in the transverse plane, due to the production mode in the two-body decay of a Higgs boson generated at rest. This variable is used in the definition of the $ggF_{2\mu}$ channel ABCD plane, by inverting the requirements which defines the signal region;

- **QCD tagger**: the tagger output score, which represents the prediction of a DPJ originating from a dark-photon decay, is used in the definition of all signal regions which include cDPJs. In the ggF category channels, the selection is made on the product of the score of all cDPJ considered and the selection defining the signal region is relaxed to define control regions C and D. For the case of the WH category channels, the minimum QCD tagger score, among the cDPJs considered in the event, has been chosen as the variable defining the signal region and, relaxing the requirements, the control regions B, C, D;

- $\boldsymbol{min(\Delta\phi)}$: the angular separation between a DPJ and the missing transverse momentum is expected to be small for events where the WH production mode is considered. The requirement on this variable, used in the definition of all the WH category signal regions, is inverted in the definition of the control regions C and D.

The selections applied to define all the Control Regions (CR) B, C, D are shown in Tables 5.3, 5.4 for the ggF and WH category channels respectively.

Table 5.3: Definition of the control regions used in the ggF ABCD background estimation. All control regions require at least two DPJs, but only the leading and the far DPJs are considered for the event classification. All CR requirements are the same as the respective SR, with the exception of the selections reported in this table.

Requirement / Region	$\mathrm{CRB}_{2\mu}^{\mathrm{ggF}}$	$\mathrm{CRC}_{2\mu}^{\mathrm{ggF}}$	$\mathrm{CRD}_{2\mu}^{\mathrm{ggF}}$
$\Delta\phi_{\mathrm{DPJ}}$	$> \pi/5$	$(0.1, \pi/5]$	$(0.1, \pi/5]$
$\max(\sum p_{\mathrm{T}})$ [GeV]	$[4.5, 20)$	$[4.5, 20)$	< 4.5
Requirement / Region	$\mathrm{CRB}_{2\mathrm{c}}^{\mathrm{ggF}}$	$\mathrm{CRC}_{2\mathrm{c}}^{\mathrm{ggF}}$	$\mathrm{CRD}_{2\mathrm{c}}^{\mathrm{ggF}}$
$\prod$ QCD tagger	> 0.95	$(0.8, 0.95]$	$(0.8, 0.95]$
$\max(\sum p_{\mathrm{T}})$ [GeV]	$[4.5, 20)$	$[4.5, 20)$	< 4.5
Requirement / Region	$\mathrm{CRB}_{\mathrm{c}+\mu}^{\mathrm{ggF}}$	$\mathrm{CRC}_{\mathrm{c}+\mu}^{\mathrm{ggF}}$	$\mathrm{CRD}_{\mathrm{c}+\mu}^{\mathrm{ggF}}$
$\prod$ QCD tagger	> 0.9	$(0.75, 0.9]$	$(0.75, 0.9]$
$\max(\sum p_{\mathrm{T}})$ [GeV]	$[4.5, 20)$	$[4.5, 20)$	< 4.5

Table 5.4: Definition of the control regions used in the WH category ABCD background estimation. The requirements for all regions are the same as those for the respective SRs, except for the selections reported in this table.

Requirement / Region	$\mathrm{CRB}_{\mathrm{c}}^{\mathrm{WH}}$	$\mathrm{CRC}_{\mathrm{c}}^{\mathrm{WH}}$	$\mathrm{CRD}_{\mathrm{c}}^{\mathrm{WH}}$
$\min(\Delta\phi)$	$< 3\pi/5$	$> 3\pi/5$	$> 3\pi/5$
min(QCD tagger)	$[0.9, 0.99)$	$[0.9, 0.99)$	> 0.99
Requirement / Region	$\mathrm{CRB}_{2\mathrm{c}}^{\mathrm{WH}}$	$\mathrm{CRC}_{2\mathrm{c}}^{\mathrm{WH}}$	$\mathrm{CRD}_{2\mathrm{c}}^{\mathrm{WH}}$
$\min(\Delta\phi)$	$< 3\pi/10$	$> 3\pi/10$	$> 3\pi/10$
min(QCD tagger)	$[0.8, 0.91)$	$[0.8, 0.91)$	> 0.91
Requirement / Region	$\mathrm{CRB}_{\mathrm{c}+\mu}^{\mathrm{WH}}$	$\mathrm{CRC}_{\mathrm{c}+\mu}^{\mathrm{WH}}$	$\mathrm{CRD}_{\mathrm{c}+\mu}^{\mathrm{WH}}$
$\min(\Delta\phi)$	$< 7\pi/20$	$> 7\pi/20$	$> 7\pi/20$
min(QCD tagger)	$[0.8, 0.9)$	$[0.8, 0.9)$	> 0.9

The resulting six ABCD planes are presented in Figure 5.13, where per event distributions are shown for benchmark signal samples. It can be noticed that the majority of the events are found to be in the SR as expected, but some non-negligible contaminations appear also in some of the CRs. However, this is not a real issue and results are not affected by the potential signal leakage since the expected signal yields are negligible in comparison

with the SM background contributions in those regions.

More details on the signal yields in the ABCD planes are given in Tables 5.5 and 5.6 for different signal samples, for the ggF and WH category channels respectively. The signal samples yields are calculated normalising the number of events to the full Run-II ATLAS luminosity of 139 fb^{-1}. In the samples where the SM Higgs boson is considered, the relative SM cross-section predicted at $\sqrt{s}$ =13 TeV is used. For what concerns the samples that assume a 800 GeV heavy scalar Higgs, a reference value of $\sigma \times B = 5$ pb is used. More details on the models and the relative theoretical assumptions are given in Chapter 1.

Table 5.5: Signal samples event yields in the ABCD planes of the three different ggF channels for different signal samples using both the FRVZ and the HAHM model. Events are normalised to the integrated luminosity of 139 fb^{-1} and the quoted errors are statistical only. For each channel, region A corresponds to the signal region and cells denoted with a dash correspond to zero predicted events with the available MC statistics.

Model		FRVZ	FRVZ	FRVZ	FRVZ
Process		$H \to 2\gamma_\text{d} + X$	$H \to 2\gamma_\text{d} + X$	$H \to 2\gamma_\text{d} + X$	$H \to 2\gamma_\text{d}$
m_H [GeV]		125	125	800	125
m_{γ_d} [GeV]		0.1	0.4	0.4	0.4
$c\tau_{\gamma_d}$ [mm]		15	50	10	25
$\sigma \times B$ [pb]		4.86	4.86	5	4.86
Selection	Region				
$ggF_{2\mu}$	A	7.2 ± 3.5	5000 ± 90	7960 ± 189	10830 ± 160
	B	-	126 ± 15	207 ± 29	292 ± 28
	C	-	1.8 ± 1.8	-	5 ± 4
	D	-	91 ± 12	30 ± 11	203 ± 23
$ggF_{c+\mu}$	A	92 ± 13	1040 ± 40	5430 ± 150	5970 ± 120
	B	1.7 ± 1.7	77 ± 11	350 ± 40	395 ± 32
	C	3.6 ± 2.5	10 ± 4	42 ± 13	36 ± 9
	D	10 ± 4	95 ± 13	320 ± 40	407 ± 30
ggF_{2c}	A	282 ± 23	102 ± 13	1460 ± 80	850 ± 50
	B	-	3.8 ± 2.7	86 ± 18	31 ± 8
	C	1.7 ± 1.7	-	19 ± 9	1.8 ± 1.8
	D	113 ± 15	29 ± 8	182 ± 26	123 ± 16

Table 5.6: Signal samples event yields in the ABCD planes of the three different WH category channels for different FRVZ signal samples. Events are normalised to the integrated luminosity of 139 fb^{-1} and the quoted errors are statistical only. For each channel, region A corresponds to the signal region and cells denoted with a dash correspond to zero predicted events with the available MC statistics.

Model		FRVZ	FRVZ	FRVZ	FRVZ
Process		$H \to 2\gamma_\text{d} + X$	$H \to 2\gamma_\text{d} + X$	$H \to 2\gamma_\text{d} + X$	$H \to 2\gamma_\text{d} + X$
m_H [GeV]		125	125	125	125
m_{γ_d} [GeV]		0.1	0.4	6	15
$c\tau_{\gamma_d}$ [mm]		15	50	600	1000
$\sigma \times B$ [pb]		0.046	0.046	0.046	0.046
Selection	Region				
WH_c	A	16.94 ± 0.39	8.27 ± 0.28	7.83 ± 0.27	6.35 ± 0.24
	B	12.03 ± 0.33	6.53 ± 0.25	8.17 ± 0.27	6.20 ± 0.25
	C	8.09 ± 0.27	3.77 ± 0.18	4.36 ± 0.20	2.04 ± 0.14
	D	7.86 ± 0.27	3.53 ± 0.18	3.33 ± 0.17	1.83 ± 0.13
$WH_{c+\mu}$	A	2.98 ± 0.17	1.25 ± 0.11	1.03 ± 0.09	0.48 ± 0.06
	B	0.78 ± 0.09	0.25 ± 0.05	0.34 ± 0.05	0.22 ± 0.04
	C	0.43 ± 0.06	0.30 ± 0.05	0.22 ± 0.04	0.44 ± 0.08
	D	2.44 ± 0.15	0.91 ± 0.09	1.18 ± 0.10	0.97 ± 0.10
WH_{2c}	A	1.34 ± 0.11	7.83 ± 0.27	2.33 ± 0.15	0.62 ± 0.08
	B	0.12 ± 0.03	0.54 ± 0.08	0.27 ± 0.05	0.07 ± 0.03
	C	0.01 ± 0.01	0.22 ± 0.04	0.10 ± 0.03	0.02 ± 0.01
	D	0.39 ± 0.07	3.06 ± 0.17	1.23 ± 0.11	0.49 ± 0.07

5.5.2 Non collision background contamination in ABCD planes

The ABCD planes defined in the previous sections can still be affected, only in the case of the ggF signal regions, by a potential contamination due to the presence of non-collision background events. This section focuses on how these additional backgrounds are evaluated.

Beam-Induced Background treatment

As already discussed in Section 5.3.3, BIB events are particularly relevant as a source of fake cDPJs and therefore the studies on a possible BIB contamination are carried focusing on the ggF_{2c} channel, which is the only one where the events are collected by the CalRatio trigger and where the BIB contamination is concerning. Two datasets have been collected

during the Run-II data-taking in order to perform these studies: a BIB-enhanced selection and an unpaired bunch crossings BIB selection, with the main difference that the former dataset is collected during colliding bunch crossings and, therefore, the presence of collision products is also expected, while the latter is obtained in unpaired isolated bunch crossings.

In the ggF_{2c} selection there are several requirements which are helpful in rejecting BIB events. The most effective ones are the requirement on the BIB tagger score (see Figure 5.14), the one on the cDPJ timing and the one on $\Delta\phi_{DPJ}$ (see Figure 5.15). In those figures, the distributions relative to different signal samples are compared to the BIB-enhanced dataset one. This dataset represents a subset of events that are way more contaminated by this background with respect to the main analysis selection running on full Run-II data. In order to further underline the effectiveness of the selection requirements against BIB events, Figure 5.16 is presented. In this image, the 2D distributions of the cDPJ η and timing are shown at different steps of the selection. It can be noticed that features related to the presence of BIB events disappear once the requirements targeting this background are applied. As a final cross-check, the unpaired bunch crossings BIB dataset has been used as input of the ggF_{2c} selection. Since in this dataset no collisions are expected, the CalRatio trigger can easily trigger the signature left by a BIB muon, but still the full selection on this dataset yields zero events entering the ABCD plane.

In conclusion, the BIB background is considered negligible once all the cuts of the analysis are applied and no anomalies in the ABCD plane are seen, indicating that if a residual BIB contamination is present in the plane, this will be distributed exactly as the multijet background, and thus not affecting the background estimation.

Cosmic-ray background

The cosmic-ray background, as already mentioned in Section 5.3.1, can contribute as a possible source of fake μDPJs and a dedicated dataset has been collected in empty bunch crossings using the same triggers active during the collision data-taking, as stated in Section 3.1.1. In the ggF category a small number of events pass the various selection cuts entering the ABCD planes. These events are subtracted from the events in the ABCD planes.

One thing to take into consideration when estimating the cosmic-ray background contribution is that during LHC runs there are very few empty bunch crossings with respect to paired ones. Therefore, the number of events in the cosmic dataset has to be scaled up to the expected one in pp collisions in order to take into account for this difference. This is done applying to these events a multiplicative weight, calculated using the ratio of the number of filled to empty bunch crossings. These scale factors are computed separately for events selected by the Tri-muon MS-only and the CalRatio trigger, as no event was entering the signal regions when selected by the Narrow-Scan trigger in empty bunch crossings, as reported in Table 3.1.

The corrected number of observed events entering the ggF ABCDs is presented in Table 5.7. Only few events enter the ABCD regions and the yield corresponds to a sub-percent contribution in the number of events of each affected region. All contributions are in regions A and D of the planes. This is expected since in empty bunch crossings, a very low inner detector activity is expected, yielding a $\max(\sum p_{\mathrm{T}}) \approx 0$ for all these events. In conclusion, as mentioned earlier, these events are subtracted from the ABCD planes computed using the Run-II dataset for the final background estimation.

Table 5.7: Table showing the observed yields in the ggF signal regions, when running on empty bunch crossings, corrected by the scale factors shown in Table 3.1. The dash indicates that no event was found in the corresponding region.

2015-2018	Empty bunch crossings			
	A	B	C	D
$ggF_{2\mu}$	7 ± 5	-	-	-
$ggF_{c+\mu}$	-	-	-	-
ggF_{2c}	7 ± 4	-	-	14 ± 7

5.5.3 ABCD method validation

Before the analysis selection is processed on the full Run-II dataset, extensive validations of the background estimation method are performed.

Throughout all the analysis stages, before the approach for the background estimation is validated, the aim is to remain as unbiased as possible when designing the analysis strategy. This is achieved by applying a so-called "blinding procedure", which is widely used in particle physics, and consists in not counting nor processing the events falling in the analysis signal region in order to avoid a possible bias in the selection. As a consequence, the ABCD method has to be validated without "unblinding" the signal region.

The ABCD validation procedure aims at verifying that the relation between the four regions defined by Equation 5.5.1 holds. The process starts by defining a second A'B'C'D' plane identified within the area of the control regions B, C and D; this second plane is then subsequently divided in four regions where the ABCD hypothesis is tested. This validation procedure is adopted since it allows to test the method in the regions close to the signal region, without unblinding it, and allows also to directly test the variables used for the final background estimation.

The aforementioned approach has been applied to each of the ggF and WH analysis channels; some examples of the multiple sub-regions that have been used are shown in Figures 5.17 and 5.18, respectively, for ggF and WH channels ABCDs. Focusing for instance on Figure 5.18 a, it can be seen how the closure tests of the ABCD planes are

performed. First, a sub-plane is built from control regions B and C, made of the four sub-regions BC1, BC2, BC3 and BC4, with the boundaries set by the two variables, min(QCD tagger) and min($\Delta\phi$), used in the ABCD plane. Second, as shown in Figure 5.18 b, the boundaries of the variables are moved in the whole range of the plane and, for each instance, the

number of expected events in region BC1 is calculated according to Equation 5.5.1 and then compared to the observed one. The process of moving the plane boundaries on each variables is referred to as "sliding windows" and allows to test the relation between the regions of the plane in an extensive way, ensuring that the ABCD closure holds.

This procedure is repeated for all ABCD planes sub-regions, in all the ggF and WH analysis channels, and a good agreement is found, within the error, between the expected and observed number of events. In addition, in all these sub-regions, the linear correlation factor between the variables defining the ABCD plane has been extracted in order to check that they remain as uncorrelated as possible, and was found to be less than 3% for the ggF channels and less than 2% for the WH ones.

All the validations and checks performed confirms that the ABCD plane closure holds and that the relation between the plane variables ensure they are still reasonably uncorrelated. Therefore, the background estimation method is validated and can be used for the final estimate, as described in the next chapter.

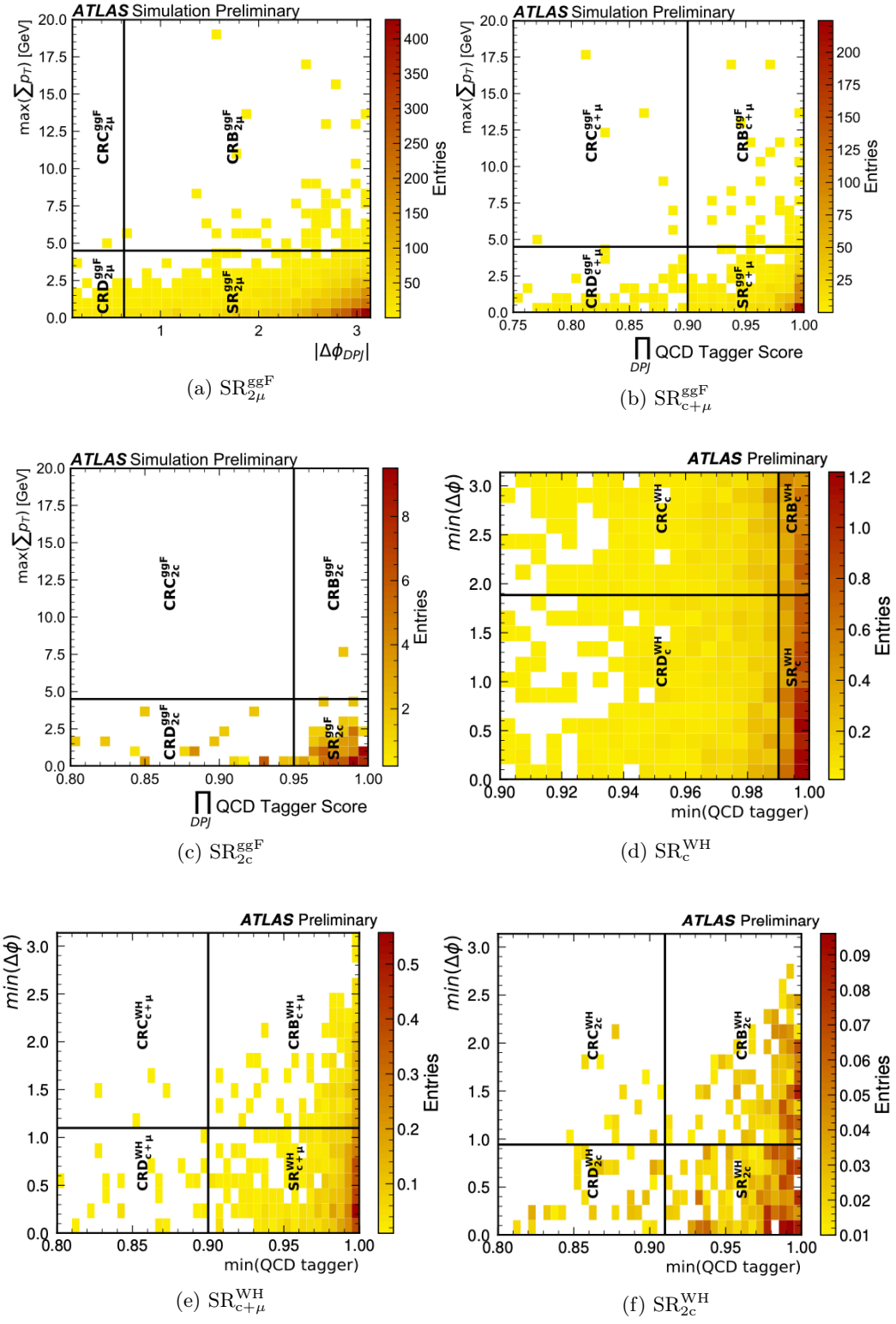

(a) $\mathrm{SR}^{\mathrm{ggF}}_{2\mu}$ (b) $\mathrm{SR}^{\mathrm{ggF}}_{\mathrm{c}+\mu}$

(c) $\mathrm{SR}^{\mathrm{ggF}}_{2\mathrm{c}}$ (d) $\mathrm{SR}^{\mathrm{WH}}_{\mathrm{c}}$

(e) $\mathrm{SR}^{\mathrm{WH}}_{\mathrm{c}+\mu}$ (f) $\mathrm{SR}^{\mathrm{WH}}_{2\mathrm{c}}$

Figure 5.13: The figure shows the per-event distribution for the six different search channels ABCD planes. Figures (a, b, c) show the distribution for benchmark signal samples with the ggF production of a SM Higgs boson. Figures (d, e ,f) show instead the event distribution for WH signal samples. In both cases, the samples used involves the production of a SM Higgs boson decaying in 2 dark-photons + X is considered. The pairs of variables that define each of the ABCD planes shown above, have been chosen in order to maximise the signal significance, as defined in [110], in each signal region. In addition, they need also to satisfy the ABCD method requirements described in 5.5.1, i.e low correlation between the variables and negligible signal leakage with the respect to the respective background

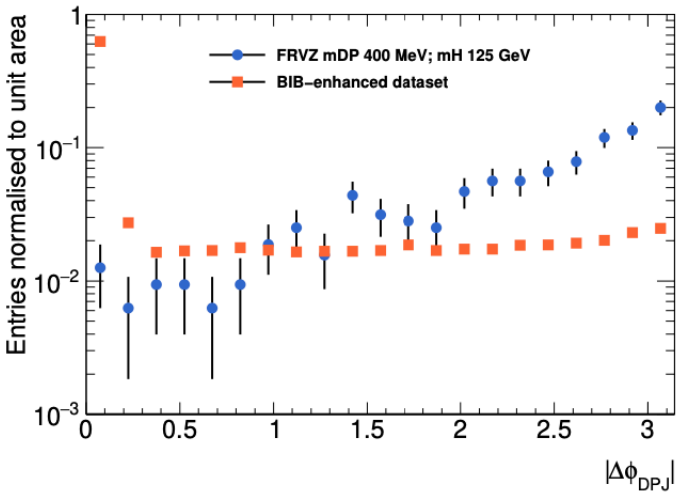

Figure 5.14: Normalised distributions of the $\Delta\phi_{DPJ}$ variable shown for events in the BIB-enhanced dataset and in different signal samples. It can be noticed how a cut at high angular separation between the DPJs in the event is helpful in rejecting the background.

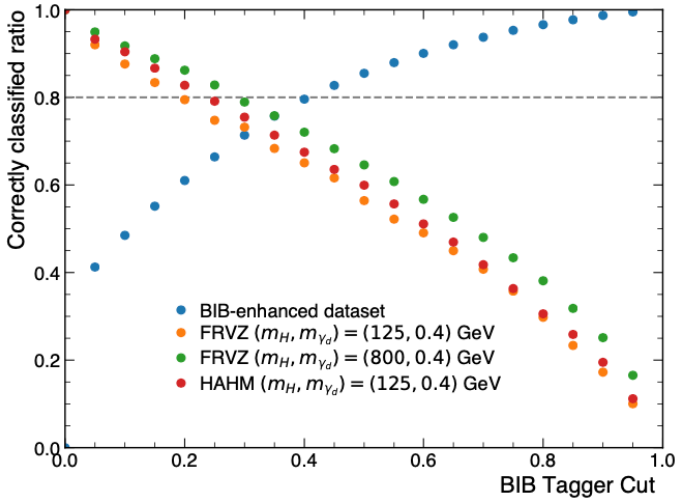

Figure 5.15: Distribution of the BIB tagger score cut efficiency for events in the BIB-enhanced dataset and in different signal samples. The dashed line represents the choice in the analysis on keeping a signal acceptance of 80%.

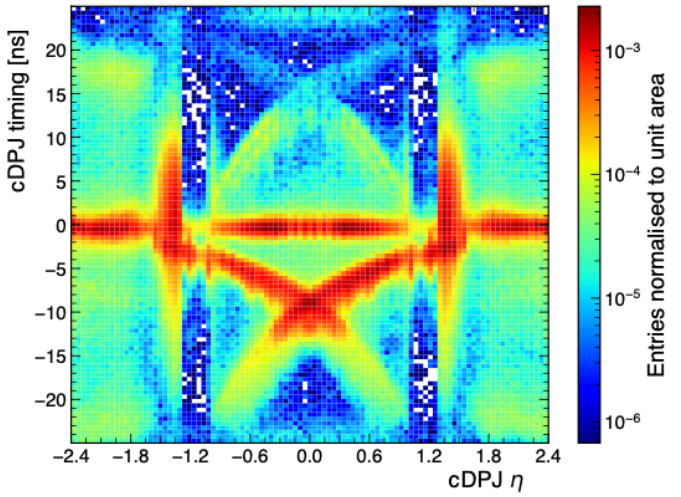

(a)

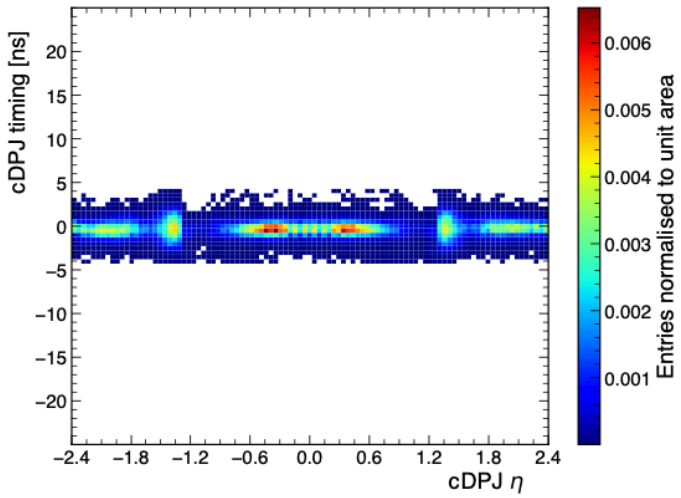

(b)

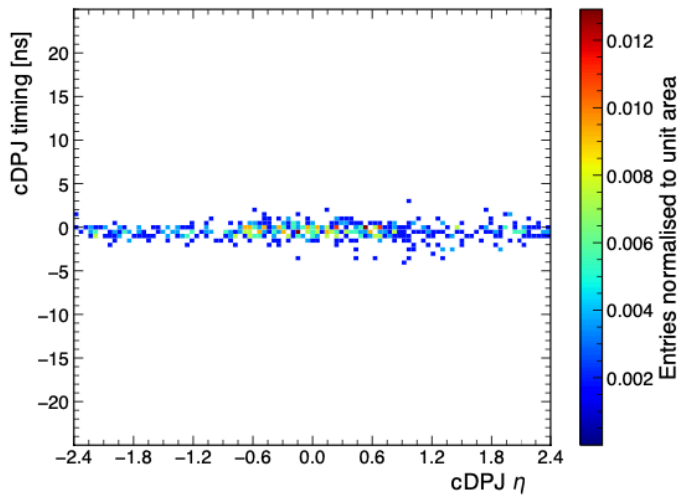

(c)

Figure 5.16: 2D distributions of the cDPJs timing vs η in the BIB-enhanced sample. (a) shows events entering the ggF_{2c} channel, while (b) shows the events after the timing and BIB tagger cuts. Finally, events entering the ABCD plane are visible in (c), for which no pattern with the characteristic of events originating from BIB is observed.

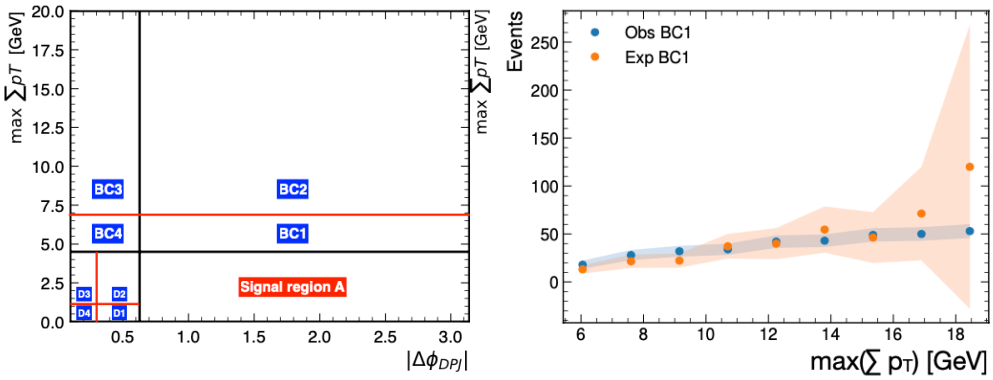

(a) $SR_{2\mu}^{ggF}$ (b) $SR_{2\mu}^{ggF}$

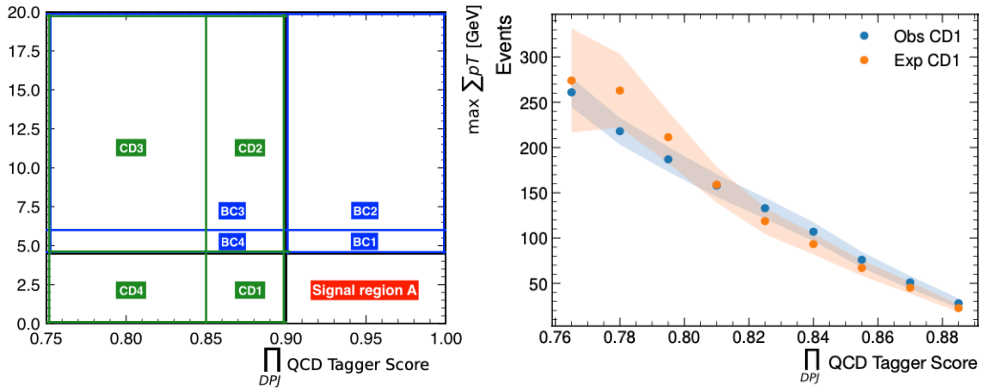

(c) $SR_{c+\mu}^{ggF}$ (d) $SR_{c+\mu}^{ggF}$

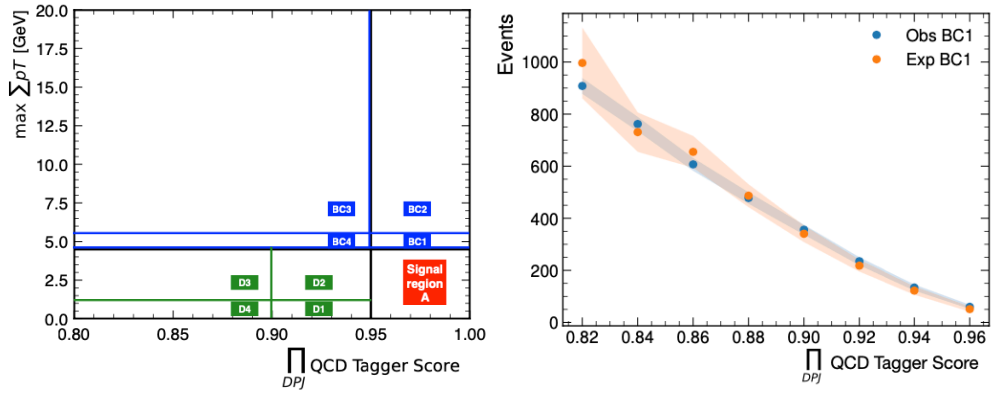

(e) SR_{2c}^{ggF} (f) SR_{2c}^{ggF}

Figure 5.17: The figure shows in (a, c, e) some of the possible subdivisions of control regions B, C and D for the *ggF* category channels ABCD validation, while in (b, d, f) the relative tests of the ABCD hypothesis are reported, for different values of the boundary that divides the sub-regions of figure (a, c, e). In (b, d, f) the expected number of events in each sub-region obtained from the ABCD method, together with the propagated errors according to Equation 5.5.1, is shown by the red band, while the blue band shows the corresponding number of observed events, together with its statistical error.

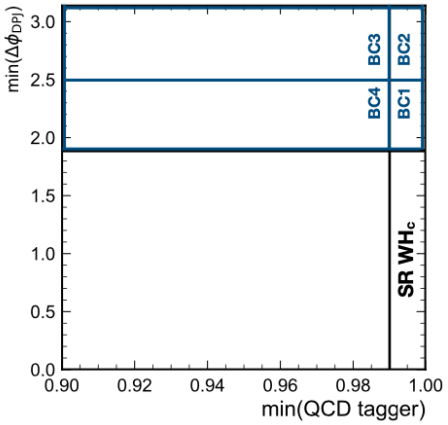

(a) SR_c^{WH}

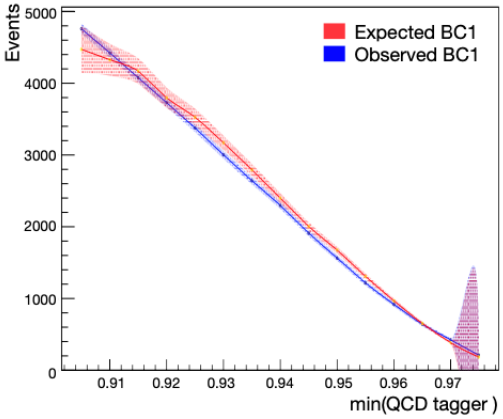

(b) SR_c^{WH}

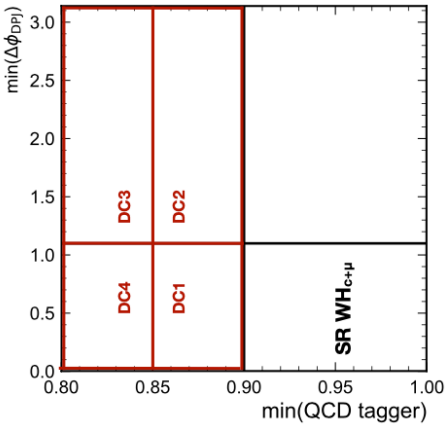

(c) $SR_{c+\mu}^{WH}$

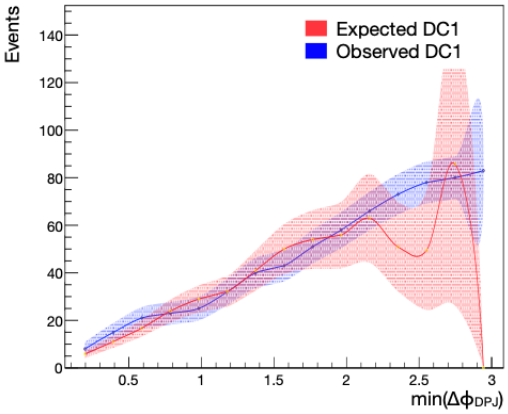

(d) $SR_{c+\mu}^{WH}$

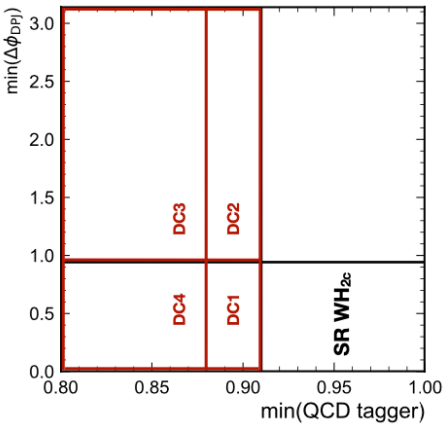

(e) SR_{2c}^{WH}

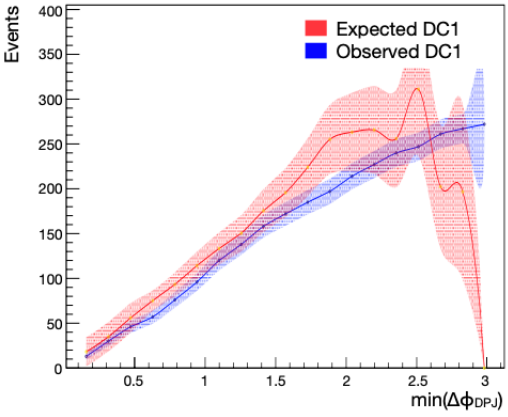

(f) SR_{2c}^{WH}

Figure 5.18: The figure shows in (a, c, e) some of the possible subdivisions of control regions B, C and D for the WH category channels ABCD validation, while in (b, d, f) the relative tests of the ABCD hypothesis are reported, for different values of the boundary that divides the sub-regions of figure (a, c, e). In (b, d, f) the expected number of events in each sub-region obtained from the ABCD method, together with the propagated errors according to Equation 5.5.1, is shown by the red band, while the blue band shows the corresponding number of observed events, together with its statistical error.

Chapter 6

Results and interpretations

In this chapter, the results and the methods used to statistically interpret the data in terms of new physics contributions from the displaced dark-photon jets analysis are described. First, an overview of the estimate of the various systematic uncertainties is presented in Section 6.1. The ABCD method final background estimate and the observed unblinded results are then reported in Section 6.2. In Section 6.3, details are given about the likelihood fitting procedure, already introduced in Section 5.5.1, followed by a description of the procedure used to set limits on the new physics models of interest. Finally, in Section 6.4, details are given about the comparison between the results obtained from the work presented in this thesis and other state-of-the-art results in the context of vector-portal model exclusions.

6.1 Systematic uncertainties

In the analysis presented in this thesis, the overall uncertainty in the signal region is dominated by the statistical uncertainty of the B, C and D regions of the ABCD plane. However, potential sources of systematic uncertainty are considered, having an impact either on the background estimates or the Monte Carlo signal yields. In this section, an overview of the different sources of systematic uncertainty is presented.

Background estimation

As already mentioned in Section 5.5, the background estimation method used in the analysis is fully data-driven. Therefore, the only corresponding source of uncertainty is the one related to the ABCD method itself, which is obtained propagating the statistical uncertainties of the observed yields in regions B, C, and D, to the background expectation obtained from the ABCD method. An additional uncertainty is assigned to account for the size of the cosmic dataset and the computed trigger scale factors. This uncertainty is estimated to be as large as 80% of the expected cosmic-ray muon background. However, the relative

contribution yields a negligible effect on the overall background uncertainty.

6.1.1 Experimental uncertainties

All the remaining sources of uncertainties considered, described in the following, only affects the MC signal events yields. These uncertainties are mainly caused by differences between data and simulation, observed in the object reconstruction or in the pile-up modelling.

Jet uncertainties

Systematic uncertainties related to the reconstruction and energy calibration of all jets reconstructed in ATLAS are considered. These uncertainties are derived from sources such as the differences of jet response between data and MC, pile-up effects, the dependence of the jet characteristics on the flavour of the jets, etc. All the different sources are translated to a set of nuisance parameter that can be applied separately in order to evaluate the corresponding uncertainty. Those parameters are centrally provided by the ATLAS collaboration. In order to correctly apply those uncertainties, the variation by one standard deviation, of one parameter at a time is applied and propagated to the signal yields. The resulting difference in terms of the expected number of signal events, with respect to the nominal case, is then evaluated for each nuisance parameter variation, and the largest is taken as systematic uncertainty. The impact on signal yields is found to be up to a maximum of 3%.

A further uncertainty on the jet energy scale is considered, specific for this analysis. This is needed since jets identified as calorimeter DPJs are required to have a low f_{EM} and therefore are selected with looser working points with regards to the jet cleaning. This uncertainty is derived by comparing the jet momentum in data and MC dijet events as a function of the jet pseudorapidity and f_{EM}. The comparison is then used to scale the events in signal MC samples, taking the corresponding yield difference in the signal region as a systematic uncertainty. This is evaluated to have an effect of $\sim 3\%$ across multiple signal samples.

Muon reconstruction uncertainties

A systematic uncertainty is associated to the reconstruction of close-by muons using only information from the muon spectrometer and evaluated using a tag-and-probe method applied to $J/\Psi \to \mu\mu$ events in data and MC simulation. $J/\Psi \to \mu\mu$ decays are used since this decay process shows similar topology and kinematics to the dark-photon decays in simulated events.

The selection of J/Ψ events follows the following requirements. First, a combined muon with $p_T > 4$ GeV, reconstructed in the acceptance of the inner detector, is required. This muon needs also to fire a J/Ψ trigger and, in addition, a matching is performed between the

triggered object and the reconstructed muon. If the matching requirement is fulfilled, the combined muon is used as tag. All reconstructed muons, with opposite charge to the tag, are then selected and the invariant mass with the tag muon is computed. Among those, the one yielding the invariant mass closest to the J/Ψ one (3.1 GeV) is chosen as the probe. At this point, the last step is to perform a matching between the probe and a stand-alone muon spectrometer track.

The J/Ψ reconstruction efficiency was evaluated, in both MC and in the full Run-II dataset, as a function of the opening angle ΔR between the two muons, as shown in Figure 6.1. As expected, the reconstruction efficiency decreases from higher to lower ΔR values, due to the muon spectrometer limitations in reconstructing tracks with small angular separation. The discrepancy observed between data and MC is the largest in the first ΔR bin, $0.02 < \Delta R < 0.08$. This corresponds to the ΔR bin where the largest contribution from the signal is expected. The discrepancy between to two values in this bin is found to be 9.6% and is taken as a systematic uncertainty.

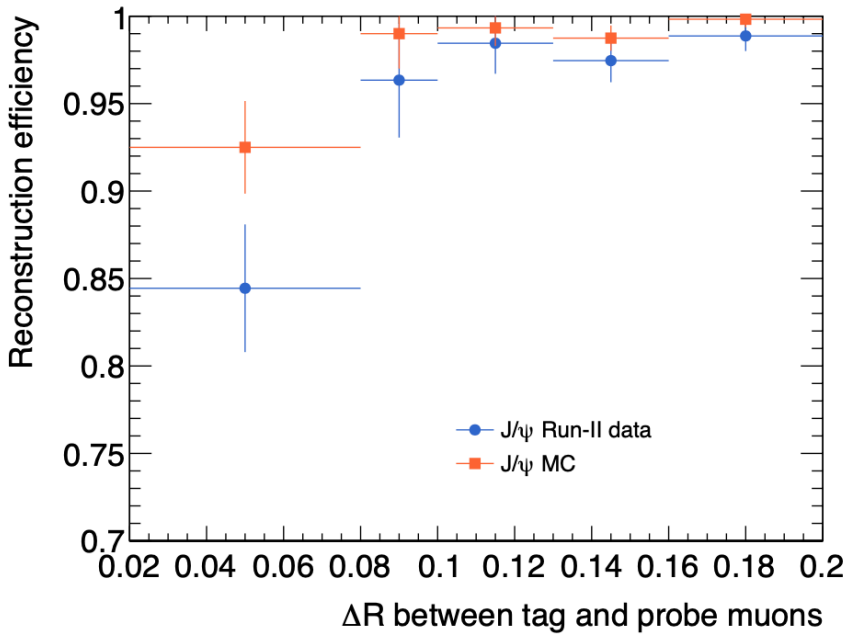

Figure 6.1: The figure shows the reconstruction efficiency of close-by muons, evaluated using the tag-and-probe method, as a function of the opening angle between the two muons in the decay of a J/Ψ for data and MC samples.

Trigger uncertainties

The uncertainties associated to the dedicated triggers, used in the identification of dark-photon decays, have been studied and are presented in the following. Those uncertainties only apply to the ggF side of the analysis and do not represent part of the author's contribution to the analysis.

For what concerns the Narrow-Scan and the Tri-muon MS-only triggers, the corresponding HLT algorithms used have not changed since the start of Run-I. Therefore, the values calculated in [3] have been re-used. Possible effects due to pile-up increase in Run-II with respect to Run-I have been checked and are found to be compatible within the statistical uncertainty. The approach used to calculate these uncertainties is the same used for the close-by muon reconstruction. In this case, the difference between the trigger efficiency calculated in $J/\Psi \to \mu\mu$ events in data and MC simulation is evaluated as a function of the opening angle between the two muons and the resulting uncertainty is found to be 6% for the Narrow-scan trigger and 5.8% for the Tri-muon MS-only trigger.

For what concerns the CalRatio trigger, a different method has been used. The modelling of the variables involved in the HLT algorithm, namely the jet E_T, f_{EM} and p_T, is studied in order to evaluate the uncertainty on the efficiency of the HLT algorithm. Studies on this matter have been performed in Ref [112] and the scale factors obtained are re-used and recomputed for each signal sample. This uncertainty has been evaluated to be the dominant one for the ggF_{2c} channel, which is the only one making use of this trigger, where its estimated value is up to 4% for the heavy (800 GeV) scalar-mediator signal samples, and ranges between 15% and 26% for the 125 GeV Higgs signal samples. The highest values are found to be corresponding to the signal scenarios for which this trigger achieves the lowest efficiency.

Neural network based taggers uncertainties

Another source of uncertainty which needs to be taken into account is the one associated with the modelling of the input variables of the neural network taggers. Those uncertainties are mainly due to potential differences in the network response on real data and MC simulated events. Also in this case, the effect of the uncertainties is only relevant for the signal, since the SM background is estimated from data.

For all the three taggers involved, the same strategy is adopted. To begin with, a binned data/MC ratio of the network output score is produced by classifying objects in a reference sample. The values of these ratios are then used as a binned scale factor to be applied to signal events as a per-event weight. Finally, the signal yields obtained applying this procedure are compared to the nominal ones and the difference is taken as a systematic uncertainty.

The data and MC samples considered are, in each case, obtained by selecting events in an appropriate region, dominated by the process that each of the neural networks aim to identify.

The uncertainty related to the cosmic-ray tagger has been evaluated by comparing the distributions of the output scores for $Z \to \mu\mu$ events in data and MC samples. The tagger aims to discriminate muon spectrometer tracks originating from the interaction point from the ones originated in cosmic-ray events. For this purpose $Z \to \mu\mu$ events are chosen,

since prompt muons from Z boson decays, reconstructed using only the muon spectrometer informations, are expected to produce signal-like muon spectrometer tracks. The ratio of the two score distributions in data and MC simulated events, shown in Figure 6.2a, is applied as a binned scale factor to the muons used for the μDPJ reconstruction. It can be noticed that in the first two bins there is an higher data to MC discrepancy. This has been investigated and found to be not worrisome, for two main reasons. Firstly, this discrepancy was found not to be related with the training of the neural network itself, as variations on the training procedure were seen not to influence this behaviour. Secondly, this effect is overall marginal since it affects only a small fraction of the events, as it can be noticed from Figure 6.2a. The corresponding variation in the final signal yield, in each signal region, is taken as systematic uncertainty and in is found to be lower than 5% in the different signal samples considered.

For the QCD and BIB taggers, the ratios of data to MC simulated events distributions are computed from data and MC samples of multijet events, selecting signal-like events with reconstructed cDPJs. The binned distributions obtained performing the ratio of the two score distributions in data and MC simulated events are shown in Figure 6.2b, c for the QCD and BIB tagger respectively. It can be seen that the data to MC ratio is reasonably stable and close to unity for the case of the QCD tagger (Figure 6.2b), while higher discrepancy and ratios are observed in the case of the BIB tagger (Figure 6.2c). This has been studied and it has been observed that this behaviour does not affect the network training nor has a significant impact on the overall systematic uncertainty evaluation. The corresponding variations in the final signal yield in the signal regions, taken as systematic uncertainty, are found to be ranging between 2% to 11% for the QCD tagger, and between 3% to 14% for the BIB tagger.

Normalisation uncertainties

A minor source of uncertainty is associated to the estimate of the integrated luminosity recorded in the full Run-II dataset, which is then used for the normalisation of MC simulated events. In ATLAS, the main measurement of the luminosity is performed by the LUCID-2 detector [58], with the estimate of the uncertainty related the luminosity measurement found to be 1.7%, as described in Ref [57].

Another minor source of uncertainty, potentially affecting the normalisation of MC simulated events, is the one associated to the pile-up modelling. This uncertainty accounts for the differences between the predicted and measured inelastic cross-sections, which have been studied by the collaboration [113]. The corresponding uncertainty is evaluated by weighting the pile-up profile of MC generated events, by applying a scale factor to take into account possible differences in data and MC simulated events. The scale factors obtained are given by the ATLAS collaboration and are then varied within the corresponding uncertainty and applied by the analysis team to the MC samples of interest. The resulting difference

in signal yields is taken as systematic uncertainty.

6.1.2 Summary of systematic uncertanties

In the following, an overview of the overall impact of systematic uncertainties on the signal yield is given. In Figure 6.3, the relative contributions are reported separately for each of the six orthogonal signal regions, averaged among different signal samples, with small variations of the order of a few percent being observed as a function of the dark-photon mass. In Figure 6.3, the various dashed lines corresponds to different sets of systematic uncertainties:

- **Muon uncertainties** correspond to the close-by muon reconstruction uncertainty, affecting only the signal regions where at least one μDPJ is present;
- **Normalisation uncertainties** refers to the ones associated to the luminosity and pile-up modelling;
- **NN taggers** represents the total contribution associated to the Cosmic-ray tagger, the QCD tagger and the BIB tagger uncertainties, with the latter giving the largest contribution;
- **Triggers** refers to the contribution of the Narrow-Scan, CalRatio and Tri-muon MS-only triggers
- **Jet uncertainties** corresponds to the total contribution from uncertainties associated to the jet reconstruction and energy calibration.

It can be also noticed from Figure 6.3 how in the ggF category the leading systematics are the Muon and the Triggers uncertainties for channels involving the presence of μDPJs and cDPJs, respectively. For what concerns the WH category, the overall uncertainty is on average lower than for the ggF case. This is mainly due to the fact that this category is not affected by the dedicated triggers uncertainties and only affected by the Muon uncertainties in the $WH_{c+\mu}$ channel, where it is the leading systematic. The leading systematic in the WH_c and WH_{2c} channels is the one related to the jet uncertainties.

6.2 ABCD final estimate: unblinded results

In the previous chapter, the event selection for the two search categories, targeting respectively dark-photon originating from the decay of Higgs bosons produced via ggF and WH processes, has been presented. Moreover, the method used to evaluate the residual background in the SRs, referred to as ABCD method, has also been introduced and described.

Once the selection is finalised, the background estimation strategy is defined and the sources of systematic uncertainties are properly evaluated, as described in the previous

section, the analysis can be unblinded. This means that also data events in the signal regions can now be looked at, after running the selection over the full Run-II dataset. In Table 6.1, the observed number of events in each of the signal regions is shown, together with the observed number of events in the B, C and D control regions and the expected number of events in SR according to the ABCD method prediction. The errors in the table represent the total uncertainty on the background expectations, including systematic uncertainties. The expected number of events in region A (i.e. the SR) is shown both before (pre-fit) and after (post-fit) running the ABCD fit on unblinded data, assuming no signal, where the estimated contributions from cosmic-ray muons are subtracted before the fit and added back post-fit. This cross-check is done to ensure that the background prediction remains reasonably stable both before and after unblinding the signal regions. A good agreements is observed between pre-fit and post-fit SR events prediction, found to be within one standard deviation, and with respect to the observed number of events in SR. The fit performed is the Likelihood ABCD fit, introduced in Section 5.5.1. More details on the fitting procedure are given later in Section 6.3.1. In addition, the full Run-II dataset unblinded ABCD planes are shown in Figure 6.4 for all the six orthogonal ggF and WH category channels. As no excess is observed in data over the estimated background, the results obtained are used to set upper limits on the production cross-section times branching fraction, $\sigma \times B$ of the FRVZ and HAHM processes considered in the analysis, and will be discussed in detail later in this chapter.

Table 6.1: The table shows the observed and expected yields in the ABCD plane regions, with the error representing the total uncertainty on the background expectations, including systematic uncertainties. As mentioned in Section 5.5.2, in the ggF selection regions, the estimated contribution from cosmic-ray yields is subtracted from each of the ABCD regions before the final ABCD method estimation of the multijet background. The expected number of events in region A (i.e. the SR) is shown both before (pre-fit) and after (post-fit) running the ABCD fit in unblinded data assuming no signal. Both pre-fit and post-fit expected results are found to be within one standard deviation.

Selection	Analysis channel	CR-B	CR-C	CR-D	SR-A expected pre-fit	SR-A expected post-fit	SR-A observed
ggF	2μ	55	61	389	357 ± 79	317 ± 47	269
	$c + \mu$	169	471	301	108 ± 15	108 ± 13	110
	$2c$	97	1113	12146	1065 ± 200	1055 ± 82	1045
WH	c	1850	3011	155	95 ± 7	93 ± 12	103
	$c + \mu$	30	49	31	19 ± 5	19 ± 8	20
	$2c$	79	155	27	14 ± 3	14 ± 5	15

6.3 Limit setting

As already discussed in Section 6.2, after unblinding the ABCD planes no significant excess or disagreement is observed in data in the analysis signal regions. Therefore, the results of the search are used to set exclusion limits on the production cross-section times branching fraction, $\sigma \times B$, of the dark-photon production in Higgs decays via the FRVZ and HAHM processes. In the following sections, details are given about the likelihood fit and on the other methods and tools used to interpret the search results and set limits on the physics models of interest.

6.3.1 Likelihood fit

The fully data-driven background estimate in each SR is obtained by performing a maximum-likelihood fit to the yields in the four ABCD regions in data. The fitted likelihood function is formed from a product of four Poisson functions, one for each of the plane regions, describing the signal and background expectations. The ABCD ansatz is introduced as nuisance parameters in the background component of the expected yield in each region. The likelihood-based ABCD fit has the characteristic of being robust against control regions with a small number of events. Moreover, it takes also into account possible signal contamination in the control regions.

For what concerns the systematic uncertainties, previously described in Section 6.1, they are all included in the fit as nuisance parameters, and parametrised with Gaussian probability density functions that multiply the fit likelihood. The uncertainties are assumed to be uncorrelated across the various ABCD plane regions. As a cross-check, an alternative correlation model, where the uncertainties are assumed to be fully correlated across regions, has been investigated and this is found to have a negligible impact on the results. The mean value of the Gaussian probability distribution function is constrained by the nominal value of the parameter and the variance is defined by the 68% confidence interval of the systematic uncertainty associated with the parameter. The observed and expected numbers of events in the signal regions are extrapolated by the fit assuming no signal and with unblinded data in all ABCD regions in the fit. When comparing the results with a likelihood fit using blinded data in the SR, the background yields are found to be consistent within a few percent.

The upper limits on the signal strength [1], μ, are obtained using the CL_s method [114], performing a global simultaneous fit using the asymptotic calculator [115], considering the background and the predicted signal yields from MC simulation in the four ABCD regions. As a cross-check, the validity of the asymptotic approximation is checked against a full

[1] In physics, it is common to use as a parameter of interest of the likelihood the so-called signal strength μ. This quantity is defined as $s = \mu s_0$, where s is the expected signal yield, and s_0 the theory prediction for the signal yield s. Therefore, for instance, a value of $\mu = 1$ corresponds to the nominal value of the theory prediction for the signal yield.

calculation performed using pseudo-experiments. The CL_s values obtained with the two methods are always in agreement within few percent.

Model-dependent limits are computed for all the available signal samples considered in the analysis, for each of the ggF and WH channels. In the following the exclusion limits reported, unless otherwise clearly stated, refer to signal strength values excluded at 95% confidence level, which corresponds to μ values that yield values of CLs < 0.05.

The hypothesis test takes into account the expected signal yields, together with its corresponding uncertainties in the CRs and SRs, and for each case a SR+CRs likelihood fit to the observed data is performed. As an example of the result of this procedure, in Figure 6.5 the expected and observed CL_s are shown for different values of the signal strength. In particular, Figure 6.5 refers to the $ggF_{c+\mu}$ channel with reference to the FRVZ signal sample involving the production of two dark-photons, with a mass of 400 MeV each, in the decay of a ggF produced SM-like Higgs boson. In this case the upper-limit at 95% on the excluded signal strength is found to be $\mu = 0.34$, when considering a signal yield normalised to the full Run-II luminosity of 139 fb^{-1}, and a branching ratio, B, of the process $H \rightarrow\ 2\gamma_\text{d} + X$ equal to 1%. This is equivalent to an upper limit on B at 95% of 0.34%.

6.3.2 The lifetime re-weighting method

With the aforementioned likelihood fit, an upper limit on the branching ratio of the Higgs boson for a given signal process is set for a MC signal sample, generated with a particular choice of the dark-photon mass and $c\tau$. It is of interest for the analysis to extrapolate this limit to other values of the dark-photon mean proper lifetime in order to explore all the accessible phase space. This is done with a weighting method called "lifetime re-weighting", which is described in the following.

Taking in consideration a given MC signal sample, the LLPs, such as the dark-photon, are generated with a given mean proper lifetime, which will be referred to in the following as $c\tau_{ref}$. In this context it is possible to define a set of weights for each LLP in the process, which can be applied to the events in the reference sample in order to mimic a sample generated with a different mean proper lifetime of the LLPs $c\tau_{new} \neq c\tau_{ref}$.

The Poissonian decay probability, $p(t)$, of a single LLP is defined as:

$$p(t) = \frac{1}{\tau} e^{-\frac{t}{\tau}}, \tag{6.3.1}$$

where t corresponds to the lifetime of a single LLP. The weighting factor w, used to re-weight the distribution of the LLP decay lifetimes to a distribution with $c\tau_{new} \neq c\tau_{ref}$, is defined as the ratio of the two Poissonian decay probabilities:

$$w = \frac{\tau_{ref}}{\tau_{new}} \exp\big[- t\big(\frac{1}{\tau_{new}} - \frac{1}{\tau_{ref}}\big)\big]. \tag{6.3.2}$$

If more than one LLP is present in each event, the product of the per-LLP weights can be treated as a per-event weight, since each LLP decay is independent.

As a result, the lifetime re-weighting method enables to extrapolate the acceptance times efficiency ($A \times \epsilon$) of the analysis, obtaining a $A \times \epsilon$ vs $c\tau$ curve. In order to validate this method, the results of the extrapolation in terms of $A \times \epsilon$, at a given value of $c\tau$, have been compared with those of MC samples generated assuming that specific value of $c\tau$, referred to as validation samples. An example of this procedure is presented in Figure 6.6 for one of the WH FRVZ samples. In the figure the extrapolated $A \times \epsilon$ vs $c\tau$ curve is shown, together with the values obtained from the validation samples represented by solid markers in the figure. A good agreement with the extrapolated curve values is observed within statistical uncertainties, represented in the figure by the coloured bands. In Figure 6.6 it can also be noticed how the behaviour of the curves reflect the dependence of the analysis sensitivity in terms of the dark-photon proper decay length. Moreover, differences between the curves of the three channels can also be observed. In particular the curve related to the WH_c channel (green curve) presents a weaker dependency with respect to $c\tau$, as expected since in this channel the reconstruction of only one DPJ is required.

6.3.3 Upper limits as a function of the dark-photon mean proper lifetime

The upper limits obtained using the likelihood fit described in Section 6.3.1, corresponding to a given choice of the dark-photon mass and mean proper lifetime, can be extrapolated using the lifetime re-weighting method. As a result, the exclusion curves presented in Figure 6.7 are obtained, where the 95% CL observed upper limits on the branching ratio of the SM Higgs decay are shown as a function of $c\tau$. Figure 6.7 refers in particular to the FRVZ signal model hypothesis, where a SM-like Higgs production is considered, with two dark-photon produced in the final state. The sensitivity of each of the six search channels is reported in a separate sub-figure. It can be noticed how the interplay between the various channels unfolds for different ranges of dark-photon mass and $c\tau$. In particular, the channels including the presence of a reconstructed μDPJ are, as expected, the most sensitive ones when the $\gamma_d \to \mu\mu$ decays are present with a sizeable branching ratio. The $ggF_{2\mu}$ (see Figure 6.7a) and $ggF_{c+\mu}$ (see Figure 6.7b) channels provide the most stringent limits in this scenario, mainly due to the larger Higgs production cross-section (48.61 pb for the ggF and 0.46 pb for the WH). On the other hand, by construction, these channels are no longer sensitive when the dark-photon decays only to electron pairs (i.e. for $m_{\gamma_d} \leq 2m_\mu$). Therefore, the channels involving the presence of at least a cDPJ allow to recover sensitivity. In the scenario where dark-photon decays only to electron pairs, the WH_c (see Figure 6.7 d) and WH_{2c} channels (see Figure 6.7 f) are competitive with the exclusion provided by the ggF_{2c} channel (see Figure 6.7 c), mainly thanks to the WH production mechanism signature, and therefore the ability to exploit the single lepton triggers. As a consequence, those three channels have been combined in a simultaneous fit, which will be described in

the next section. To summarise, in this interpretation Higgs boson branching fraction to pair of dark-photons, decaying to μDPJs, larger than 1% are excluded at 95% CL if the dark-photons have a mean proper decay length $c\tau$ between 10 mm and 250 mm, and a mass between 0.4 GeV and 2 GeV. When considering dark-photon decays into pairs of cDPJs, Higgs boson branching fractions larger than 10% are excluded at 95% CL for mean proper decay lengths between 2 mm and 3 mm and masses between 17 MeV and 50 MeV.

In addition to the interpretation in the FRVZ signal hypothesis, with SM-like Higgs production and two dark-photon produced in the final state (i.e. $H \rightarrow 2\gamma_{\mathrm{d}} + X$), discussed above, the search results have been also interpreted considering alternative signal scenarios. This has been done in the context of the FRVZ model, considering different Higgs productions and different final states, but also, for the first time in this ATLAS search, in the context of the HAHM model. Exclusion limits referring to the HAHM model interpretation are presented in Figure 6.8. SM-like Higgs boson production is considered, with two dark-photons produced in the final state. The absence of additional hidden sector particles in the process, which translates in a larger p_T of the dark-photon, benefits the ggF category selection where an improved signal efficiency is observed, mainly because of increased trigger efficiencies. On the other hand, this does not translate in an improvement on the WH side of the search. Hence, a direct comparison of Figure 6.7 and 6.8 shows that more stringent constraints are set on the branching ratio of the SM Higgs decaying in a pair of dark-photons with respect to the FRVZ model interpretation. In terms of Higgs boson branching fraction to dark-photons, this translates in an exclusion at 95% CL of branching fractions larger than 1%, for pairs of dark-photons decaying into μDPJs. This refers to dark-photons having a mean proper decay length $c\tau$ between 4 mm and 200 mm, and a mass between 0.4 GeV and 2 GeV. When considering dark-photon decays into pairs of cDPJs, Higgs boson branching fractions larger than 10% are excluded at 95% CL for mean proper decay lengths between 1.5 mm and 8 mm and masses between 17 MeV and 100 MeV.

The analysis results can also be interpreted in terms of FRVZ models processes involving the production of four dark-photons ($H \rightarrow 4\gamma_{\mathrm{d}} + X$). The limits are shown in Figure 6.9. In this case, two back-to-back pairs of dark-photons are produced, with each pair found to be reconstructed as single DPJ. Therefore, the reconstruction of a single DPJ is more efficient when dark-photons in a pair are both decaying in the same final state, due to the fact that the two types of DPJ selections are mutually exclusive. As a consequence, for this interpretation an overall smaller efficiency of the analysis is found, and the constraints obtained are less stringent than in the benchmark final states involving two dark-photons. For this interpretation Higgs branching fractions above 10% are excluded at 95% CL for dark-photons with a mean proper decay length between 20 mm and 50 mm and a mass between 400 MeV and 1 GeV.

In Figure 6.10, exclusion limits as a function of the dark-photon $c\tau$ are shown for the

FRVZ process involving an 800 GeV Higgs-like scalar. In this case, the sensitivity is driven by the selection efficiency being higher than for the decay of the 125 GeV Higgs boson because of the larger p_T of the dark-photons produced. As a consequence, a good sensitivity is achieved across all the dark-photon mass spectrum considered. Limits are reported in terms of the $\sigma \times B$ of the FRVZ process, where a 5 pb cross-section is considered for these processes involving the production of a 800 GeV Higgs-like scalar. In this case, Higgs boson branching fractions above 10% are excluded at 95% CL if the dark-photons have a mean proper decay length between 6 mm and 30 mm and a mass between 400 MeV and 2 GeV.

The exclusion limits presented in this section are further used to produce two-dimensional exclusion contours in the plane of the dark-photon mass and kinetic mixing coupling constant. This will be described in detail in Section 6.3.5.

6.3.4 Combination of WH associated production and gluon-gluon fusion results

The event selection applied to the WH and ggF categories, described in detail in Chapter 5.4, ensures that the six signal regions defined in this analysis are mutually orthogonal, and therefore can be statistically combined to maximise the achieved exclusion power.

As mentioned in the previous section, this is particularly important in the case of the FRVZ signal samples, where the combination of different search channels helps in constraining the regions of the phase space dominated by the dark-photon decay to electron pairs $\gamma_d \to ee$. In this context, a combined likelihood fit of the ggF_{2c}, WH_c and WH_{2c} channels ABCD planes was performed, considering a product of the likelihood functions of the individual search channels with independent parameters, but with a common signal normalisation. An example of the results obtained with this procedure is presented in Figure 6.11, where 95% CL upper limits on the branching ratio of the $H \to 2\gamma_{\mathrm{d}} + X$ process are shown, considering a dark-photon with mass equal to 100 MeV. In this figure the combined result is shown together with the single search channels upper limits, highlighting the interplay between the WH and ggF exclusions. The complementarity between the three channels enables to extend the analysis exclusion for dark-photon proper decay lengths shorter than 2 mm and larger than 50 mm. This method is applied to all the available samples with $m_{\gamma_d} \leq 2m_\mu$.

6.3.5 Limits on the kinetic mixing as a function of the dark-photon mass

In order to be able to compare the results of this search to other constraints on dark-photon models, upper limits at 90% confidence level are also set in the context of the FRVZ model and the HAHM vector-portal model. This is needed since the exclusion limits from dedicated experiments are usually set considering this confidence level value, which corresponds to μ values that yield a CLs < 0.10. In addition, these limits are commonly

set in terms of the kinetic mixing parameter ϵ and the dark-photon mass m_{γ_d}, resulting in two dimensional exclusion contours.

To produce such limits, the information of the results from different dark-photon mass hypotheses has been used, deriving limits at 90% of the CL. The one-dimensional exclusions as a function of the dark-photon mean proper lifetime, obtained in the same way described in Section 6.3.2, are translated to limits as a function of the kinetic mixing parameter. This is done exploiting the relation between $c\tau$ and ϵ described in Equation 1.2.5. Subsequently, the branching ratio of the dark-photon allows to scale the one-dimensional limits to different mass hypotheses. In fact, for each dark-photon in an event, the branching fraction to standard model particles is described by Figure 1.6 and can be used to scale the limits to other mass hypotheses, taking into consideration the correct branching fraction in each case. At this point, the extrapolated limits are corrected by a linear interpolation of the signal efficiency between the available MC signal mass samples and the best exclusion limit from the relevant channels is considered. For instance, in the case of dark-photon masses $m_{\gamma_d} < 2m_\mu$, only the combination of the ggF and WH search regions that consider only the presence of reconstructed cDPJs is used.

An example of the resulting two-dimensional exclusion contours produced is presented in Figure 6.12, with reference to the 90% CL exclusion on the FRVZ model for different values of the branching ratio of the $H \rightarrow 2\gamma_{\mathrm{d}} + X$ process. The exclusion contours, shown as a function of the dark-photon mass and kinetic mixing parameter, are obtained for different assumptions on the decay branching fraction of the Higgs boson into dark-photon. These values are in the range between 0.1% and 10%, where each region filled with a darker shade of blue correspond to contours obtained considering a lower branching fraction. As an example, the contour shown with lightest blue corresponds to a choice of B = 10%, and can be directly compared to the limits obtained from the previous search. In addition to the Full-Run II displaced analysis exclusion, in Figure 6.12 the exclusion limit from the previous ATLAS displaced DPJ search [3] is also shown (dashed orange contour), as well as the limit from the ATLAS Run-I prompt search [4] (red contour). The direct comparison enables to underline the great improvements achieved in the Full Run-II search in terms of analysis sensitivity and exclusion limits. This is not only due to the larger available dataset, but mainly from the improvements obtained from the work presented in this thesis. One of the keys is the development of the Neural Network taggers, which results in an optimisation of the signal DPJ selections while achieving a greater background rejection. In this matter, the greatest impact comes from the development of the QCD tagger (see Chapter 5.3.2) which, together with the addition of the WH production channels, allowed to set for the first time limits below the threshold to produce two muons ($m_{\gamma_d} \leq 211$ MeV), allowing to reach a previously uncovered region of the phase space.

In addition to the FRVZ interpretation, the same two-dimensional exclusion contours have been derived for the HAHM model, and are shown in Figure 6.13. Also in this

case the extrapolated limits are corrected by a linear interpolation between two adjacent dark-photon mass samples and the most stringent limit from each channel is considered according to the respective region of the ϵ vs m_{γ_d} plane. A broader region of the phase-space is excluded in the HAHM interpretation with respect to the FRVZ one, since the ggF selection achieves an increased sensitivity on these samples as previously discussed in Section 6.3.3.

The same procedure has been used to produce exclusion contours for the remaining benchmark signal processes considered. In Figure 6.14a, the 90% CL exclusion contour in the ϵ vs m_{γ_d} plane, relative to the FRVZ interpretation involving the $H \rightarrow 4\gamma_{\mathrm{d}} + X$ process and the production of a SM-like Higgs boson, is shown. As for the previous contours, darker shades of the contour colour correspond to different assumptions on the SM Higgs branching ratio. As a reference, in Figure 6.14a, also the 10% contour obtained from the $H \rightarrow 2\gamma_{\mathrm{d}} + X$ process is shown, visible as an orange dashed line. Finally, in Figure 6.14b and 6.14c, the two-dimensional exclusion regions are presented for the FRVZ processes involving the production of respectively two and four dark-photons in the final state, when considering an 800 GeV Higgs-like heavy scalar. The same approach has been used also in this case, with the difference that the various coloured contours refer to different assumptions on the $\sigma \times B$ of the 800 GeV Higgs-like boson. As before, the exclusion limits have been produced using all the available MC samples, with the heaviest dark-photon mass sample being generated at a 15 GeV mass.

6.4 Comparison with other results in the context of vector portal model exclusions

The results obtained by the displaced DPJ analysis described in thesis can be compared with other state-of-the-art results in the context of vector portal models.

Limits on the decays of dark-photons to collimated pairs of leptons or hadrons were set in ATLAS also looking for prompt decays [4] of the dark-photon to charged leptons, and exploiting the monojet signature [116].

Prompt decays of the dark-photon to pair of charged leptons have been investigated in ATLAS using Run-I data, as described in detail in Ref [4]. This search explores a region of the phase-space complementary to the one investigated by the displaced DPJ search detailed in this thesis. The prompt DPJ search signature is represented by collimated pair of electrons or muons and focuses on decays consistent with zero decay length within the experimental resolution, exploiting the inner regions of the ATLAS detector.

The displaced Dark-Photon Jets analysis already exploits the outer regions of the ATLAS detector. Therefore, a different approach is needed to study LLPs with proper decay lifetimes large enough that most of the decays happen outside the ATLAS detector. For this region of the phase space, in ATLAS it is possible to look at events where all the en-

ergy associated to LLPs is lost outside the detector, contributing to the missing transverse momentum of the event. Final states with large missing transverse momentum recoiling against one highly energetic jet are referred to as *monojet events*. This kind of events can be exploited in many searches for beyond the SM physics, such as probing LLP signals in the case of very long proper lifetimes. In this scenario, the targeted signature is represented by multiple LLPs decaying outside the detector, where the whole system is recoiling against an Initial-State-Radiation (ISR) jet. The monojet analysis is described with great detail in detail in Ref [117], and its interpretation in terms of displaced dark-photon decays is described in Ref [116].

The results of the ATLAS searches are summarised in Figure 6.15, where the two-dimensional exclusion contours at 90% CL as a function of the dark-photon mass and kinetic mixing parameter are presented. As highlighted in the figure, the exclusion contours shown depend on the different assumptions on the branching fraction of the Higgs boson to dark-photon.

For what concerns the results from non-ATLAS searches, a summary of the most recent constraints on the dark-photon models, assuming the vector portal in both production and decay, was presented in Figure 1.7. It should be noted that among these results, the ATLAS ones, as mentioned before, are dependent also on the assumptions made on the Higgs boson branching fraction to dark-photon. This does not apply to LHCb results [118] and other dedicated experiment and non-collider results that rely only on vector portal coupling. Also in this case, the limits are presented as a function of the dark-photon mass and kinetic mixing term. Details about the aforementioned non-ATLAS results can be found in Ref [119].

Both ATLAS and non-ATLAS results are presented in the same plane for a more direct comparison, as reported in Figure 6.16. It can be noticed that ATLAS searches exclusion contours vary depending on the assumption made on the SM-like Higgs boson branching fraction to dark-photon. Overall there is good complementarity between the result obtained from the analysis described in thesis and the other state-of-the-art results in the context of vector portal model exclusions.

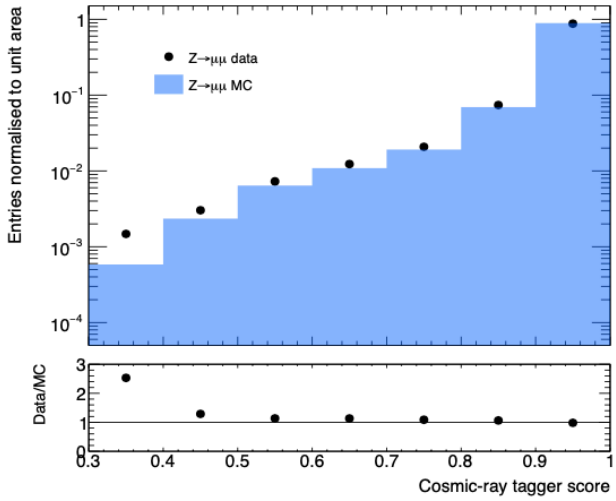

(a) Cosmic-ray tagger

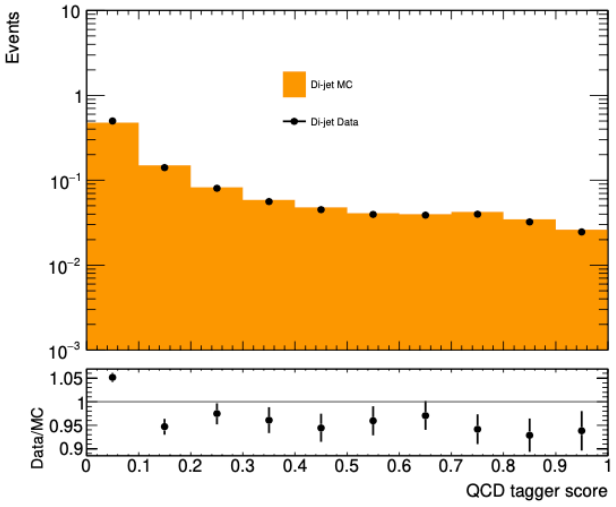

(b) QCD tagger

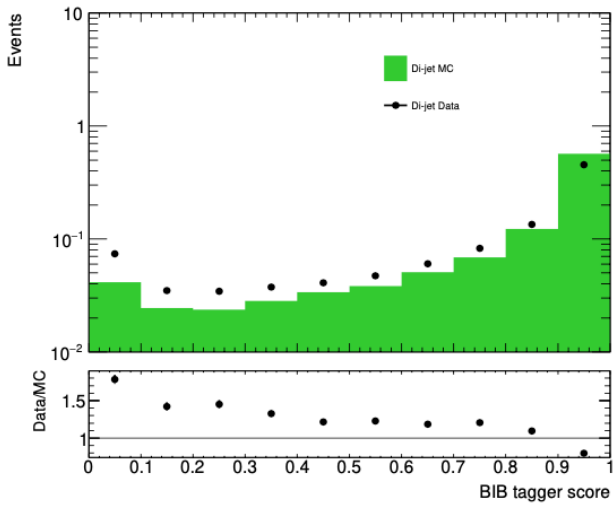

(c) BIB tagger

Figure 6.2: The figure shows the distributions of the output score of the three neural-network-based taggers used in the analysis. The distributions are computed for data and Monte Carlo events in different reference samples. Figure (a) shows the cosmic-ray tagger score in $Z \to \mu\mu$ events, while (b) and (c) show respectively the QCD tagger and BIB tagger output score distribution in multijet events. Figures from [2].

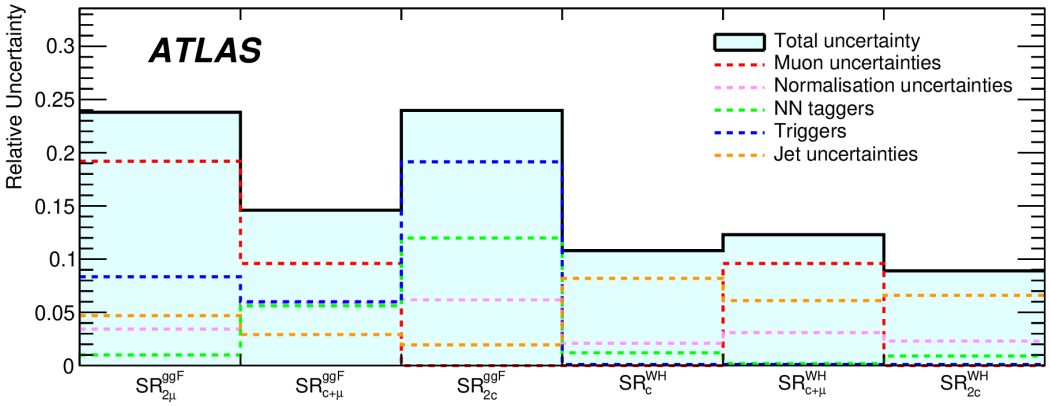

Figure 6.3: Figure showing the relative contributions from systematic uncertainties on the signal yields across the six signal regions of the analysis, as well as the total uncertainty. The figure is obtained averaging across the signal samples with two dark-photon in the final state, assuming signal production via a 125 GeV Higgs boson. In figure, the Muon uncertainties category correspond to the close-by muon reconstruction uncertainty. The NN taggers category contains the three taggers adopted in the analysis and is dominated by the BIB tagger uncertainty. The Triggers category contains all trigger systematic uncertainties, which are relevant only for the dedicated triggers in the ggF selection. The Jet uncertainties category contains all the jet-related systematic uncertainties. Some sets of systematic uncertainties apply to only a subset of the six signal regions. Figure from [2].

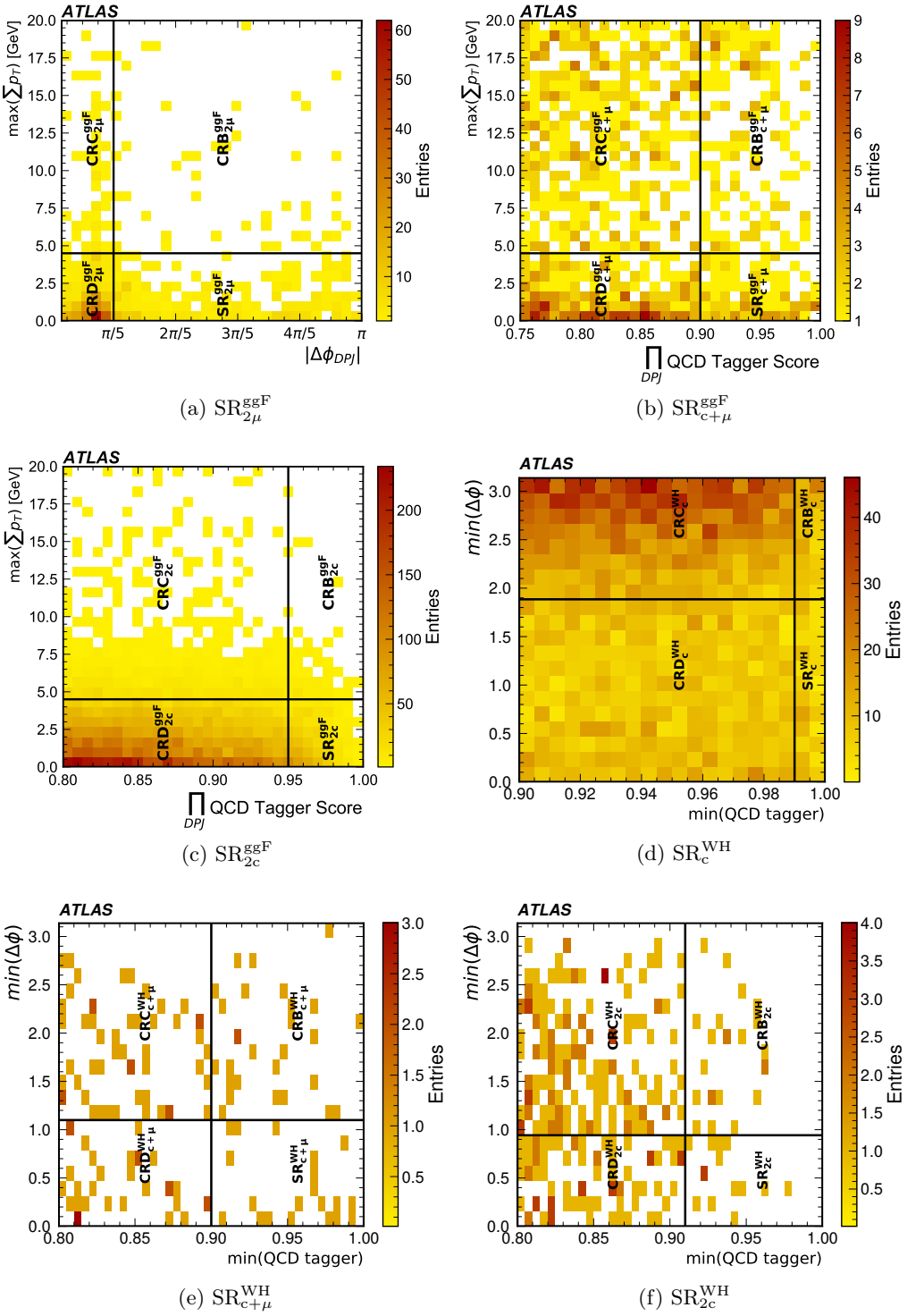

(a) $\mathrm{SR}_{2\mu}^{\mathrm{ggF}}$ (b) $\mathrm{SR}_{\mathrm{c}+\mu}^{\mathrm{ggF}}$

(c) $\mathrm{SR}_{2\mathrm{c}}^{\mathrm{ggF}}$ (d) $\mathrm{SR}_{\mathrm{c}}^{\mathrm{WH}}$

(e) $\mathrm{SR}_{\mathrm{c}+\mu}^{\mathrm{WH}}$ (f) $\mathrm{SR}_{2\mathrm{c}}^{\mathrm{WH}}$

Figure 6.4: The figure shows the per-event distributions in the ABCD planes, for all the six orthogonal ggF and WH category channels, when running on the full Run-II dataset collected by ATLAS. In Figures (a, b, c), the distribution for the ggF category channels is shown, while in figures (d, e, f), the event distribution of the WH category channels is shown. Figures from [2].

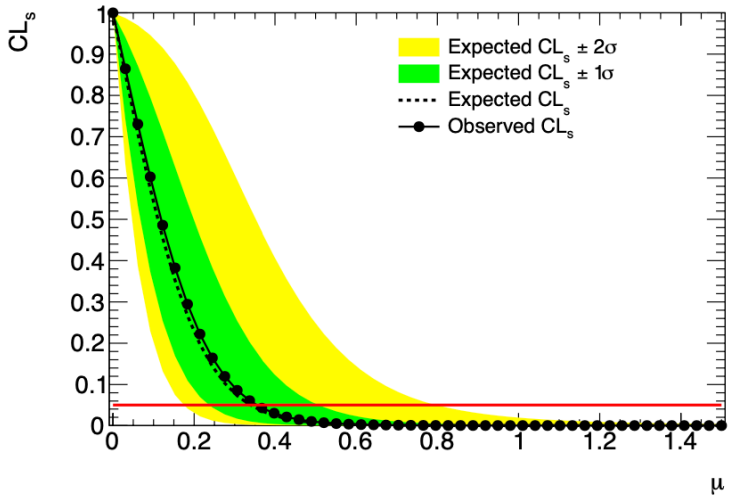

Figure 6.5: The picture shows the value assumed by the CL_s for different values of the signal strength. Here, a simultaneous fit of the four ABCD regions of the $ggF_{c+\mu}$ channel is performed. The signal sample considered is the FRVZ sample, where two dark-photon with a 400 MeV mass and with mean proper decay length of 50 mm are produced in the decay of a ggF produced SM-like Higgs boson. The upper-limit at 95% on the excluded signal strength is found to be $\mu = 0.34$, when considering a signal yield normalised to the full Run-II luminosity of 139 fb^{-1}, and a branching ratio, B, of the process $H \rightarrow 2\gamma_\text{d} + X$ equal to 1%.

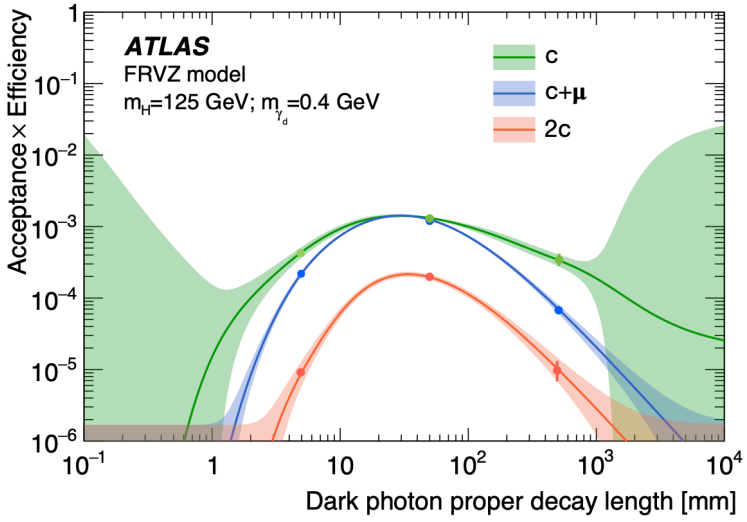

Figure 6.6: Acceptance times efficiency curves, extrapolated as a function of $c\tau$, are shown for the three WH analysis channels. The signal sample used to produce the curves is the FRVZ sample involving the WH associated production a SM-like Higgs boson, where two dark-photons with a 400 MeV mass and $c\tau = 50$ mm are produced. The three curves refers to the $A \times \epsilon$ of the WH_c (green), $WH_{c+\mu}$ (blue) and WH_{2c} (red) analysis channels. Markers, following the same colour scheme, show the relative $A \times \epsilon$ found using the additional MC samples generated with different values of $c\tau$, respectively $c\tau = 5$ mm and $c\tau = 500$ mm. A good agreement with the extrapolated curve values is observed, within statistical uncertainties, represented in the figure by the coloured bands.

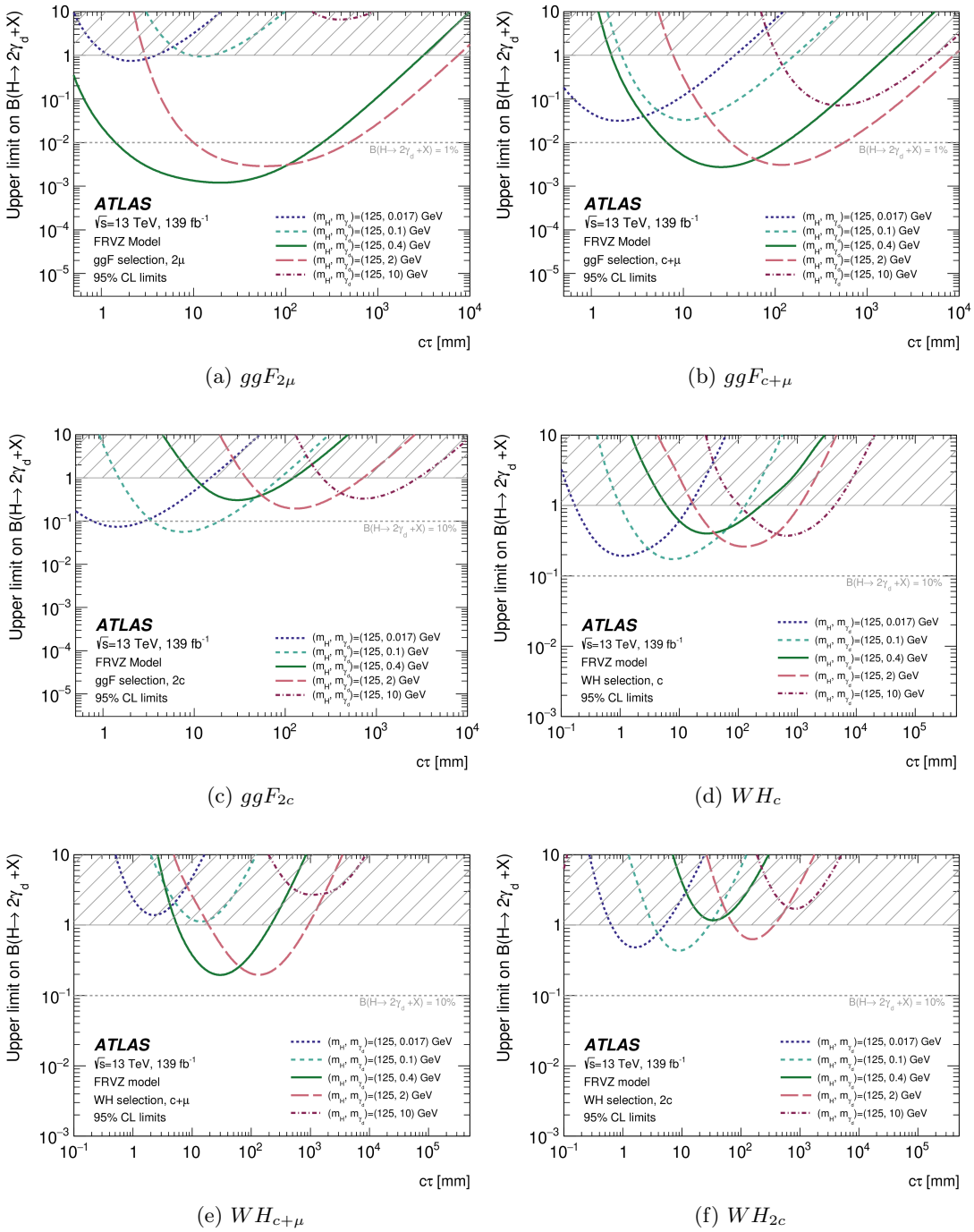

(a) $ggF_{2\mu}$ (b) $ggF_{c+\mu}$

(c) ggF_{2c} (d) WH_c

(e) $WH_{c+\mu}$ (f) WH_{2c}

Figure 6.7: Observed upper limits, at the 95% CL, on the branching ratio (B) for the process $H \to 2\gamma_d + X$, when considering the FRVZ model and the production of a SM-like Higgs boson. Limits in fuction of the dark-photon $c\tau$ are shown for different choice of the dark-photon mass. The limits for the ggF search channels are reported in separated sub-figures respectively for the $ggF_{2\mu}$ (a), $ggF_{c+\mu}$ (b) and ggF_{2c} (c). For what concerns the results from the WH channels, they are shown in (d) for WH_c, (e) for $WH_{c+\mu}$ and (f) for WH_{2c}. In all the sub-figures, the region where the hatched band is present, highlights the fact that the branching ratio considered becomes larger than unity. Figures from [2].

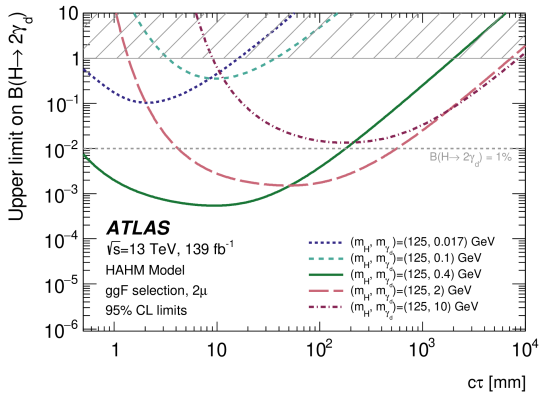

(a) $ggF_{2\mu}$

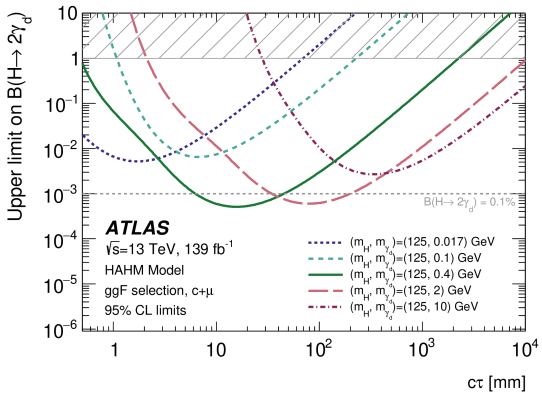

(b) $ggF_{c+\mu}$

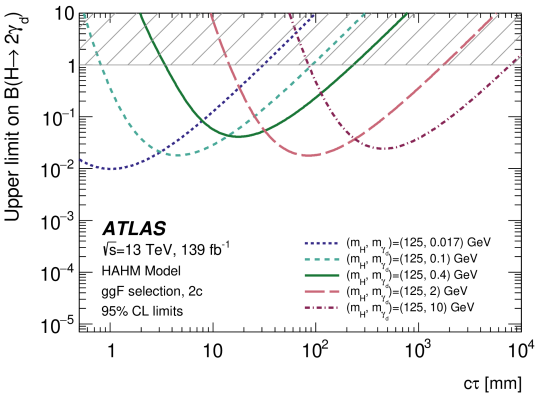

(c) ggF_{2c}

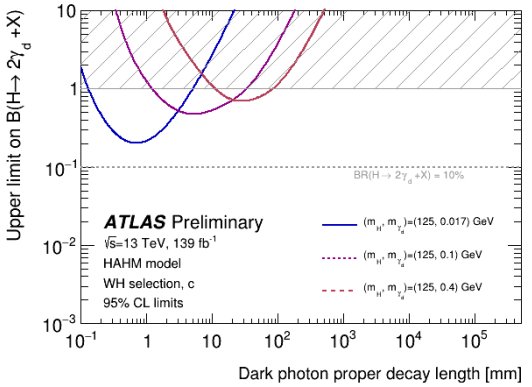

(d) WH_c

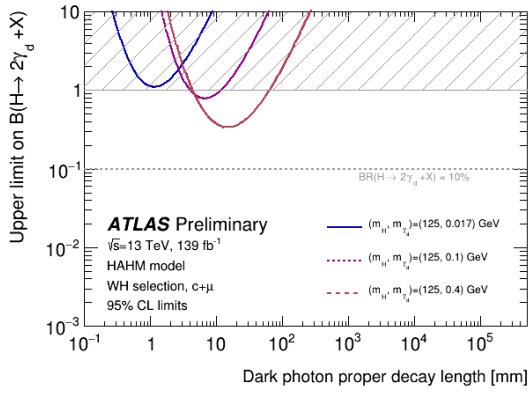

(e) $WH_{c+\mu}$

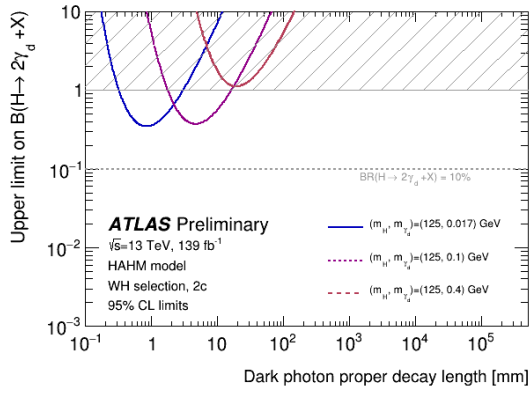

(f) WH_{2c}

Figure 6.8: Observed upper limits, at the 95% CL, on the branching ratio (B) for the process $H \to 2\gamma_d$, when considering the HAHM model and the production of a SM-like Higgs boson. Limits in fuction of the dark-photon $c\tau$ are shown for different choice of the dark-photon mass. The limits for the ggF search channels are reported in separated sub-figures respectively for the $ggF_{2\mu}$ (a), $ggF_{c+\mu}$ (b) and ggF_{2c} (c). For what concerns the results from the WH channels, they are shown in (d) for WH_c, (e) for $WH_{c+\mu}$ and (f) for WH_{2c}. In this interpretation, no limits are set in WH case for dark-photon masses above 400 MeV. In all the sub-figures, the region where the hatched band is present, highlights the fact that the branching ratio considered becomes larger than unity. Figures partially adapted from [2].

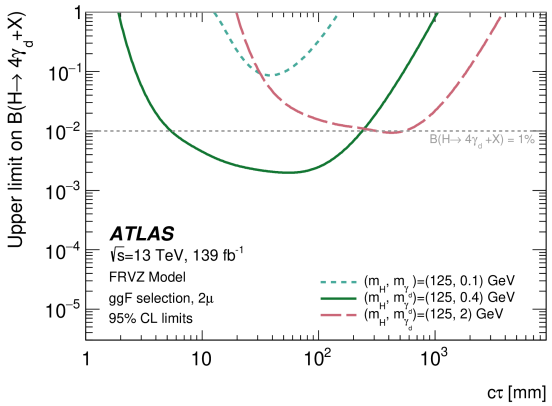

(a) $ggF_{2\mu}$

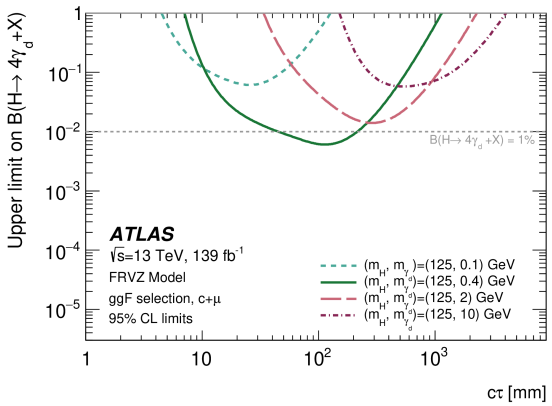

(b) $ggF_{c+\mu}$

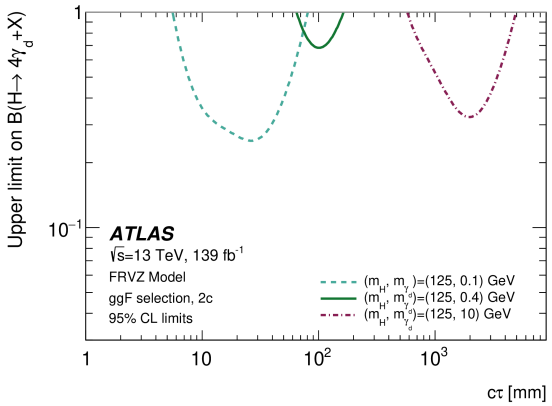

(c) ggF_{2c}

Figure 6.9: Observed limits, at the 95% CL, on the branching ratio (B) for the process $H \rightarrow 4\gamma_{\mathrm{d}} + X$ considering the FRVZ model and the production of a SM-like Higgs boson. Different choice of the dark-photon mass are shown and limits for the sensitive channels are reported. Figures from [2].

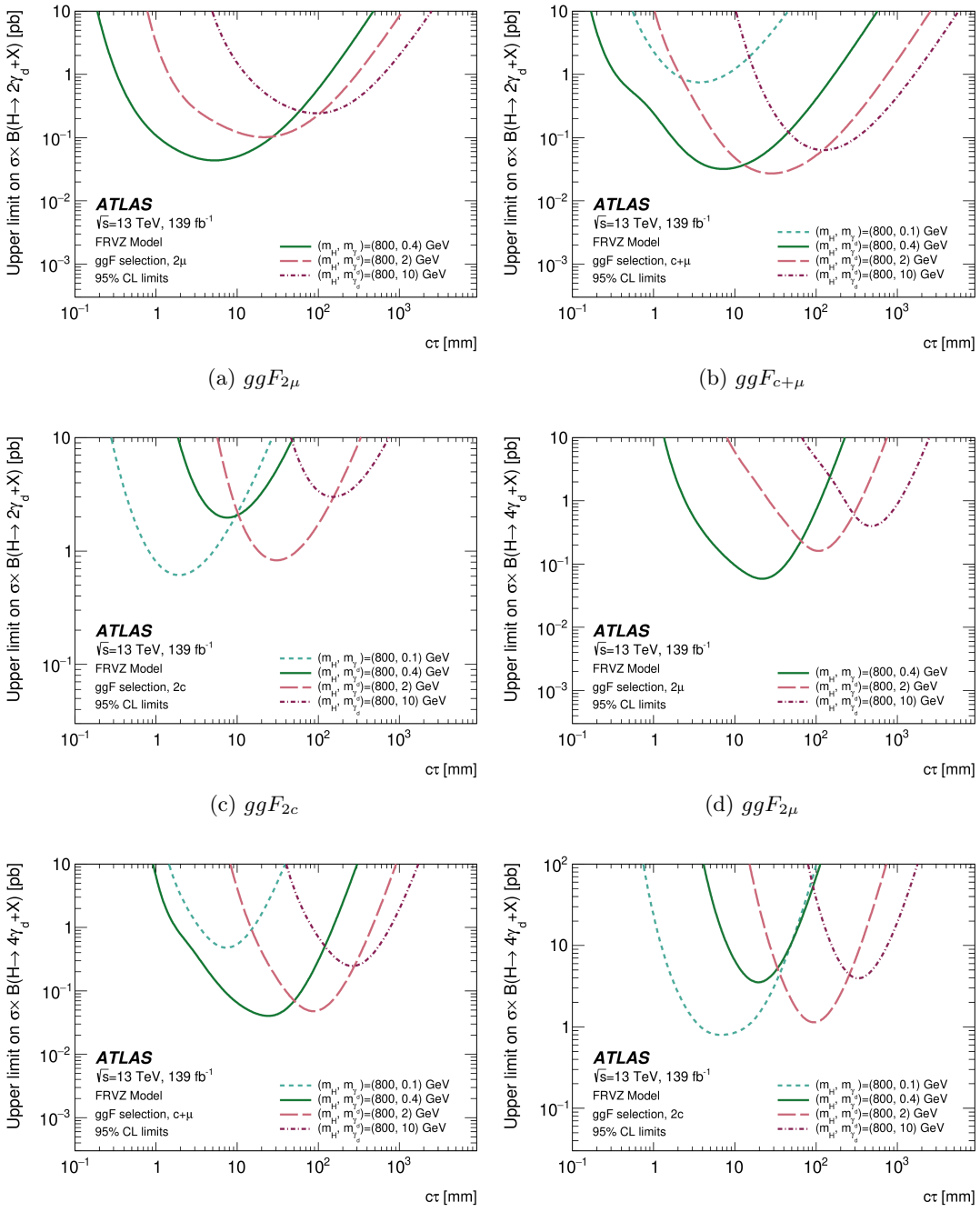

(a) $ggF_{2\mu}$ (b) $ggF_{c+\mu}$

(c) ggF_{2c} (d) $ggF_{2\mu}$

(e) $ggF_{c+\mu}$ (f) ggF_{2c}

Figure 6.10: Observed limits, at the 95% CL, on the $\sigma \times B$ for the FRVZ model considering the production of an 800 GeV Higgs-like boson. The three ggF search channels ($ggF_{2\mu}$, $ggF_{c+\mu}$ and ggF_{2c}) are shown, respectively, in (a, b, c) for the $H \rightarrow 2\gamma_{\mathrm{d}} + X$ process and in (d, e, f) for the $H \rightarrow 4\gamma_{\mathrm{d}} + X$. Multiple dark-photon masses have been considered and the limit for the sensitive channels are reported. Figures from [2].

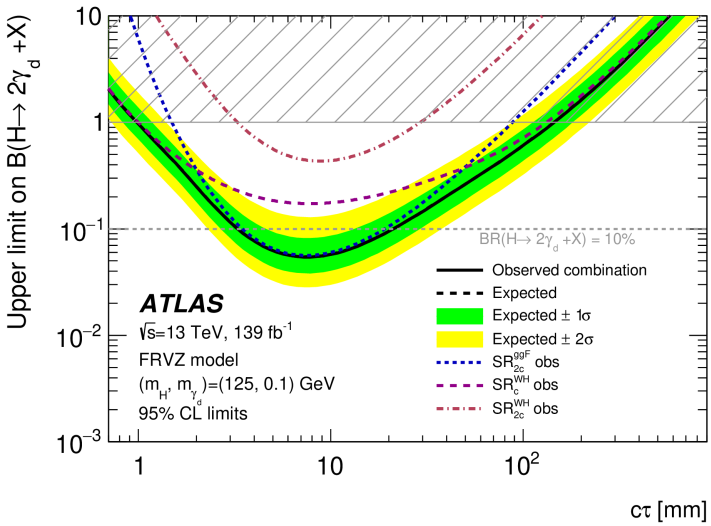

Figure 6.11: 95% CL upper limits on the branching ratio of the FRVZ $H \rightarrow 2\gamma_{\mathrm{d}} + X$ process, considering a dark-photon mass of 100 MeV and the production of a SM-like Higgs boson. The solid black line shows the observed exclusion limits obtained from a combined likelihood fit of the ggF_{2c}, WH_c and WH_{2c} channels. On the other hand, the dashed coloured lines show the individual limits of the search channels in the three search regions that are considered for the statistical combination. The complementarity between ggF and WH is visible and enables to extend the analysis exclusion for dark-photon proper decay lengths shorter than 2 mm and larger than 50 mm. Figure from [2].

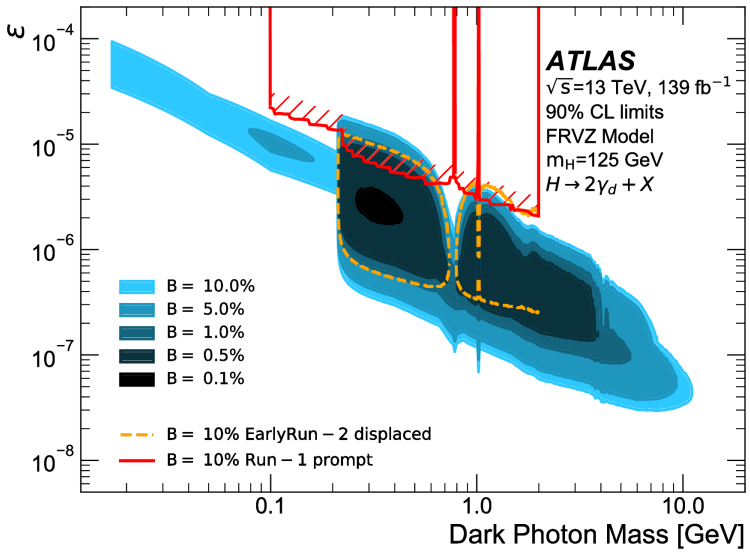

Figure 6.12: The figure shows two-dimensional 90% CL exclusion contours as a function of the dark-photon mass and of the kinetic mixing parameter ϵ in the context of the FRVZ model hypothesis. In particular the figure refers to the case of the production of SM-like Higgs boson in the $H \rightarrow 2\gamma_{\mathrm{d}} + X$ process. These limits are obtained assuming a decay branching fraction of the Higgs boson into dark-photon ranging between 0.1% and 10%, where each region filled with darker shades of blue correspond to contours obtained considering a lower branching fraction. The figure also shows the respective excluded regions from the previous ATLAS displaced DPJ search [3] (orange line) and ATLAS prompt [4] (red line) DPJ search. Figure from [2].

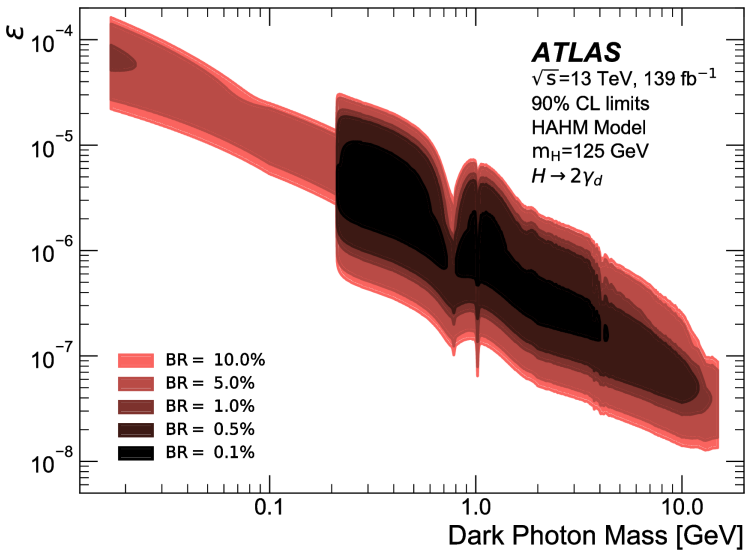

Figure 6.13: The figure shows two-dimensional 90% CL exclusion contours as a function of the dark-photon mass and of the kinetic mixing parameter ϵ in the context of the HAHM model hypothesis. In particular the figure refers to the case of the production of SM-like Higgs boson in the $H \rightarrow 2\gamma_{\mathrm{d}}$ process. These limits are obtained assuming a decay branching fraction of the Higgs boson into dark-photon ranging between 0.1% and 10%, where each region filled with darker shades of red correspond to contours obtained considering a lower branching fraction. A broader region of the phase-space is excluded in the HAHM interpretation, since the ggF selection achieves an increased sensitivity on these samples as previously discussed in Section 6.3.3. Figure from [2].

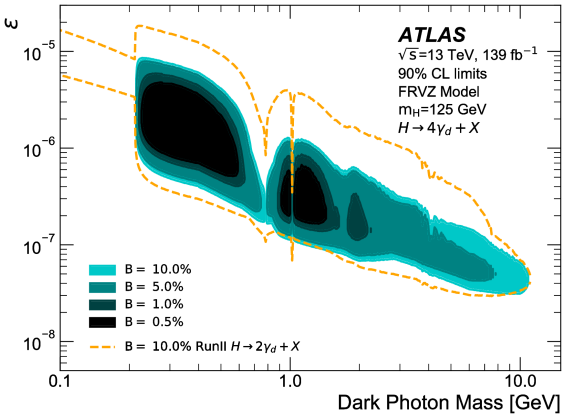

(a) $m_H = 125$ GeV, $H \rightarrow 4\gamma_{\mathrm{d}} + X$

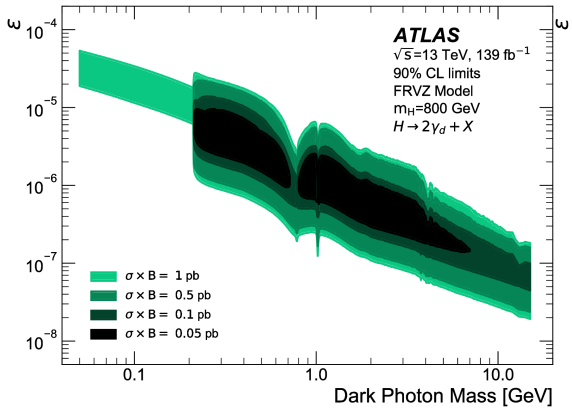

(b) $m_H = 800$ GeV, $H \rightarrow 2\gamma_{\mathrm{d}} + X$

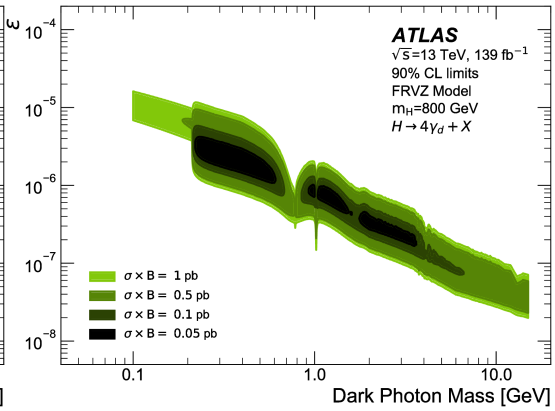

(c) $m_H = 800$ GeV, $H \rightarrow 4\gamma_{\mathrm{d}} + X$

Figure 6.14: Figure showing the two-dimensional exclusion contours for the FRVZ signal model alternative scenarios. In particular, (a) refers to the exclusion contours, as a function of the dark-photon mass and the kinetic mixing parameter, in the case of SM-like Higgs boson production involving the $H \rightarrow 4\gamma_{\mathrm{d}} + X$ process. As a reference is shown also the 10% contour obtained from the $H \rightarrow 2\gamma_{\mathrm{d}} + X$ process (see Figure 6.12), visible as an orange dashed line. In (b) exclusion contours are presented in the case of an 800 GeV Higgs-like boson production involving the production of two dark-photons in the final state. Finally, the exclusion contours presented in (c) are relative to the $H \rightarrow 4\gamma_{\mathrm{d}} + X$ process involving the production of an 800 GeV Higgs-like boson. In (a) the exclusion regions are reported for various choices of the Higgs boson branching fraction into dark-photons, while in (b) and (c) the excluded regions are reported for different choices of the $\sigma \times B$ of the Higgs-like 800 GeV scalar. Figures from [2].

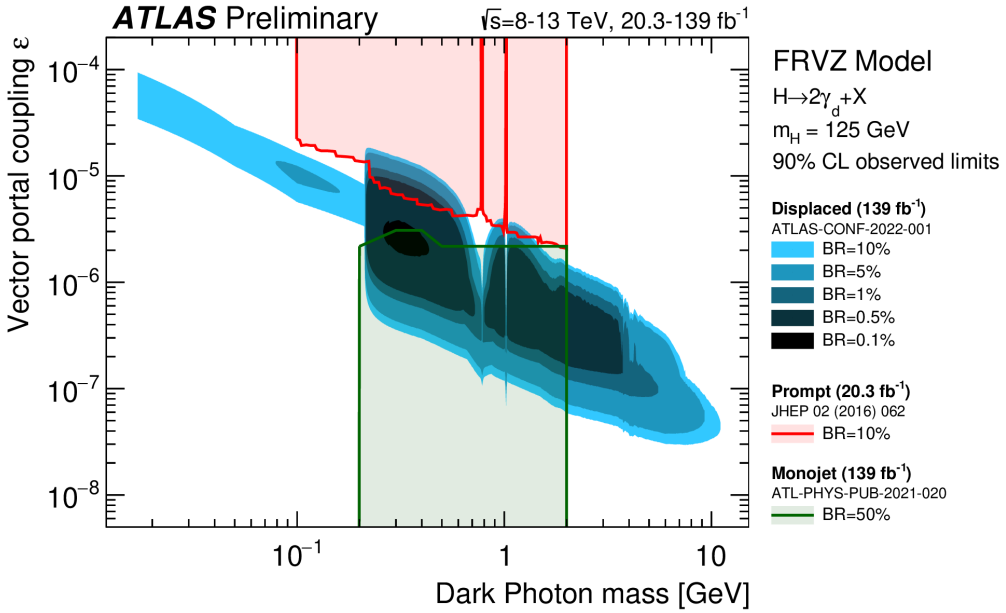

Figure 6.15: The figure shows two-dimensional 90% CL exclusion contours as a function of the dark-photon mass and of the kinetic mixing parameter ϵ in the context of the FRVZ model hypothesis. Results from three different ATLAS analyses are shown for different assumptions on the $H \to 2\gamma_{\mathrm{d}} + X$ branching ratio, ranging between 0.1% and 50%. The excluded regions from the Full Run-II displaced dark-photon search [2] are shown with darker blue tones for decreasing branching fractions. The exclusion contour depicted in red refers to the region excluded by the Run-I prompt dark-photon search [4], while the green contour depicts the region excluded by the monojet signature dark-photon re-interpretation in the context of the FRVZ vector portal model [116]. Figure from [120].

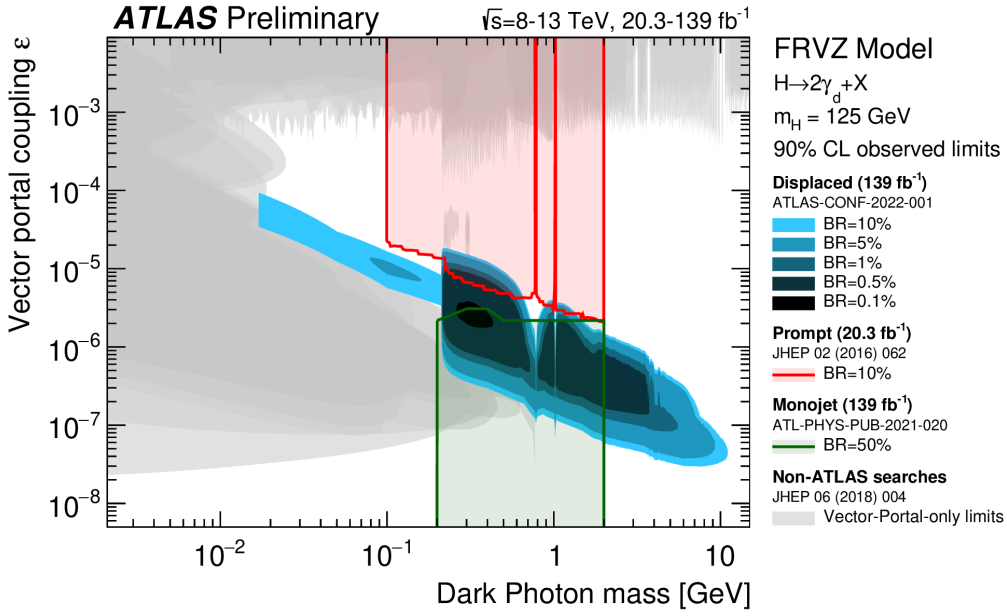

Figure 6.16: Exclusion limits as a function of the dark-photon mass and of the kinetic mixing parameter ϵ in the context of the dark-photon models, assuming the vector portal in both production and decay. Results from the Full Run-II displaced analysis described in this thesis are here compared with other ATLAS and non-ATLAS constraints. The results from three different ATLAS analyses are shown for different assumptions on the $H \rightarrow 2\gamma_{\mathrm{d}} + X$ branching ratio, ranging between 0.1% and 50%. The excluded regions from the Full Run-II displaced dark-photon search [2] are shown with darker blue tones for decreasing branching fractions. The exclusion contour depicted in red refers to the region excluded by the Run-I prompt dark-photon search [4], while the green contour depicts the region excluded by the monojet signature dark-photon re-interpretation in the context of the FRVZ vector portal model [116]. Results from non-ATLAS searches [119] are shown by the grey shaded regions. It can be noticed the nice interplay between the result obtained from the analysis described in thesis and the other state-of-the-art results in the context of vector portal model exclusions. Figure from [120].

Conclusions

Possible extensions of the Standard Model often predicts the existence of a dark sector, weakly coupled to the SM, where unstable dark states may be produced, resulting in the presence of long-lived particles. LLPs can leave unconventional signatures in the detector which are challenging to search for and, therefore, may have evaded detection until now. With the continuing absence of any obvious signs of new physics in LHC data, it is crucial to target unconventional signatures of new particles to ensure that new physics is not just hiding in plain sight within the currently available dataset. This thesis has presented a search for light long-lived neutral particles which decay into collimated pairs of fermions within the ATLAS detector. The dataset collected between 2015 and 2018 (Run-II), corresponding to 139 fb^{-1} of pp collisions at $\sqrt{s} = 13$ TeV, was analysed. No evidence of new physics involving long-lived dark-photons from Higgs boson decays was found. Upper limits on the Higgs boson branching fraction to dark-photons as a function of their mass and mean proper decay length $c\tau$ have been set and reported. When assuming SM Higgs boson production cross-sections, branching fractions above 1% were excluded at 95% CL for Higgs boson decays to two dark-photons with mean proper decay length between 10 mm and 250 mm and mass between 0.4 and 2 GeV. The sensitivity to displaced dark-photon decays, and the corresponding analysis exclusion limits have been significantly improved with respect to the previous rounds of the analysis. This has been achieved thanks to the addition of an event selection targeting long-lived dark-photons from decays of Higgs bosons produced in association with a W boson, the use of a larger dataset and the development of new methodologies for reconstructing dark-photon candidates and improved background rejection based on deep learning classifiers.

In addition, this thesis has also presented work which has been carried out in the context of the ATLAS HL-LHC upgrade. During this new phase the LHC instantaneous luminosity will dramatically increase, and therefore the ATLAS detector will be subject to a number of major upgrades in order to cope with the new challenging running conditions. This includes the installation of a new tracking detector, the ATLAS ITk. The studies presented in this thesis concern the validation of a new software for the reconstruction of testbeam data, where ITk modules performances are tested and evaluated.

Appendix A

ATLAS Inner Tracker strip modules testbeam data reconstruction

In this appendix, an overview is given about the technical work that has been carried out in the context of testbeam data reconstruction for the ATLAS Inner Tracker (ITk) upgrade [121]. At first, an overview of the ATLAS ITk upgrade is given in Section A.1, followed in Section A.2 by the description of the testbeam experimental setup. Furthermore, in Section A.3 an overview of the testbeam data reconstruction frameworks is given. Finally, in Section A.4 details are given about the efforts made towards the implementation and validation, in the context of ITk strip testbeam data reconstruction, of a new framework, referred to as Corryvreckan [122], with an overview of the current status and plans for this effort.

A.1 The High-Luminosity LHC and the ATLAS ITk upgrade

ATLAS is currently in the Run-III data-taking period, which will be followed by the Long Shutdown 3 (LS3) where the LHC will be upgraded for the next phase of the scientific programme, the High-Luminosity LHC [123] (HL-LHC). Therefore, during LS3, ATLAS will be subject to a number of major upgrades of the detector in order to cope with the new challenging running conditions.

During the HL-LHC phase, a peak instantaneous luminosity of $7.5 \times 10^{34}\, cm^{-2}s^{-1}$ at $\sqrt{s} = 14$ TeV is expected, corresponding to an average of 200 inelastic pp collisions per bunch-crossing, with a total integrated luminosity of 3000-4000 fb^{-1} planned to be recorder by the experiments during this period. All these values exceeds by far the design of the ATLAS detector, as it was described in Chapter 2. Hence, a number of detector upgrades are needed, including the installation of a new tracking detector with better performance and higher radiation tolerance, the ATLAS ITk.

ATLAS ITk upgrade

The ATLAS ITk is an all-silicon tracking detector consisting of pixel [124] and strip [125] modules. The ITk structure will consist of five concentric pixel barrel layers, surrounded by four strip barrel layers. The endcaps will consist of pixel rings of different radii and six strip disks placed respectively on each side of the pixel and strip barrel. A scheme showing the cross-section of one quadrant of the ITk detector is shown in Figure A.1, while its corresponding simulated layout is illustrated in Figure A.2.

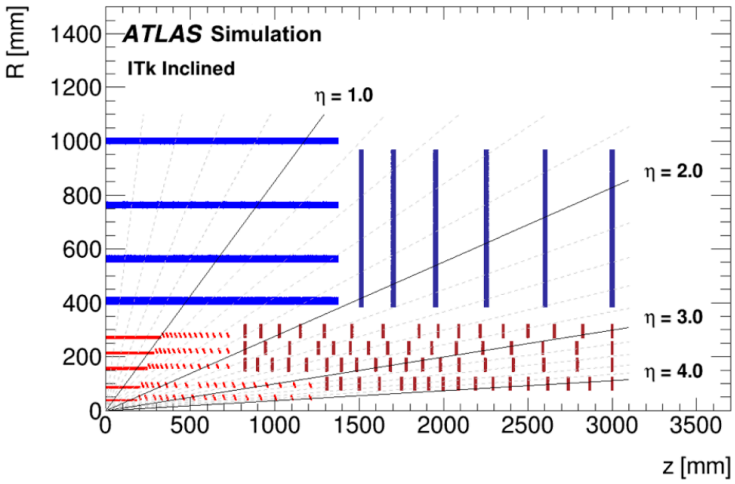

Figure A.1: Schematic layout of one quadrant of the ATLAS ITk detector [121]. The red coloured lines corresponds to the ITk pixel sub-detector layers, while the blue components represent the ITk strip sub-detector layers. The horizontal axis goes along the beam line and the origin of axes lies in the interaction point. The vertical axis corresponds to the radius measured from the beam axis.

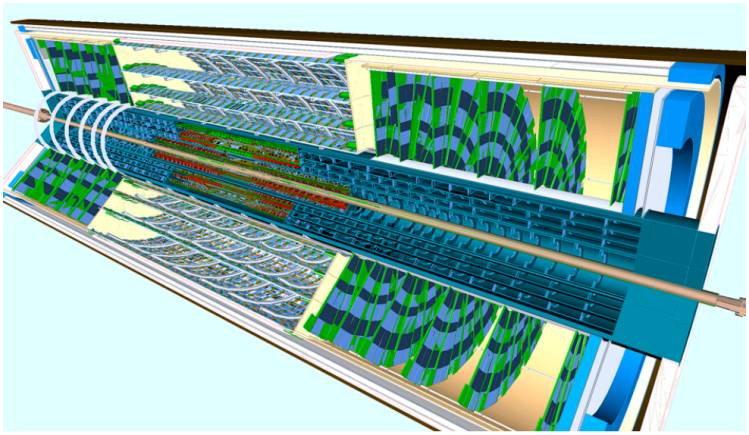

Figure A.2: Simulated layout of the ATLAS ITk tracking detector [121], with the inner pixel sub-detector surrounded by the strip sub-detector.

The ATLAS ITk strip detector, composed of four concentric barrel layers and one end-cap section with six disks on each of its barrel sides, will cover the pseudo-rapidity

range $|\eta| < 2.7$ and consist of a series of different modules. The inner two barrel layers accommodate the Short Strip modules, consisting of parallel strips of 24.16 mm, while the outer two layers include Long Strip modules with 48.35 mm strips. The end-cap modules are of six different geometries and are mounted on petals, where 32 petals compose one endcap disk, with the sensors having strip lengths varying from 19.0 mm to 60.1 mm.

In this following, the focus will be in particular on the modules used in the two outer layers, the so-called Long Strip modules. Prototypes for this kind of modules have been studied and tested during the 2019 test beam campaign and are the object of the studies described in the following sections.

A.2 Testbeam experimental setup

In order to perform studies on the characterisation and performance of the ITk modules, testbeam measurements are made, where the real detector conditions are mimicked. The data used to perform the studies described in this chapter have been collected during the 2019 DESY testbeam campaign. The DESY testbeam facility and the experimental setup used are described in the following.

DESY testbeam facility

DESY, the Deutsches Elektronen-Synchrotron, provides testbeam facilities which can be used to test the performance of detector devices. In particular, the DESY-II synchrotron [126], which began operations in 1987, accelerates electrons or positrons in a momentum range between 1-6 GeV. A scheme representing the layout of the DESY-II test beam facility is presented in Figure A.3. Carbon fibers can be moved into the beam to create bremsstrahlung photons, which leave the line tangentially. The photons are then converted back to electrons with a secondary metal target. A dipole magnet is used to spread out the beam to three test beam halls, T21, T22 and T24, and to select beam particles with a certain energy. The electron beam used during the 2019 DESY testbeam campaign were tuned to an energy of 5.4 GeV.

Experimental setup

Test beam analyses at the DESY facility are performed using an EUDET-type beam telescope [127]. The telescope itself serves as a small tracking detector, comprising six silicon pixel MIMOSA 26 [128] sensors which are used to provide reference track hits. The telescope planes operate at a 80 MHz clock rate, which would produce huge amounts of data, much of which would be of no use to the subsequent analyses. Therefore, a triggering system is used, which consists of four scintillators (two at the front of the telescope and two at the back) with photomultiplier tubes and a trigger logic unit. In addition, an FE-I4 timing plane [129] is used since an extra timing information is necessary for the measurement of

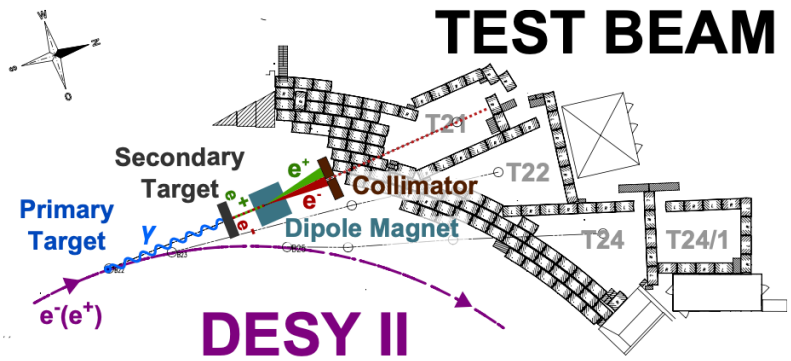

Figure A.3: Scheme illustrating the layout of the DESY-II test beam facility [126].

the detection efficiency, given the fact that the readout window of the telescope is too wide when compared to the one of the tested ITk module. Finally, a data acquisition (DAQ) system is present in order to read out the hits and trigger information. As an example, a photograph of the experimental setup from the April 2019 testbeam is shown in Figure A.4. It can be noticed how in this configuration the device under test (DUT) is placed between the two groups of three telescope planes, which are also referred to as beam telescope arms.

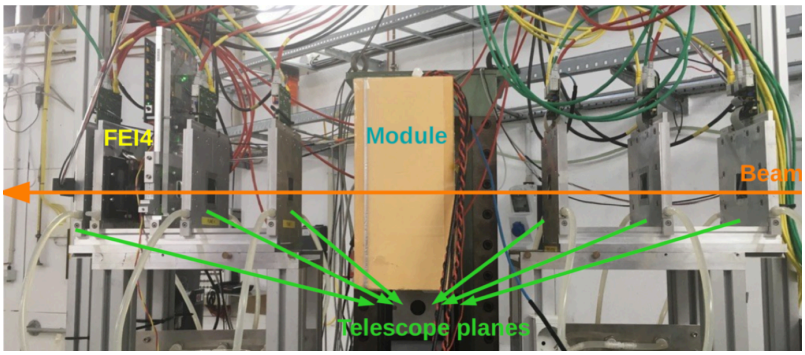

Figure A.4: A photograph of the EUDET telescope [127] and the tested module setup from the April 2019 testbeam. The six telescope planes are visible, with the ITk Long Strip module situated between the two groups of three telescope planes. The FE-I4 timing plane is also visible.

A.3 Data reconstruction frameworks: EUTelescope and Corryvreckan

The raw data taken during the testbeam is processed in three steps:

- **the raw data-taking and pre-processing:** this is performed using the EUDAQ software [130], which allows to read out the data from the single devices and perform the event building, resulting in an output where the data streams from different detectors can be merged and stored for further analysis;

- **the track and event reconstruction:** this is performed using dedicated reconstruction frameworks and includes the grouping of the hits detected by the individual detectors, the alignment of the telescope planes and the fitting of the tracks;

- **the data analysis:** usually performed using standalone python scripts and consisting of more detailed tests on module performances, including charge collection, noise occupancy, detection efficiency, and tracking performances.

The studies presented focuses in particular on the track and event reconstruction step and on the frameworks used.

Historically, the reconstruction of testbeam data has been performed using the EUTelescope framework [131], which makes use of a multi-step approach and where the most important steps are: clustering, hit making, alignment and finally track-fitting. This framework has given solid results and has extensively been used for both ATLAS ITk pixel and strip testbeam data reconstruction. However, in recent times several issue concerning the use of this framework have been identified, mainly due to two reasons. The first one is related to the fact that the software is currently unmaintained and will not be developed or supported anymore in the future. Secondly, EUTelescope relies on many scattered dependencies, which means that a change in any of the related softwares involved can result in a potential source of problems for the use of the framework.

As a results of this, it became evident that an alternative framework was needed to supplant in the long term the usage of EUTelescope. An ideal candidate has been identified in the Corryvreckan reconstruction framework [122].

Corryvreckan

Corryvreckan is a testbeam data reconstruction framework which has been released in 2019 [122] and has a series of characteristics which are particularly interesting. The software is a CERN based community project, that benefits from active participation in the development and code contributions from users. One of the framework's key characteristics is that it reduces external dependencies to a minimum by implementing its own data format, with the only explicit dependency being the one on the ROOT framework [132]. Corryvreckan is based on a modular concept of the reconstruction chain, meaning that the framework is extremely flexible and the user can add new functionalities, such as event loaders to support different data formats or analysis modules to investigate specific features of detectors, without having to deal with centrally provided items. On the other hand, Corryvreckan was initially developed to test pixel-like DUTs and even though it can potentially be extended to the test strip-like DUTs, this has not been done before and dedicated studies and software updates are needed.

In the next section, details are given about the studies carried out by the author of this thesis to contribute to the transition from EUTelescope to Corryvreckan.

A.4 ITk strip testbeam data reconstruction with Corryvreckan

The Corryvreckan framework was developed, and used so far, to test only pixel-like DUTs. As a first step in the transition from EUTelescope to Corryvreckan, the choice was made to re-analyse the April 2019 DESY testbeam data, where unirradiated Long Strip modules were used as DUTs, in order to perform a full comparison between the results obtained using EUTelescope as a reference and the ones obtained by adapting Corryvreckan to the use of strip-like DUTs. The decision to use this particular campaign was motivated by the fact that both EUTelescope and Corryvreckan are designed for DUTs whose geometry can be described by Cartesian coordinates, which is the case for the ITk barrel strip modules. On the other hand, the ITk strip endcap modules need a dedicated software development since their geometrical shape can only be described in terms of polar coordinates. Therefore, for the sake of simplicity, it was decided to start the comparison between the two frameworks from the reconstruction of test beam data involving barrel strip modules.

In order to adapt the Corryvreckan framework to the specific reconstruction of DESY testebeam data involving strip-like DUTs, a first step was to build new so-called *converters* which have the function of allowing the communication between the raw data-taking software used (EUDAQ) and the reconstruction software for each module involved in the process. Once this was done, the next step has been to perform a test of the Corryvreckan reconstruction chain. A scheme illustrating the workflow involved in the Corryvreckan reconstruction chain is presented in Figure A.5. It can be noticed the modularity and flexibility of the whole reconstruction process. At first, the raw input data are needed, together with the Geometry file illustrating the details of each detector involved (e.g position, spatial resolution, pitch, type ecc.). Second, these information are passed to the Configuration file where the user has the total freedom to decide which module will be involved in the reconstruction process. Finally, a ROOT output file will be produced, together with updated geometry files. As a result of this, the user can, for instance, run the whole process only focusing on one step and one detector at a time, e.g aligment of telescope planes, and move to the next phase only when the desired objective is achieved.

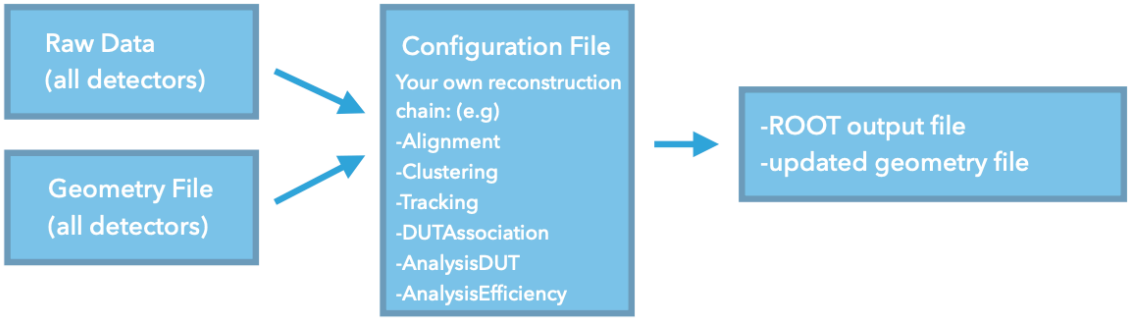

Figure A.5: Schematic illustration of the testbeam data reconstruction workflow when using the Corryvreckan framework [122].

As a proof of concept, the Corryvreckan reconstruction chain has firstly been tested on performing the Telescope planes alignment in runs of the April 2019 testbeam data. The result of this process is shown in Figure A.6 for one of the telescope planes, where the residuals obtained using Corryvreckan are compared to the results from the EUTelescope alignment. Similar results are observed, with small differences that can be explained in terms of the number of alignment iterations performed.

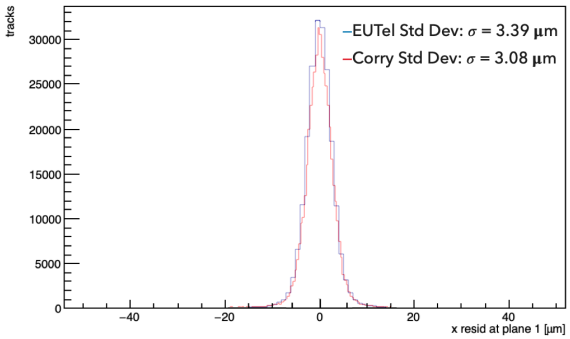

Figure A.6: Comparison of the residuals obtained after performing the Telescope planes alignment in EUTelescope (blue) and Corryvreckan (red). Overall, a good agreement is observed between the two frameworks, with small differences explainable in terms of the number of alignment iterations performed.

Once the telescope alignment step was successfully performed, the FE-I4 timing plane alignment was tested. This was crucial since the final evaluation of the Long Strip module efficiency needs to take into account the FE-I4 module track hit and timing information. In this step the reconstruction chain, that is then used for the Long Strip, is tested exploiting the now aligned telescope planes and treating the FE-I4 module as a DUT. After completing the timing plane alignment procedure, the FE-I4 is then treated as an additional telescope plane and a hit on this module will be required when building the final track to be associated to the hits observed in the Long Strip module. The results obtained exploiting data collected during the April 2019 testbeam using the Corryvreckan framework are compared to the ones obtained from the same data in the EUTelescope framework. The comparison is presented in Figure A.7. Comparable result are obtained for the residuals curves, with standard deviations of $\sigma(\text{EUTelescope}) = 21.81\,\mu\text{m}$ and $\sigma(\text{Corryvreckan}) = 22.43\,\mu\text{m}$ both in the expected range for the FE-I4 plane correct alignment.

ITk Long Strip module: alignment and efficiency

Once the Corryvreckan reconstruction chain was tested on the telescope and timing plane, the final step consisted in running the whole chain using the Long Strip module as DUT and the newly developed converters to correctly acquire the informations from the raw data. At first, the alignment procedure was performed with all the aligned MIMOSA planes and FE-I4 used as telescope planes. The achieved results are shown in Figure A.8, where resid-

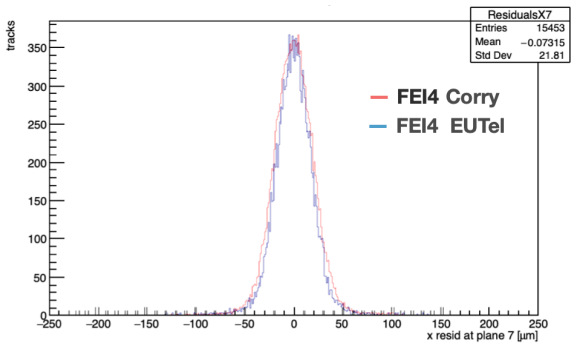

Figure A.7: Comparison of the residuals obtained after performing the FE-I4 timing plane alignment in EUTelescope (blue) and Corryvreckan (red). A nice agreement is observed between the two frameworks, with $< 1\,\mu$m differences in the curves standard deviations, with both being in the expected range for the FE-I4 plane correct alignment.

ual for ITk strip modules obtained running on Corryvreckan are shown, compared with the ones obtained from the EUTelescope reconstruction. Small differences are observed with Corryvreckan residuals being slightly worse than the EUTelescope ones. Results for the different data streams analysed are respectively $\sigma(\text{EUTelescope}) = 28 - 32\,\mu$m and $\sigma(\text{Corryvreckan}) = 35 - 37\,\mu$m, where σ refers to the standard deviation of the residuals curve. The results obtained are still very encouraging, with differences that have been analysed and arises from the different treatment of the material budget in the two frameworks and from the differences on the tracking procedure as well.

Furthermore, these differences are not a reason of concern and therefore, after performing the alignment process successfully, measurements of the Long Strip module efficiency have been carried out. In order to do this, after the alignment process, the tracking step is run again requiring one hit in all of the MIMOSA telescope planes and also a hit in the FE-I4 timing plane. At this point, in order to measure the efficiency of the DUT, the reconstructed tracks are matched to hits in the DUT. The global efficiency of the DUT will be then given by:

$$\epsilon_{DUT} = \frac{N_{matched\ tracks}}{N_{tracks}}, \tag{A.4.1}$$

where N_{tracks} corresponds to the total number of telescope + timing plane reconstructed tracks and $N_{matched\ tracks}$, to the subset of those which have a corresponding matching hit in the DUT. For unirradiated Long Strip modules, the target efficiency has to be above 99%. Corryvreckan allows to measure the DUT efficiency through the dedicated Analysis-Efficiency module. This module has been specifically modified in the course of the studies presented in order to allow the measurements of the global efficiency for strip-like detectors. Efforts are ongoing in order to extend the module capability to produce more detailed efficiency map for the whole strip.

In Figure A.9, the first measurement of the Long Strip module total efficiency made

using Corryvreckan is presented. Each point in the figure represents a run where a different threshold was applied to DUT. This is typically done to check the dependency on the threshold applied, as this can heavily impact the level of noise and occupancy of the module tested. The resulting shape obtained, often referred to as "S-curve", is the one expected and observed also in EUTelescope. In the plateau region a $> 99\%$ efficiency is observed.

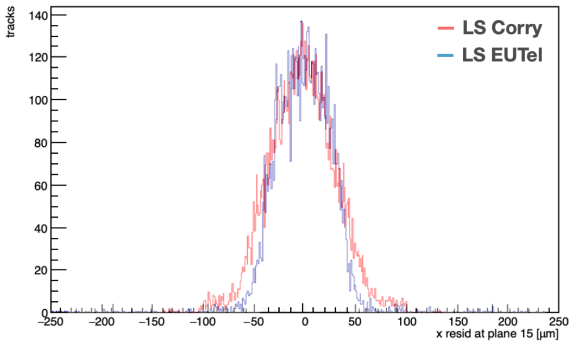

Figure A.8: Comparison of the residuals obtained after performing the ITk Long Strip alignment in EUTelescope (blue) and Corryvreckan (red). Minor differences are observed between the two frameworks. The results for the various runs of the April 2019 DESY testbeam data are respectively $\sigma(\text{EUTelescope}) = 28 - 32\,\mu\text{m}$ and $\sigma(\text{Corryvreckan}) = 35 - 37\,\mu\text{m}$. It is important to stress out that this was a first comparison and the outcome is very encouraging. The differences observed have been analysed and arises from the different treatment of the material budget in the two frameworks and from the differences on the tracking procedure as well. Efforts to further improve the agreement between the frameworks are ongoing.

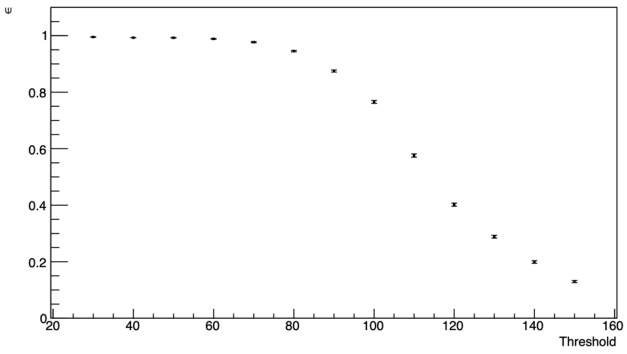

Figure A.9: Measurements of the total efficiency of an unirradiated Long Strip module in the April 2019 DESY testbeam made using the Corryvreckan reconstruction framework. Each point refers to a run where a run where a different threshold was applied to DUT. The error bars on each point represents the corresponding statistical error. The characteristic S shape is observed, with an efficiency measured in the plateau region being $> 99\%$.

In conclusion, the work presented in this thesis contributed to the process of transition from the use of EUTelescope to Corryvreckan for what concern the testbeam data reconstruction of the ITk barrel strip modules. At the time this thesis was written, efforts are

ongoing to further improve the usage of Corryvreckan for the reconstruction of barrel strip modules and to also implement the usage of polar coordinates in order to allow also the reconstruction of testbeam data involving ITk endcap strip modules as DUTs.

Bibliography

[1] Brian Batell, Maxim Pospelov, and Adam Ritz. Probing a secluded U(1) at B factories. *Phys. Rev. D*, 79:115008, 2009.

[2] Search for light long-lived neutral particles that decay to collimated pairs of leptons or light hadrons in pp collisions at $\sqrt{s} = 13$ TeV with the ATLAS detector. *arXiv*, 2022.

[3] Georges Aad et al. Search for light long-lived neutral particles produced in pp collisions at $\sqrt{s} = 13$ TeV and decaying into collimated leptons or light hadrons with the ATLAS detector. *Eur. Phys. J. C*, 80(5):450, 2020.

[4] ATLAS Collaboration. A search for prompt lepton-jets in pp collisions at $\sqrt{s} = 7\,\text{TeV}$ with the ATLAS detector. *Phys. Lett. B*, 719:299, 2013.

[5] Franz Mandl and Graham Shaw. *Quantum Field Theory*. 1985.

[6] K. Symanzik. Schrodinger representation in renormalisable Quantum Field Theory. In *Les Houches Summer School in Theoretical Physics: Recent Advances in Field Theory and Statistical Mechanics*, 1981.

[7] Emmy Noether. Invariant Variation Problems. *Gott. Nachr.*, 1918:235–257, 1918.

[8] A. Aguilar-Arevalo et al. Evidence for neutrino oscillations from the observation of $\bar{\nu}_e$ appearance in a $\bar{\nu}_\mu$ beam. *Phys. Rev. D*, 64:112007, 2001.

[9] CERN Webfest 2012. Standard Model infographic developed at the webfest. 2014.

[10] R. P. Feynman. Space - time approach to quantum electrodynamics. *Phys. Rev.*, 76:769–789, 1949.

[11] S. L. Glashow. Partial Symmetries of Weak Interactions. *Nucl. Phys.*, 22:579–588, 1961.

[12] Steven Weinberg. A Model of Leptons. *Phys. Rev. Lett.*, 19:1264–1266, 1967.

[13] Abdus Salam. Weak and Electromagnetic Interactions. *Conf. Proc. C*, 680519:367–377, 1968.

[14] Peter W. Higgs. Broken symmetries, massless particles and gauge fields. *Phys. Lett.*, 12:132–133, 1964.

[15] F. Englert and R. Brout. Broken Symmetry and the Mass of Gauge Vector Mesons. *Phys. Rev. Lett.*, 13:321–323, 1964.

[16] D. de Florian et al. Handbook of LHC Higgs Cross Sections: 4. Deciphering the Nature of the Higgs Sector. 2016.

[17] Georges Aad et al. Observation of a new particle in the search for the Standard Model Higgs boson with the ATLAS detector at the LHC. *Phys. Lett. B*, 716:1–29, 2012.

[18] Serguei Chatrchyan et al. Observation of a New Boson at a Mass of 125 GeV with the CMS Experiment at the LHC. *Phys. Lett. B*, 716:30–61, 2012.

[19] Lyndon Evans and Philip Bryant. LHC machine. *Journal of Instrumentation*, 3(08):S08001–S08001, aug 2008.

[20] Leonard Susskind. Dynamics of Spontaneous Symmetry Breaking in the Weinberg-Salam Theory. *Phys. Rev. D*, 20:2619–2625, 1979.

[21] P. A. Zyla et al. Review of Particle Physics. *PTEP*, 2020(8):083C01, 2020.

[22] Brian Shuve. Theory overview of long-lived particles at the LHC, 2017.

[23] Heather Russell. Russell H 2017 An experimental introduction to long-lived particle searches at the LHC. 2017.

[24] Jim Alexander et al. Dark Sectors 2016 Workshop: Community Report. 8 2016.

[25] Giorgio Arcadi, Abdelhak Djouadi, and Martti Raidal. Dark Matter through the Higgs portal. *Phys. Rept.*, 842:1–180, 2020.

[26] Brian Batell, Maxim Pospelov, and Adam Ritz. Exploring Portals to a Hidden Sector Through Fixed Targets. *Phys. Rev. D*, 80:095024, 2009.

[27] Yasunori Nomura and Jesse Thaler. Dark Matter through the Axion Portal. *Phys. Rev. D*, 79:075008, 2009.

[28] David Curtin, Rouven Essig, Stefania Gori, and Jessie Shelton. Illuminating Dark Photons with High-Energy Colliders. *JHEP*, 02:157, 2015.

[29] ATLAS Collaboration. Combination of searches for invisible Higgs boson decays with the ATLAS experiment. ATLAS-CONF-2020-052, 2020.

[30] Adam Falkowski, Joshua T. Ruderman, Tomer Volansky, and Jure Zupan. Discovering Higgs Decays to Lepton Jets at Hadron Colliders. *Phys. Rev. Lett.*, 105:241801, 2010.

[31] Adam Falkowski, Joshua T. Ruderman, Tomer Volansky, and Jure Zupan. Hidden Higgs Decaying to Lepton Jets. *JHEP*, 05:077, 2010.

[32] Matthew J. Strassler and Kathryn M. Zurek. Echoes of a hidden valley at hadron colliders. *Phys. Lett. B*, 651:374–379, 2007.

[33] LHC Machine. *JINST*, 3:S08001, 2008.

[34] Michael Benedikt, Paul Collier, V Mertens, John Poole, and Karlheinz Schindl. *LHC Design Report*. CERN Yellow Reports: Monographs. CERN, Geneva, 2004.

[35] Aad et al. The ATLAS Experiment at the CERN Large Hadron Collider. *JINST*, 3:S08003. 437 p, 2008. Also published by CERN Geneva in 2010.

[36] The CMS Collaboration et al. The CMS experiment at the CERN LHC. *Journal of Instrumentation*, 3(08):S08004–S08004, aug 2008.

[37] K. Aamodt et al. The ALICE experiment at the CERN LHC. *JINST*, 3:S08002, 2008.

[38] A. Augusto Alves, Jr. et al. The LHCb Detector at the LHC. *JINST*, 3:S08005, 2008.

[39] E. Mobs. The CERN accelerator complex - 2019. Complexe des accélérateurs du CERN - 2019. (CERN-GRAPHICS-2019-002), Jul 2019.

[40] ATLAS Collaboration. Luminosity determination in pp collisions at $\sqrt{s} = 13\,\text{TeV}$ using the ATLAS detector at the LHC. ATLAS-CONF-2019-021, 2019.

[41] *ATLAS magnet system: Technical Design Report, 1*. Technical design report. ATLAS. CERN, Geneva, 1997.

[42] Track Reconstruction Performance of the ATLAS Inner Detector at $\sqrt{s} = 13$ TeV. Technical report, CERN, Geneva, Jul 2015. All figures including auxiliary figures are available at https://atlas.web.cern.ch/Atlas/GROUPS/PHYSICS/PUBNOTES/ATL-PHYS-PUB-2015-018.

[43] M Capeans, G Darbo, K Einsweiller, M Elsing, T Flick, M Garcia-Sciveres, C Gemme, H Pernegger, O Rohne, and R Vuillermet. ATLAS Insertable B-Layer Technical Design Report. Technical report, Sep 2010.

[44] B. Abbott et al. Production and integration of the ATLAS insertable b-layer. *Journal of Instrumentation*, 13(05):T05008–T05008, may 2018.

[45] A. Ahmad et al. The Silicon microstrip sensors of the ATLAS semiconductor tracker. *Nucl. Instrum. Meth. A*, 578:98–118, 2007.

[46] ATLAS collaboration. Calibration of the ATLAS Transition Radiation Tracker. 2011.

[47] ATLAS Collaboration. Performance of the ATLAS Transition Radiation Tracker in Run 1 of the LHC: tracker properties. *JINST*, 12:P05002, 2017.

[48] ATLAS Collaboration. ATLAS Calorimeter Performance: Technical Design Report, 1996.

[49] Bernard Aubert et al. Construction, assembly and tests of the ATLAS electromagnetic barrel calorimeter. *Nucl. Instrum. Meth. A*, 558:388–418, 2006.

[50] ATLAS Collaboration. ATLAS Liquid Argon Calorimeter: Technical Design Report, 1996.

[51] ATLAS tile calorimeter: Technical design report. 12 1996.

[52] D. M. Gingrich et al. Construction, assembly and testing of the ATLAS hadronic end-cap calorimeter. *JINST*, 2:P05005, 2007.

[53] A. Artamonov et al. The ATLAS forward calorimeters. *JINST*, 3:P02010, 2008.

[54] ATLAS muon spectrometer: Technical design report. 6 1997.

[55] 2015 start-up trigger menu and initial performance assessment of the ATLAS trigger using Run-2 data. Technical report, CERN, Geneva, Mar 2016. All figures including auxiliary figures are available at https://atlas.web.cern.ch/Atlas/GROUPS/PHYSICS/PUBNOTES/ATL-DAQ-PUB-2016-001.

[56] Georges Aad et al. ATLAS data quality operations and performance for 2015–2018 data-taking. *JINST*, 15(04):P04003, 2020.

[57] Luminosity determination in pp collisions at $\sqrt{s} = 13$ TeV using the ATLAS detector at the LHC. 6 2019.

[58] G. Avoni et al. The new LUCID-2 detector for luminosity measurement and monitoring in ATLAS. *JINST*, 13(07):P07017, 2018.

[59] Georges Aad et al. Characterisation and mitigation of beam-induced backgrounds observed in the ATLAS detector during the 2011 proton-proton run. *JINST*, 8:P07004, 2013.

[60] ATLAS Collaboration. Performance of the ATLAS Trigger System in 2010. *Eur. Phys. J. C*, 72:1849, 2012.

[61] ATLAS Collaboration. Triggers for displaced decays of long-lived neutral particles in the ATLAS detector. *JINST*, 8:P07015, 2013.

[62] Imperial College London. Proton-proton collision scheme. Imperial College London website.

[63] Richard D. Ball et al. Parton distributions for the LHC run II. *JHEP*, 04:040, 2015.

[64] Richard D. Ball et al. Parton distributions with LHC data. *Nucl. Phys. B*, 867:244, 2013.

[65] John C. Collins. Sudakov form-factors. *Adv. Ser. Direct. High Energy Phys.*, 5:573–614, 1989.

[66] Johannes Bellm et al. Herwig 7.0/Herwig++ 3.0 release note. *Eur. Phys. J. C*, 76(4):196, 2016.

[67] Torbjörn Sjöstrand, Stefan Ask, Jesper R. Christiansen, Richard Corke, Nishita Desai, Philip Ilten, Stephen Mrenna, Stefan Prestel, Christine O. Rasmussen, and Peter Z. Skands. An introduction to pythia 8.2. *Computer Physics Communications*, 191:159–177, 2015.

[68] B. Andersson, G. Gustafson, G. Ingelman, and T. Sjöstrand. Parton fragmentation and string dynamics. *Physics Reports*, 97(2):31–145, 1983.

[69] D. Amati and G. Veneziano. Preconfinement as a property of perturbative qcd. *Physics Letters B*, 83(1):87–92, 1979.

[70] Enrico Bothmann et al. Event Generation with Sherpa 2.2. *SciPost Phys.*, 7(3):034, 2019.

[71] S. Agostinelli et al. Geant4a simulation toolkit. *Nuclear Instruments and Methods in Physics Research Section A: Accelerators, Spectrometers, Detectors and Associated Equipment*, 506(3):250–303, 2003.

[72] T. Sjöstrand, S. Mrenna, and P. Skands. A brief introduction to PYTHIA 8.1. *Comput. Phys. Commun.*, 178:852–867, 2008.

[73] The Pythia 8 A3 tune description of ATLAS minimum bias and inelastic measurements incorporating the Donnachie-Landshoff diffractive model. 8 2016.

[74] J. Alwall, R. Frederix, S. Frixione, V. Hirschi, F. Maltoni, O. Mattelaer, H. S. Shao, T. Stelzer, P. Torrielli, and M. Zaro. The automated computation of tree-level and next-to-leading order differential cross sections, and their matching to parton shower simulations. *JHEP*, 07:079, 2014.

[75] M. Cepeda et al. Report from Working Group 2: Higgs Physics at the HL-LHC and HE-LHC. *CERN Yellow Rep. Monogr.*, 7:221–584, 2019.

[76] Charalampos Anastasiou, Claude Duhr, Falko Dulat, Elisabetta Furlan, Thomas Gehrmann, Franz Herzog, Achilleas Lazopoulos, and Bernhard Mistlberger. High precision determination of the gluon fusion Higgs boson cross-section at the LHC. *JHEP*, 05:058, 2016.

[77] Oliver Brein, Abdelhak Djouadi, and Robert Harlander. NNLO QCD corrections to the Higgs-strahlung processes at hadron colliders. *Phys. Lett. B*, 579:149–156, 2004.

[78] Constraining the Dark Sector with the monojet signature in the ATLAS experiment. 2021.

[79] Patrick Meade, Michele Papucci, and Tomer Volansky. Dark matter sees the light. *JHEP*, 12:052, 2009.

[80] Johannes Backens and Marc Vanderhaeghen. X17 discovery potential in the $\gamma n \to e^+e^-n$ process at electron scattering facilities. *Phys. Rev. Lett.*, 128:091802, Mar 2022.

[81] T. Gleisberg, S. Höche, F. Krauss, M. Schönherr, S. Schumann, F. Siegert, and Winter J. Event generation with SHERPA 1.1. *JHEP*, 02:007, 2009.

[82] Stefano Frixione, Paolo Nason, and Giovanni Ridolfi. A positive-weight next-to-leading-order Monte Carlo for heavy flavour hadroproduction. *JHEP*, 09:126, 2007.

[83] Torbjorn Sjöstrand, Stephen Mrenna, and Peter Z. Skands. PYTHIA 6.4 physics and manual. *JHEP*, 05:026, 2006.

[84] Peter Zeiler Skands. Tuning Monte Carlo generators: The Perugia tunes. *Phys. Rev. D*, 82:074018, 2010.

[85] H.-L. Lai et al. New parton distributions for collider physics. *Phys. Rev. D*, 82:074024, 2010.

[86] J. Pumplin et al. New Generation of Parton Distributions with Uncertainties from Global QCD Analysis. *JHEP*, 07:012, 2002.

[87] Piotr Golonka and Zbigniew Was. PHOTOS Monte Carlo: a precision tool for QED corrections in Z and W decays. *Eur. Phys. J. C*, 45:97–107, 2006.

[88] Vertex Reconstruction Performance of the ATLAS Detector at "\sqrts = 13~\textrmTeV". 2015.

[89] Morad Aaboud et al. Electron reconstruction and identification in the ATLAS experiment using the 2015 and 2016 LHC proton-proton collision data at $\sqrt{s} = 13$ TeV. *Eur. Phys. J. C*, 79(8):639, 2019.

[90] ATLAS Collaboration. Muon reconstruction performance of the ATLAS detector in proton–proton collision data at $\sqrt{s} = 13\,\text{TeV}$. *Eur. Phys. J. C*, 76:292, 2016.

[91] Matteo Cacciari, Gavin P. Salam, and Gregory Soyez. The anti-k_t jet clustering algorithm. *JHEP*, 04:063, 2008.

[92] Matteo Cacciari, Gavin P. Salam, and Gregory Soyez. FastJet User Manual. *Eur. Phys. J. C*, 72:1896, 2012.

[93] ATLAS Collaboration. Tagging and suppression of pileup jets with the ATLAS detector. ATLAS-CONF-2014-018, 2014.

[94] Andreas Hoecker et al. TMVA - Toolkit for Multivariate Data Analysis, 2007.

[95] ATLAS Collaboration. Jet energy scale measurements and their systematic uncertainties in proton–proton collisions at $\sqrt{s} = 13\,\text{TeV}$ with the ATLAS detector. *Phys. Rev. D*, 96:072002, 2017.

[96] ATLAS Collaboration. Selection of jets produced in 13 TeV proton–proton collisions with the ATLAS detector. ATLAS-CONF-2015-029, 2015.

[97] Optimisation and performance studies of the ATLAS b-tagging algorithms for the 2017-18 LHC run. 7 2017.

[98] ATLAS Collaboration. ATLAS b-jet identification performance and efficiency measurement with $t\bar{t}$ events in pp collisions at $\sqrt{s} = 13\,\text{TeV}$. *Eur. Phys. J. C*, 79:970, 2019.

[99] ATLAS Collaboration. Measurement of b-tagging efficiency of c-jets in $t\bar{t}$ events using a likelihood approach with the ATLAS detector. ATLAS-CONF-2018-001, 2018.

[100] ATLAS Collaboration. Calibration of light-flavour b-jet mistagging rates using ATLAS proton–proton collision data at $\sqrt{s} = 13$ TeV. ATLAS-CONF-2018-006, 2018.

[101] ATLAS Collaboration. Electron and photon performance measurements with the ATLAS detector using the 2015–2017 LHC proton–proton collision data. *JINST*, 14:P12006, 2019.

[102] ATLAS Collaboration. Muon reconstruction and identification efficiency in ATLAS using the full Run 2 pp collision data set at $\sqrt{s} = 13\,\text{TeV}$. *Eur. Phys. J. C*, 81:578, 2020.

[103] Yu.L Dokshitzer, G.D Leder, S Moretti, and B.R Webber. Better jet clustering algorithms. *JHEP*, 08:001–001, 1997.

[104] F. Anulli et al. The Level-1 Trigger Muon Barrel System of the ATLAS experiment at CERN. *JINST*, 4:P04010, 2009.

[105] Chollet, François and others. Keras. https://keras.io, 2015.

[106] M. Abadi et al. TensorFlow: Large-scale machine learning on heterogeneous systems. 2016.

[107] Josh Cogan, Michael Kagan, Emanuel Strauss, and Ariel Schwarztman. Jet-Images: Computer Vision Inspired Techniques for Jet Tagging. *JHEP*, 02:118, 2015.

[108] Luke de Oliveira, Michael Kagan, Lester Mackey, Benjamin Nachman, and Ariel Schwartzman. Jet-images — deep learning edition. *JHEP*, 07:069, 2016.

[109] Quark versus Gluon Jet Tagging Using Jet Images with the ATLAS Detector. 7 2017.

[110] Formulae for Estimating Significance. 2020.

[111] Morad Aaboud et al. Performance of the ATLAS Trigger System in 2015. *Eur. Phys. J. C*, 77(5):317, 2017.

[112] Georges Aad et al. Search for neutral long-lived particles in pp collisions at $\sqrt{s} =$ 13 TeV that decay into displaced hadronic jets in the ATLAS calorimeter. *JHEP*, 06:005, 2022.

[113] ATLAS Collaboration. Measurement of the Inelastic Proton–Proton Cross-Section at $\sqrt{s} = 13$ TeV with the ATLAS Detector at the LHC. ATLAS-CONF-2015-038, 2015.

[114] Alexander L. Read. Presentation of search results: the CL_S technique. *J. Phys. G*, 28:2693, 2002.

[115] Glen Cowan, Kyle Cranmer, Eilam Gross, and Ofer Vitells. Asymptotic formulae for likelihood-based tests of new physics. *Eur. Phys. J. C*, 71:1554, 2011.

[116] Constraining the Dark Sector with the monojet signature in the ATLAS experiment. Technical report, CERN, Geneva, 2021. All figures including auxiliary figures are available at https://atlas.web.cern.ch/Atlas/GROUPS/PHYSICS/PUBNOTES/ATL-PHYS-PUB-2021-020.

[117] Georges Aad et al. Search for new phenomena in events with an energetic jet and missing transverse momentum in pp collisions at $\sqrt{s}$ =13 TeV with the ATLAS detector. *Phys. Rev. D*, 103(11):112006, 2021.

[118] LHCb Collaboration. Search for Dark Photons Produced in 13 TeV pp Collisions. *Phys. Rev. Lett.*, 120(6):061801, 2018.

[119] Philip Ilten, Yotam Soreq, Mike Williams, and Wei Xue. Serendipity in dark photon searches. *JHEP*, 06:004, 2018.

[120] Louie Dartmoor Corpe and Iacopo Longarini. Long-lived particle summary plots for Hidden Sector and Dark Photon models. Technical report, CERN, Geneva, 2022. All figures including auxiliary figures are available at https://atlas.web.cern.ch/Atlas/GROUPS/PHYSICS/PUBNOTES/ATL-PHYS-PUB-2022-007.

[121] Giovanni Calderini. The ATLAS ITk detector for High Luminosity LHC upgrade. *Nucl. Instrum. Meth. A*, 1040:167048, 2022.

[122] Jens Kröger, Simon Spannagel, and Morag Williams. User Manual for the Corryvreckan Test Beam Data Reconstruction Framework, Version 1.0. 12 2019.

[123] G. Apollinari, O. Brüning, T. Nakamoto, and Lucio Rossi. High Luminosity Large Hadron Collider HL-LHC. *CERN Yellow Rep.*, (5):1–19, 2015.

[124] Technical Design Report for the ATLAS Inner Tracker Pixel Detector. Technical report, CERN, Geneva, 2017.

[125] Technical Design Report for the ATLAS Inner Tracker Strip Detector. Technical report, CERN, Geneva, 2017.

[126] R. Diener et al. The DESY II Test Beam Facility. *Nucl. Instrum. Meth. A*, 922:265–286, 2019.

[127] Hendrik Jansen et al. Performance of the EUDET-type beam telescopes. *EPJ Tech. Instrum.*, 3(1):7, 2016.

[128] J. Baudot et al. First test results of MIMOSA-26: A fast CMOS sensor with integrated zero suppression and digitized output. 2007.

[129] M. Benoit et al. The FE-I4 Telescope for particle tracking in testbeam experiments. *JINST*, 11(07):P07003, 2016.

[130] Y. Liu et al. EUDAQ2—A flexible data acquisition software framework for common test beams. *JINST*, 14(10):P10033, 2019.

[131] Tobias Bisanz et al. EUTelescope: A modular reconstruction framework for beam telescope data. *JINST*, 15(09):P09020, 2020.

[132] Rene Brun and Fons Rademakers. Root – an object oriented data analysis framework. *Nucl. Instrum. Meth. A*, 389(1):81 – 86, 1997.